Evaluation of Compound Semiconductors for Infrared Photo-Detection Applications

by

Jing Lu

A Dissertation Presented in Partial Fulfillment
of the Requirements for the Degree
Doctor of Philosophy

Approved March 2017 by the
Graduate Supervisory Committee:

David Smith, Chair
Terry Alford
Peter Crozier
Yong-Hang Zhang
Martha McCartney

ARIZONA STATE UNIVERSITY

May 2017

ABSTRACT

In this dissertation research, conventional and aberration-corrected (AC) transmission electron microscopy (TEM) techniques were used to evaluate the structural and compositional properties of thin-film semiconductor compounds/alloys grown by molecular beam epitaxy for infrared photo-detection. Imaging, diffraction and spectroscopy techniques were applied to TEM specimens in cross-section geometry to extract information about extended structural defects, chemical homogeneity and interface abruptness. The materials investigated included $InAs_{1-x}Bi_x$ alloys grown on GaSb (001) substrates, $InAs/InAs_{1-x}Sb_x$ type-II superlattices grown on GaSb (001) substrates, and CdTe-based thin-film structures grown on InSb (001) substrates.

The InAsBi dilute-bismide epitaxial films were grown on GaSb (001) substrates at relatively low growth temperatures. The films were mostly free of extended defects, as observed in diffraction-contrast images, but the incorporation of bismuth was not homogeneous, as manifested by the lateral Bi-composition modulation and Bi-rich surface droplets. Successful Bi incorporation into the InAs matrix was confirmed using lattice expansion measurements obtained from misfit strain analysis of high-resolution TEM (HREM) images.

Analysis of averaged intensity line profiles in HREM and scanning TEM (STEM) images of the Ga-free $InAs/InAs_{1-x}Sb_x$ type-II strained superlattices indicated slight variations in layer thickness across the superlattice stack. The interface abruptness was evaluated using misfit strain analysis of AC-STEM images, electron energy-loss spectroscopy and 002 dark-field imaging. The compositional profiles of antimony across

the superlattices were fitted to a segregation model and revealed a strong antimony segregation probability.

The CdTe/$Mg_xCd_{1-x}Te$ double-heterostructures were grown with Cd overflux in a dual-chamber molecular beam epitaxy with an ultra-high vacuum transfer loadlock. Diffraction-contrast images showed that the growth temperature had a strong impact on the structural quality of the epilayers. Very abrupt CdTe/InSb interfaces were obtained for epilayers grown at the optimum temperature of 265 °C, and high-resolution imaging using AC-STEM revealed an interfacial transition region with a width of a few monolayers and smaller lattice spacing than either CdTe or InSb.

DEDICATION

This dissertation is dedicated to my parents.

ACKNOWLEDGMENTS

I owe my deepest and greatest gratitude to my academic advisor and committee chair, Regents' Prof. David J. Smith, for his tireless guidance, encouragement and support through my degree course work and this dissertation research with great patience and kindness, and for being such a father-like figure to me both academically and personally.

My sincere appreciation is extended to the rest of my committee members, Prof. Terry L. Alford, Prof. Peter Crozier, Prof. Martha R. McCartney and Prof. Yong-Hang Zhang, for their invaluable constructive input, and inspiring discussion in and out of research.

I would like to convey my heartfelt gratitude to all my collaborators: Dr. Elizabeth H. Steenbergen, Dr. Michael J. DiNezza, Dr. Shi. Liu, Dr. Preston T. Webster, Dr. Xin-Hao Zhao, Dr. Zhi-Yuan Lin, Dr. Shane R. Johnson and Prof. Yong-Hang Zhang at Arizona State University for the design and growth of the thin-film semiconductor compounds/alloys studied; Prof. Rafal E. Dunin-Borkowski and Dr. Andras Kovacs at Ernst Ruska Center for Microscopy and Spectrocopy in Julich for kind support in STEM study; Dr. Esperanza Luna at Paul Drude Institute in Berlin for collaboration on superlattice interface study, Dr. Toshihiro Aoki and Dr. Katia March in Center for Solid State Science at ASU for invaluable teaching and guidance, all three for enjoyable and fulfilling discussions and for being dear friends outside of research; Prof. Pierre Stadelmann for patiently addressing my questions regarding image/diffraction simulations using JEMS, and Mr. Karl Weiss for technical support and encouragement. I gratefully acknowledge support from MURI Grant W911NF-10-1-0524 and the use of facilities in the John M. Cowley Center for High Resolution Electron Microscopy at Arizona State University.

Sincere thanks are presented to the dearest past and present research group members: Dr. Lin Zhou, Dr. Wenfeng Zhao, Dr. Ouyang Lu, Dr. Jaejin Kim, Dr. Dinghao Tang, Dr. Zhaofeng Gan, Dr. Desai Zhang, Dr. Sahar Farjami, Dr. Xiao-Meng Shen, Saiphaneendra Bachu, Allison Boley, Abhinandan Gangopadhyay, Rajeev R. Kosireddy, Sirong Lu, Petr Mares, Thomas McConkie, Brandon McKeon, Scott Sherman, Brian Tracy, Majid Vaghayenegar and Hsin-Wei Wu, for enjoyable scientific discussions and all the cherishable laughter and tears in and out of the research lab.

I owe special thanks to my family away from home: grandma Adeline and grandpa Jim Grayson, Marcie and Kacie and Kelly Blakley, Robyn and Edward Sweeney, Brenda and Pastor Bob Dodridge, Lyndsey and Adam Henry and their lovely kids, Crystal and Ryan Gorishek and their lovely kids, Mike Gertz, Adrienne Bowers and the rest of the Oasis bible study group and worship team in CrossPoint Tempe, my dearest undergraduate friends across the ocean in China, Kun Liu and Yuexin Ma, for faithfully supporting me and helping keep my sanity in these years.

Last but not least, a never-enough thank-you to my parents Yingtang Lu and Yumin Xu and my parents-in-law Cynde and Billy Turnage, my aunts Yuzhuo Lu and Yuran Lu and their families, my brother You Lu, my sister/brother-in-law Kelly and Jason Turnage, and my beloved husband Scott A. Turnage, for unconditionally and wholeheartedly supporting and tolerating me while encouraging me to develop my potential and pursue my dream.

"Great are the works of the Lord; they are studied by all who delight in them."

Psalm 111:2 NAS

TABLE OF CONTENTS

Page

CHAPTER PAGE

LIST OF TABLES

LIST OF FIGURES

Figure Page

Figure Page

Figure Page

CHAPTER 1

INTRODUCTION AND OVERVIEW

Infrared detector technology nowadays spans across a wide variety of terrestrial and astronomical, civilian and military applications including imaging, spectroscopy and communications [1]. The prior interest in infrared materials has mostly been driven by military needs such as night vision, thermal sensing and tracking systems. The research and development of semiconductors for infrared photo-detection has been active since the early 1910s, and infrared photo-detectors have gone through several generations of evolution [2]. Currently, the predominant material in use for the infrared range of wavelengths is $Hg_{1-x}Cd_xTe$ (MCT), which is an intrinsic direct-bandgap semiconductor alloy. MCT has notable advantages such as providing controllable bandgap engineering in the range of 1 – 20 μm through slight adjustment of alloy composition, as well as high electron mobility. However, MCT has disadvantages, which include compositional non-uniformity and low mechanical strength, and mercury is a toxic material [3].

Thus, researchers continue to explore materials that could be more advantageous as photodetectors than MCT. The research in this dissertation lies along this direction, investigating alternative systems for reliable infrared photo-detection using transmission electron microscopy-based techniques, mainly from the perspective of fundamental material properties. Material shortcomings become evident in different ways in different systems, and it is important to identify any bottlenecks in terms of structural properties that could degrade infrared photo-detection, and attempt to overcome them where possible. The overall goal is to evaluate the as-grown structures for correlation with results from other techniques such as X-ray diffraction and time-resolved photoluminescence, to

progressively improve the epitaxial layer quality through elimination of extended defects, and eventually to achieve controlled engineering of specific structures with the desired optoelectronic properties.

Three material systems grown by molecular beam epitaxy on III-V substrates have been investigated. These systems were Ga-free type-II superlattices ($InAs/InAs_{1-x}Sb_x$), dilute $InAs_{1-x}Bi_x$ bismide alloys, and CdTe epitaxial layers, which could serve as intermediate buffer layers for the growth of $Hg_{1-x}Cd_xTe$, or function as absorbing layers in solar cells. Details are provided in the respective chapters of this dissertation. Challenges in exploiting these materials for detector applications mainly involve control of structural properties such as point defects, line defects and planar defects, as well as control of composition. The substrates used for growth were GaSb (001) and InSb (001), rather than the more commonly used silicon or GaAs, for a highly strategic reason, namely, to enable the possibility of the as-grown epitaxial layers being nearly or completely lattice-matched with the corresponding substrate, thus reducing the likelihood of structural relaxation through the creation of extended defects.

1.1. Infrared Radiation

Infrared waves are electromagnetic in nature and infrared radiation is invisible to human vision. The spectral span is in the range of 0.7 to 1000 μm in wavelength, beyond the long-wavelength edge of the visible spectrum. Most objects emit infrared radiation: an object in equilibrium with its surroundings actually emits radiation over a broad range of wavelengths. A blackbody is considered to be an ideal radiator and complete absorber within a cavity that is in thermal equilibrium with cavity walls at temperature T. The spectral dependence of radiation emission as a function of temperature can be described

using Planck's radiation law over the entire wavelength range from zero to infinity, with the hypothesis that energy is emitted in discrete quanta. Figure 1.1 shows the blackbody spectral emittance at several temperatures according to Planck's law [4].

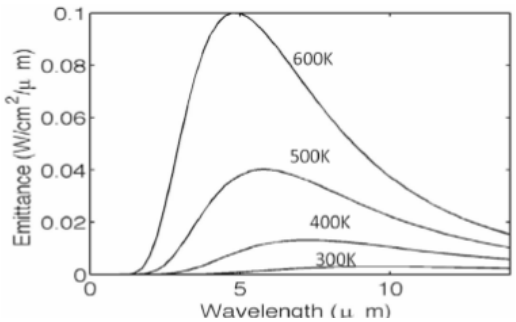

Figure 1.1 Spectral emittance of a blackbody according to Planck's law [4].

At each temperature, the emissive power starts from zero at 0 μm, increases rapidly and reaches a maximum at a certain wavelength, then decreases and approaches zero again at very long wavelength, as evident in Figure 1.1. The peak wavelength of the blackbody spectral emission depends on the temperature: the higher the temperature, the shorter the wavelength. The spectral emittance peaks in the infrared range at relatively low temperatures; for ambient temperature (~ 300 K,), the maximum emissive power lies at around 9.7 μm, as shown in Figure 1.2 [5]. Although real objects have limited emissivity due to finite transmission and reflection, and emit less radiation than an ideal blackbody of the same size at the same temperature, they can be approximated as gray-bodies over certain spectral ranges [6, 7].

Not all radiation emitted from an object is transmitted through the Earth's atmosphere (see Figure 1.3), since the atmosphere selectively absorbs radiation of certain wavelengths (mainly due to water vapor and carbon dioxide), and it also attenuates the transmitted spectrum from gray-body radiation [8]. The infrared spectrum of wavelengths

contains the following important atmospheric transmission windows: short-wavelength infrared (1 – 3 μm), mid-wavelength infrared (3 – 5 μm), long-wavelength infrared (8 – 12 μm), and very-long-wavelength infrared (12 – 30 μm) [9]. The response windows of infrared photo-detectors are usually engineered to overlap with these atmospheric transmission spectral ranges, especially for systems of tactical importance.

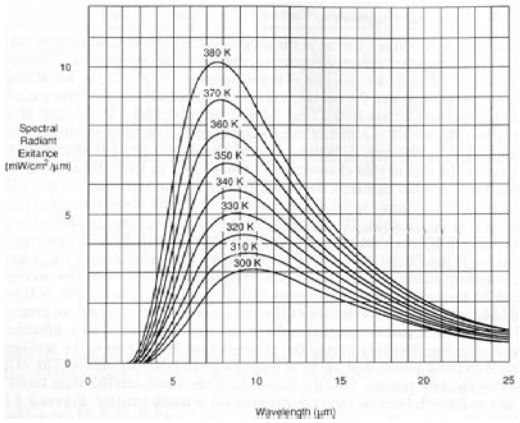

Figure 1.2 Blackbody spectral emittance for objects with temperatures in the range of 300 – 380 K [5].

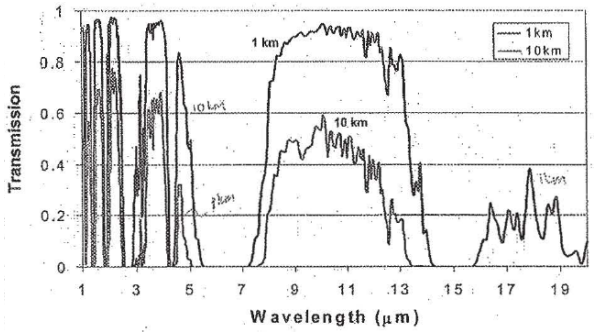

Figure 1.3 Atmospheric transmission of infrared spectrum at sea level [8].

1.2. Semiconductor Materials for IR Photon Detectors

1.2.1. Semiconductor Basics

When atoms with discrete energy levels are brought into close proximity in an ordered manner, energy bands are formed with the electrons having a continuous energy

range. The conduction band contains the highest energy levels that electrons can occupy at temperatures higher than zero Kelvin, and it is separated from the valence band, which is filled with electrons, by an energy band gap with an energy difference between the lowest energy level of the conduction band and the highest energy level of the valence band [10]. The electrical resistivity of materials is directly related to the energy band structure, in particular the relative positions of the conduction band, the valence band and the Fermi level. Based on their electrical resistivity, materials can generally be categorized as conductors, semiconductors and insulators, where semiconductors have resistivity in the range of 10^{-3} to 10^{8} ohm-cm at room temperature [11].

Charge transport in semiconductors is carried out either by electrons in the conduction band and/or by holes in the valence band, and requires available energy levels for carriers in the respective energy bands. For insulators, the band gap is so wide that thermal excitation fails to provide adequate energy to excite electrons into the conduction band and create available states in either band, and no current flow occurs. For semiconductors, thermal energy can be sufficient to excite some electrons into the conduction band, creating partially filled conduction and partially depleted valence bands, which allows the transport of charge and the creation of current flow. Temperature plays an important role in determining electron distribution. At zero Kelvin and in the absence of defects or impurities, semiconductors behave as insulators due to the absence of available energy states in the conduction and valence bands. Generally, semiconductors have band gaps between ~ 0.1 eV and ~ 4 eV at room temperature [10]. The concept of a band gap no longer exists for metals because there are ample charge carriers due to very

small gap or overlapping of the conduction and valence bands, and resistivity is many orders of magnitude smaller [12].

Direct band-gap and indirect band-gap: A material has a direct band-gap when the conduction band minima and valence band maxima align at the same wavevector value, whereas the band gap is indirect when the conduction and valence extrema points are misaligned with a substantial wavevector. The electronic interband transitions in this latter case must involve phonons in order to satisfy conservation of momentum [13].

Intrinsic and extrinsic: an intrinsic semiconductor contains insignificant amounts of impurity atoms so that its electronic properties are native to the material itself, and the electron carrier concentration equals the hole carrier concentration because excitation of a valence electron into the conduction band leads to simultaneous creation of a hole in the valence band. An extrinsic semiconductor is produced when specific impurity atoms are added, preferably in a controlled fashion, and the electronic properties are determined mostly by the ionized dopants. Depending on the type of dopant atom, there are *n*-type semiconductors (doped with shallow-level donors) that have enhanced electron carrier population, and the majority carriers are electrons; and *p*-type semiconductors (shallow-level acceptors) that have enhanced hole carrier population, and the minority carriers are electrons [14].

Carrier lifetime: Charge carriers, i.e. electrons and holes, are constantly being generated and annihilated in semiconductors, even under equilibrium conditions. Carrier generation and recombination can occur via several processes, and the rates at which these processes occur affect the carrier population. Under equilibrium conditions, generation and recombination occur at the same rate and balance each other, hence leaving the carrier

concentrations unchanged. There are three major recombination mechanisms (Figure 1.4): (1) radiative recombination, where electrons and holes directly annihilate and photons are produced to release the excess energy; (2) Shockley-Reed-Hall recombination, where electron and hole annihilation is facilitated by a deep-level impurity or trap (associated with defects), and phonons are created to dissipate the liberated energy; (3) Auger recombination, where electron-hole recombination and collision of two like carriers occur simultaneously, and the recombination energy is absorbed by the surviving carrier [15].

The reverse of each of these recombination processes is a corresponding generation process: optical generation, thermal generation and impact ionization generation. When a mild perturbation (low-level injection) is applied to an extrinsic semiconductor, excess electrons and holes are generated at the same rate (ignoring trapping). These excess carriers barely bring any change to the majority carrier population, but may temporarily enhance the minority carrier concentration by several orders of magnitude. The minority carrier lifetime is the average lifetime that an excess minority carrier experiences in a population of majority carriers, and is an important parameter for device modeling [15].

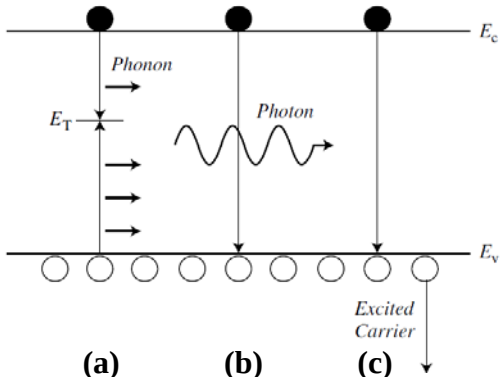

Figure 1.4 Recombination mechanisms: (a) Shockley-Reed-Hall recombination; (b) radiative recombination, and (c) Auger recombination [15].

There are limited number of elements and possible combinations of elements that form semiconductors (Table 1.1). The family of semiconductor materials include: elemental semiconductors consisting of elements from group IV of the Periodic Table (e.g. Si and Ge), and semiconductor compounds and alloys including binary (e.g. GaAs), ternary (e.g. $GaAs_{1-x}P_x$) and quaternary (e.g. $Ga_xIn_{1-x}As_{1-y}P_y$) alloys, generally formed by combining elements from group IV, or from groups that are equally distant from group IV (e.g. groups III-V and groups II-VI compounds), with the exception of some IV-VI compounds [16]. The elements that form the semiconductor compounds studied in this dissertation are highlighted in Table 1.1, with groups III & V colored in yellow, and groups II & VI colored in blue.

Table 1.1 Partial Periodic Table showing elements that can form semiconductors.

II	III	IV	V	VI
^{4} **Be**	^{5} **B**	^{6} **C**	^{7} **N**	^{8} **O**
^{12} **Mg**	^{13} **Al**	^{14} **Si**	^{15} **P**	^{16} **S**
^{30} **Zn**	^{31} **Ga**	^{32} **Ge**	^{33} **As**	^{34} **Se**
^{48} **Cd**	^{49} **In**	^{50} **Sn**	^{51} **Sb**	^{52} **Te**
^{80} **Hg**	^{81} **Tl**	^{82} **Pb**	^{83} **Bi**	^{84} **Po**

Elemental semiconductors such as Si and Ge have the diamond-cubic lattice structure (space group Fd3m), which consists of two identical face-centered-cubic sublattices displaced along the body diagonal direction by a quarter of the body diagonal [Figure 1.5 (a)]. Group III-V and group II-VI compound semiconductors can either arrange in the zincblende structure (space group $F\bar{4}3m$), which resembles the diamond-cubic

structure but with two distinguishable sublattices interpenetrating each other (e.g., GaAs in Figure 1.5 (b), with the group-III sublattice and group-V sublattice), or the wurtzite structure (space group $P6_3mc$) (e.g., GaN in Figure 1.5 (c)). Both zincblende and wurtzite structures are tetrahedrally coordinated. Group IV-VI compounds, such as PbS and PbSe, can also crystallize in the rock-salt structure (space group $Fm\underline{3}m$) (PbS structure shown in Figure 1.5 (d)) [18].

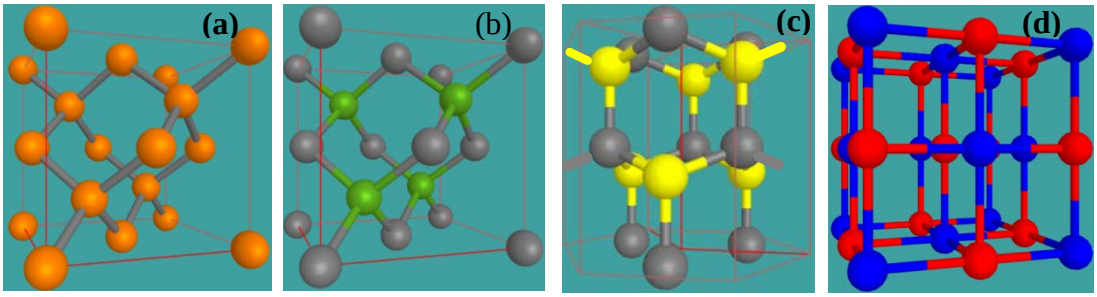

Figure 1.5 Schematic illustration of crystalline semiconductor structures simulated using JEMS [17]: (a) Si; (b) GaAs: Ga in grey, As in green; (c) GaN: Ga in grey, N in yellow; (d) PbS: Pb in blue, S in red.

1.2.2. Semiconductor Growth using Molecular Beam Epitaxy

The technique of molecular beam epitaxy (MBE) was initially developed in the late 1960s, and has since become a powerful and versatile tool for the epitaxial growth of thin-film semiconductors [19-21]. MBE is essentially an ultrahigh-vacuum-based evaporation technique that achieves controlled mass transfer from sources to the substrate. Fluxes of the constituent atomic/molecular species that are generated at the source travel under ultrahigh vacuum in rectilinear paths towards the heated substrate, where they condense and react with each other to form epitaxial films in a kinetic-growth fashion [22].

The evaporated atoms contained in the fluxes, or beams, have long mean free paths so that they usually experience no interaction with each other or with the residual gas in

the vacuum chamber. Fluxes in solid-source MBE are usually generated through thermal evaporation using Knudsen-type effusion cells, tunable by precise control of the cell temperatures and computer-controlled mechanical shutters, and can be monitored through measurement of the corresponding beam equivalent pressures. The substrate is continuously rotated to enhance the film uniformity in terms of composition and thickness. The growth can be monitored and controlled *in situ* using reflection high-energy electron diffraction (RHEED), which allows studies of the surface crystallography and the growth kinetics/dynamics [23]. The kinetic growth process can be considered as involving: (a) adsorption of the incident atoms or molecules; (b) migration and dissociation on the surface; and (c) incorporation of atoms at the growth front via surface reaction [24]. With ultrahigh-vacuum, low deposition rate of around one monolayer per second, a kinetic growth mechanism and low deposition temperature, MBE is capable of producing epitaxial films in a reproducible manner with well-controlled composition and thickness, and atomically sharp interfaces [21].

1.2.3. Materials for Infrared Photo-Detection

There are two major types of IR detectors: (1) photon (or quantum) detectors, which convert incoming photons into free carriers that are subsequently detected using an electrical circuit; and (2) thermal detectors, which convert the energy of the absorbed photons into increases in temperature that are subsequently monitored using temperature-sensitive parameters such as resistivity. Photon detectors usually need cryogenic cooling to prevent the generation of charge carriers by undesirable thermal excitation and to reduce thermal noise. The semiconductor materials studied in this dissertation research are primarily intended for applications as IR photon detectors, which can operate in either

photovoltaic and/or photoconductive modes, depending on whether the dominant carriers are minority or majority carriers [25].

From an engineering point-of-view, the simplest materials to exploit for IR detection purposes are either intrinsic binary semiconductor compounds with narrow bandgaps or extrinsic elemental semiconductors. Photoconductive IR detectors based on polycrystalline PbS [26], PbSe and PbTe [27] were among the first to be developed and used for photo-detection in the SWIR and MWIR ranges. Following invention of the transistor and maturing of material purification and controlled doping processes, extrinsic germanium (Ge doped with Hg [28]] and later extrinsic silicon with various dopants [29], provided photo-detection capability in the LWIR range. However, a major disadvantage of utilizing extrinsic excitation is the requirement for cooling below ~ 40 K in order to freeze out impurities and to enhance the performance and sensitivity. Narrow band-gap binary semiconductors such as InSb were also explored in the early stages [30]. However, the cut-off wavelengths of these elemental or binary compound semiconductors were inadequate to cover the LWIR range, prompting the need to consider ternary alloys in order to expand the wavelength capability.

1.2.4. HgCdTe Semiconductor Alloys

Narrow bandgap semiconductor alloys can provide tunable bandgaps over a wide spectral range through control of the alloy composition. The preparation and initial study of electrical and optical properties of mixed crystals of HgTe-CdTe [31], including photoconductive and photovoltaic response, demonstrated the potential that this single-phase alloy possessed as an intrinsic IR detection material, in particular spanning a wavelength range from 0.8 μm (pure CdTe) to 13 μm (alloy containing 90% HgTe) simply

by tuning Cd concentration. The band-gap variability and potentially higher operating temperature compared with extrinsic materials triggered intensive research and the development of HgCdTe for IR photo-detection devices [31]. This pseudo-binary alloy has since been the material of choice for first-generation scanning detectors, second-generation staring IR focal-plane arrays (FPAs), and is easily adaptable to the third-generation multicolor IR FPAs in MWIR and LWIR [32, 33]. HgTe and CdTe both have the zincblende structure, with a small lattice mismatch of ~ 0.3 %, and they form a solid solution over the entire composition range from pure CdTe (bandgap 1.5 eV) to pure HgTe (bandgap – 0.3 eV, semimetal), with the alloy bandgap being continuously variable across the SWIR to VLWIR ranges from ~ 1 – 30 um,. Moreover, MCT has large photo-absorption coefficient, high electron mobility, low dielectric constant, and inherent recombination mechanism, which mean high quantum efficiency, fast response and higher operating temperature.

HgCdTe has several disadvantages: the weak Hg-Te bonding can cause instabilities at surfaces and interfaces, and in bulk MCT (which can result in low yield), while compositional homogeneity remains problematic especially for the LWIR range [2]. The challenges associated with bulk crystal growth methods, i.e., control of stoichiometry and composition at high Hg pressure, segregation due to the wide separation of solidus and liquidus, and control of point defects, can be improved by using epitaxial techniques that enable growth of complex MCT heterostructures with compositional uniformity and controlled doping profiles. Vapor phase epitaxy (VPE) methods, such as metalorganic chemical vapor deposition (MOCVD) and molecular beam epitaxy (MBE), offer non-equilibrium growth modes, and help to realize the growth of complex structures with the

required doping by adjusting the growth conditions dynamically. MBE is the dominant VPE method for growth of sophisticated MCT structures, since it provides low-temperature growth under ultrahigh vacuum, *in situ* doping, and good control of composition, doping and interfacial profiles [34, 35]. However, epitaxial growth requires suitable substrates. Various substrates for epitaxial MCT growth have been evaluated but the ideal substrate has not yet been identified [36]. These disadvantages of MCT have motivated the search for alternative IR materials, which are described in the following section.

1.3. Alternative Semiconductors for Infrared Photon Detectors

A myriad of semiconductor materials have been evaluated as potential alternatives to MCT for third-generation IR detectors, especially for the spectral ranges of MWIR and LWIR (and VLWIR). Several materials, especially those based on group III-V compounds, such as quantum-well infrared photodetectors and type-II strained-layer superlattices, demonstrate great promise. The group III-V semiconductors are in general mechanically stronger than the II-VI semiconductors, and they provide a range of lattice constants and band structures/gaps, and they have relatively mature growth and processing techniques.

1.3.1. Type-II Superlattices

Beyond the traditional methods of band-gap engineering such as alloying and doping for tailoring electronic and optical properties of semiconductors, the band structure of synthetic layered semiconductor heterostructure can be controlled in a nearly continuous way by spatially varying the composition and doping profiles [37, 38]. The use of MBE for this purpose has opened up the possibility of achieving photo-detection over the entire IR spectrum through precise control of the composition, doping and thickness of the constituent layers with ideally atomically abrupt interfaces.

Different III-V heterostructures have been proposed and evaluated for photo-detection in MWIR and LWIR, taking advantage of their superior chemical bonding strength over II-VI materials, and the relatively mature growth and processing technologies. Quantum-well infrared photo-detectors (QWIP) are heterostructures with type-I band alignment [39]. They consist of a series of thin layers of narrow-bandgap semiconductors, each sandwiched between two thick layers of a wide-bandgap semiconductor. Quantized energy levels within the quantum wells are controlled by the thickness and depth of the wells. Infrared absorption is achieved through intersubband excitation, and requires doping. One prominent example is the GaAs/AlGaAs multiple quantum well system, which has been very well studied and developed [40].

When the barriers of the wells are sufficiently thin, tunneling between wells becomes significant, and an effective superlattice structure is formed [41]. The discrete energy levels within isolated wells change into energy minibands across the whole superlattice stack. These can be engineered through judicious choice of materials, composition and thickness of the constituent layers, and the effective band gap can be smaller than for either of the constituents. In addition, growth of high-quality lattice-mismatched superlattice heterostructures can be achieved provided that the layers are thin enough, so that lattice mismatch is accommodated by coherency strain of the layers [42]. Such internal strain can serve as an additional band-gap engineering tool by modifying the band gap of the constituent materials through splitting of the degeneracy of the valence-band maxima [43, 44]. These heterostructures are termed strained-layer superlattices. Strained-layer superlattices with type-II band alignment provide the capability for IR photo-detection over the whole IR spectrum via interband transitions, with the effective

band gap being engineered through choice of material, layer thickness, composition and misfit strain. This approach provides strategic advantages, such as suppressed Auger recombination, since electrons and holes are spatially separated in adjacent layers.

InAs/$Ga_{1-x}In_xSb$ strained-layer superlattices were proposed and widely studied as a potential candidate for LWIR detection [45]. However, these structures suffered from short minority carrier lifetimes, most likely due to Shockley-Reed-Hall recombination induced by Ga-related native defects [46]. Ga-free InAs/$InAs_{1-x}Sb_x$ type-II strained-layer superlattices (T2SLs), one of the material systems investigated here, have demonstrated significantly improved minority carrier lifetimes, which are up to and exceeding an order of magnitude longer than those measured for Ga-containing T2SLs, depending on the wavelength [47, 48]. Ga-free InAs/$InAs_{1-x}Sb_x$ T2SLs grown using carefully designed superlattices for strain balance and proper control over growth conditions, have very low densities of extended defects [49, 50]. Hence, carrier recombination due to extended defects should no longer be the performance-limiting factor for these materials.

Evidence suggests that the bottleneck that could be hindering the performance at the current stage of development of InAs/InAsSb T2SLs lies in control of the compositional profile, i.e., the Sb compositional distribution. This effectively determines the superlattice layer thickness and composition, which in turn control the band-gap engineering [51]. Analysis of asymmetric superlattice peaks visible in high-resolution X-ray diffraction (HRXRD) rocking curve patterns through simulations suggests the possibility of non-uniform $InAs_{1-x}Sb_x$ layer thickness and/or Sb composition throughout the superlattice stack [52]. Interface chemical diffuseness deduced from scanning tunneling microscopy and transmission electron microscopy may also be present [51, 53-55]. Either type of

compositional disorder could introduce perturbations to the superlattice band structure, causing deviations from the design parameters and deterioration of the optoelectronic response. These possibilities have been researched in this dissertation.

1.3.2. $InAs_{1-x}Bi_x$ Dilute Bismide Alloys

Dilute bismides based on III-V host semiconductors are emerging alloys that possess interesting band-structure engineering capability due to the large band-gap bowing analogous to the dilute nitrides; a small amount of substitutional bismuth present in the group-V sublattice creates impurity energy levels within the host valence band, and interaction between the valence band states and the Bi states significantly reduces the band gap and creates strong spin-orbit splitting [56-58]. Thus, trace incorporation of Bi into narrow-band-gap III-V compound semiconductors can extend their access to the IR spectrum across MWIR and LWIR regions. Recent research has been directed towards the development of a range of narrow-band-gap bismides using MBE, e.g. $InSb_{1-x}Bi_x$ [59, 60], $GaSb_{1-x}Bi_x$ [61] and $InAs_{1-x}Bi_x$ [62].

The synthesis of III-V-Bi alloys is problematic because of the large miscibility gap and the small equilibrium solid solubility of Bi. Even non-equilibrium growth methods such as MBE have problems due to the large difference between the size, mass and bonding energy of Bi and the host group-V element. Bi is the largest and heaviest group-V element, with weak III-Bi bonding strength. It has a strong tendency to segregate and form surface droplets or bulk clusters, and to occupy interstitial sites. Hence, uniform substitutional incorporation of modest Bi concentrations in III-V alloys has proven to be very challenging [63]. For example, lattice contraction in $GaSb_{1-x}Bi_x$ was revealed by X-ray diffraction rocking curve measurement [60], which contradicts the prediction of a ternary material

based on substitutional incorporation of Bi, since GaBi (lattice constant of 0.6324 nm) has a larger lattice parameter than GaSb (lattice constant of 0.6096 nm). This lattice contraction was attributed to possible vacancies induced by Bi segregation. Atomic ordering and phase segregation were reported for $GaAs_{1-x}Bi_x$ grown using low-temperature MBE [64].

$InAs_{1-x}Bi_x$ grown by MBE has been relatively less investigated, but it is attracting increasing attention. Growth of $InAs_{1-x}Bi_x$ by way of metalorganic vapor phase epitaxy (MOVPE) was investigated for application in uncooled LWIR photo-detection [65, 66]. Growth by way of MBE has just recently been explored [62, 67]. In order to push forward the understanding and control of Bi incorporation, and the potential development of $InAs_{1-x}Bi_x$ as an IR photo-detection material, there is a strong need for fundamental research on the as-grown InAsBi, and to study the potential similarity/difference with the other III-V-Bi compounds. It is also of interest to carry out comparisons that contrast the microstructure of $InAs_{1-x}Bi_x$ and $GaAs_{1-x}Bi_x$ (or other III-V-Bi), to facilitate a better understanding of Bi incorporation. These factors have been explored in this dissertation research.

1.3.3. CdTe Grown on InSb

MBE is the dominant VPE method for growth of sophisticated MCT structures. It provides low-temperature growth under ultrahigh vacuum with *in situ* doping capability, and enables good control of composition and doping and interfacial profiles. However, there is a lack of an economic and large-area substrate that is structurally and mechanically matched with MCT for epitaxial growth [68]. CdTe substrates have significant lattice mismatch with MWIR and LWIR HgCdTe. Moreover, in common with CdZnTe substrates (closely lattice-matched to MCT), they are typically grown by the Bridgman technique, and suffer from limited substrate size, impurity, non-uniformity, high dislocation density

and high cost [69]. Silicon is an exemplary substrate material for hybrid applications, and it is attractive for its low cost, large-area availability and easy integration with Si readout circuits in focal-plane arrays (FPA). However, the dislocation density for MCT growth (few $\times 10^6$ cm^{-2}) is less than satisfactory for LWIR applications, even after introducing CdTe buffer layers and taking advantage of misorientation with the substrate [70].

The interest in epitaxial thin films of CdTe grown by MBE began in the early 1980s [71] because of potential applications in optoelectronics devices (e.g. infrared photo-detectors), as well as for hybrid substrates, serving as intermediary buffers on economic substrates, for the epitaxial growth of HgCdTe alloys and HgTe-CdTe superlattices [72]. The use of InSb as a candidate substrate for CdTe growth appears ideal because the two materials are nearly lattice-matched ($|\Delta a| / a \leq 5 \times 10^{-4}$ at room temperature), and they have very similar thermal expansion coefficients. However, defective interfacial III-VI structures are reported even with the use of Cd/Te flux ratios of greater than unity during MBE growth [73]. Interfacial compounds with different lattice parameters would be liable to induce strain at the interface and possibly contribute to the formation of extended defects. Through proper handling of MBE growth parameters, such as substrate surface preparation, growth temperature [74], and, most importantly, introduction of an intermediate InSb buffer layer in a dual-chamber molecular beam epitaxy (MBE) system [75], epitaxial CdTe films with high structural quality have recently been obtained [76]. In addition, the recent exploration of monocrystalline CdTe thin films for solar cells, providing competition with polycrystalline CdTe solar cells, has spurred increased interest. The Shockley-Reed-Hall recombination lifetime achieved was more than one order of magnitude longer than that of polycrystalline CdTe [76].

A serious complication persisting for the epitaxial growth of CdTe thin films with reasonable structural quality on InSb lies in the fact that CdTe (group II-VI compound) and InSb (group III-V compound) represent a heterovalent pair of compound semiconductors. The possible formation of an interfacial III-VI alloy due to inter-diffusion has been investigated by soft X-ray photoelectron spectroscopy (XPS) [77] and Raman spectroscopy [78]. However, there have so far been no published electron microscopy observations of any such interfacial compounds.

The characterization by X-ray diffraction (XRD) of epitaxial CdTe films grown on InSb substrates at different substrate temperatures has indicated that the full-width at half-maximum of the CdTe XRD peak may not be a strong indication of the structural quality [79]. Thus, alternative techniques such as photoluminescence and cross-sectional transmission electron microscopy (XTEM) need to be incorporated to provide more comprehensive and reliable characterization of the CdTe epilayers.

1.4. Overview of Dissertation Research

In this dissertation, conventional and aberration-corrected transmission electron microscopy techniques including imaging, diffraction and spectroscopy have been utilized to evaluate the structural and compositional properties of epitaxial semiconductor films grown by MBE on different substrates. The materials targeted for investigation are dilute $InAs_{1-x}Bi_x$ alloys grown on GaSb substrates, Ga-free $InAs/InAs_{1-x}Sb_x$ type-II superlattices grown on GaSb substrates with or without Bi as surfactant, and CdTe-based structures grown on InSb substrates.

Fundamental properties of these compound semiconductors are summarized in Table 1.2, including the crystal structure, lattice constant and band gap [80, 81].

In Chapter 2, the preparation of MBE-grown thin-film structures for transmission electron microscopy (TEM) observation, the experimental setups designed for imaging, diffraction and spectroscopy in TEM or scanning transmission electron microscopy (STEM) mode, and methods used for data analysis are described.

Table 1.2 Fundamental properties of studied compound semiconductors [80, 81].

Compound	**Crystal Structure**	**Lattice Constant/nm (at 300 K)**	**Band Gap/eV (close to 0 K)**
GaSb	Zincblende	0.6096	0.812
InAs		0.6058	0.418
InSb		0.6479	0.235
AlSb		0.6136	2.384
CdTe		0.6481	1.606
MgTe		0.6420	3.356
InBi		0.686	-1.63

The structure of $InAs_{1-x}Bi_x$ dilute bismide epitaxial films grown on GaSb (001) substrates at low growth temperature are described in Chapter 3. Cross-sectional TEM images revealed that extended defects were occasionally observed, and bismuth incorporation was confirmed through misfit strain analysis of high-resolution images [54]. A lack of chemical homogeneity in all of the films, which was associated with the difficulty of incorporating the relatively large and heavy Bi atoms, was observed in diffraction contrast images. Lateral modulation of bismuth composition and surface droplets rich in Bi were also observed.

Chapter 4 describes Ga-free $InAs/InAs_{1-x}Sb_x$ type-II strained superlattices grown on GaSb substrates which were found to be largely free of extended defects. The observations thus focused more on investigating the uniformity of the superlattice stack and the interface abruptness. The possible variation of superlattice layer thickness

throughout the entire stack was evaluated by analyzing the intensity line profiles of high-resolution TEM lattice-fringe images. Interface abruptness was studied using misfit strain analysis of high-resolution images, diffraction techniques, electron energy-loss spectroscopy and dark-field imaging. The Sb compositional profiles across the superlattices were fitted to a phenomenological segregation model to reveal the Sb segregation probability [82].

In Chapter 5, CdTe-based structures, primarily, CdTe/$Mg_xCd_{1-x}Te$ double-heterostructures, grown on InSb (001) substrates were investigated to provide details about the structural properties and the nature of the heterovalent CdTe/InSb interface. Diffraction-contrast images showed that the growth temperature had a strong impact on the structural properties of the epitaxial films grown with Cd overflux: films grown at the optimal temperature of 265 °C were largely free of extended defects, whereas films grown at higher or lower temperature had complicated networks of extended defects. The CdTe/InSb interfaces were grown with pre-growth Cd flux treatment, and were extremely abrupt. High-resolution imaging using aberration-corrected scanning transmission electron microscopy revealed that the interfacial transition region was only a few monolayers wide, with a lattice spacing smaller than either InSb or CdTe [83].

References

[1] J. L. Miller, Principles of Infrared Technology (Van Nostrand Reinhold, New York, 1994) p. 6.

[2] A. Rogalski, Opto-Electron. Rev. **20**, 279 (2012).

[3] P. Martyniuk, J. Antoszewski, M. Martyniuk, L. Faraone and A. Rogalski, Appl. Phys. Rev. **1**, 041102 (2014).

[4] R. G. Driggers, M. H. Friedman and J. Nichols, Introduction to Infrared and Electro-optical Systems, 2nd edition (Artech House, Norwood, MA, 2012) p. 127.

[5] G. J. Zissis, Sources of Radiation (Infrared Information Analysis Center, Ann Arbor, Michigan and SPIE Optical Engineering Press, Bellingham, Washington, 1993) p. 14.

[6] I. Simon, Infrared Physics (D. Van Nostrand Company, Inc. Princeton, New Jersey, 1966) p. 10.

[7] C. Kittle, Thermal Physics (John Wiley & Sons, Inc. New York, 1969) p. 253.

[8] A. Hoffman, Introduction to Infrared Detection, 39th Annual Modern infrared Detectors and System Applications, UCSB Extension, June 19-23, 2006.

[9] F. G. Smith, Atmospheric Propagation of Radiation (Infrared Information Analysis Center, Ann Arbor, Michigan and SPIE Optical Engineering Press, Bellingham, Washington, 1993) p. 46.

[10] R. F. Pierret, Advanced Semiconductor Fundamentals (Addison-Wesley Publishing Company, Inc., Massachusetts, USA, 1987) p. 53.

[11] K. K. Ng, Complete Guide to Semiconductor Devices, 2nd edition (John Wiley & Sons, Inc. New York, USA, 2002) p. 1.

[12] R. F. Pierret, Semiconductor Fundamentals (Addison-Wesley Publishing Company, Inc. Massachusetts, USA, 1988) p. 27.

[13] C. Kittel, Introduction to Solid State Physics, 8th edition (John Wiley & Sons, Inc. New York, USA, 2005) p. 188.

[14] C. Kittel, ibid., p. 209.

[15] D. Schroder, Semiconductor Material and Device Characterization, 3rd edition (John Wiley & Sons, Inc. New Jersey, USA, 2006) p. 389.

[16] R. F. Pierret, ibid. 10, p. 3.

[17] P. Stadelmann, Ultramicroscopy **21**, 131 (1987).

[18] D. B. Holt and B. G. Yacobi, Extended Defects in Semiconductors (Cambridge University Press, Cambridge, UK, 2007) p. 24.

[19] J. R. Arthur, J. Appl. Phys. **39**, 4032 (1968).

[20] A. Y. Cho, J. Appl. Phys. **41**, 2780 (1970).

[21] R. F. C. Farrow, Molecular Beam Epitaxy, Applications to Key Materials (Noyes Publications, New Jersey, USA, 1995) p. 2.

[22] V. Swaminathan and A. T. Macrander, Materials Aspects of GaAs and InP Based Structures (Prentice-Hall, Inc. New Jersey, USA, 1991) p. 138.

[23] R. F. C. Farrow, ibid. 21, p. 9.

[24] V. Swaminathan and A. T. Macrander, ibid. 22, p. 142.

[25] M. A. Kinch, Fundamentals of Infrared Detector Materials (SPIE, Bellingham, Washington, 2007) p. 5.

[26] P. W. Kruse, L. D. McGlauchlin and R. B. McQuistan, Elements of Infrared Technology (Wiley, New York, 1962) p. 399.

[27] D. J. Lovell, Amer. J. Phys. **37**, 467 (1969).

[28] S. Borrello and H. Levinstein, J. Appl. Phys. **33**, 2947 (1962).

[29] R. A. Soref, J. Appl. Phys. **38**, 5201 (1967).

[30] F. D. Morten and R. E. King, Appl. Optics **4**, 659 (1965).

[31] W. D. Lawson, S. Nielson, E.H. Putley and A.S. Young, J. Phys. Chem. Solids **9**, 325 (1959).

[32] M. A. Kinch, ibid. 25, p. 2.

[33] S. Kasap, P. Capper, Handbook of Electronic and Photonic Materials (Springer Science + Business Media, Inc. New York, USA, 2006) p. 855.

[34] A. Rogalski, Rep. Prog. Phys. **68**, 2267 (2005).

[35] J. Chu and A. Sher, Physics and Properties of Narrow Gap Semiconductors (Springer Science + Business Media, LLC, New York, 2007) p. 5.

[36] R. N. Jacobs, C. Nozaki, L. A. Almeida, M. Jaime-Vasquez, C. Lennon, J. K. Markunas, D. Benson, P. Smith, W. F. Zhao, D. J. Smith, C. Billman, J. Arias and J. Pellegrino, J. Electron. Mater., **41**, 2707 (2012).

[37] F. Capasso, Science **235**, 172 (1987).

[38] R. Dingle, W. Wiemann and C. H. Henry, Phys. Rev. Lett. **33**, 827 (1974).

[39] B. F. Levine, J. Appl. Phys. **74**, R1 (1993).

[40] B. F. Levine, K. K. Choi, C. G. Bethea, J. Walker and R. J. Malik, Appl. Phys. Lett. **50**, 1092 (1987).

[41] L. Esaki, R. Tsu, IBM J. Res. Dev. **14**, 61 (1970).

[42] J. W. Matthews and A. E. Blakeslee, J. Cryst. Growth **27**, 118 (1974).

[43] G. C. Osbourn, J. Vac. Sci. Technol. B **2**, 176 (1984).

[44] E. P. O'Reilly, Semicond. Sci. Technol. **4**, 121 (1989).

[45] C. Mailhiot, D. L. Smith, J. Vac. Sci. Technol. B **5**, 1268 (1987).

[46] S. P. Svensson, D. Donetsky, D. Wang, H. Hier, F. J. Crowne and G. Belenky, J. Cryst. Growth **334**, 103 (2011).

[47] E. H. Steenbergen, B. C. Connelly, G. D. Metcalfe, H. Shen, M. Wraback, D. Lubyshev, Y. Qiu, J. M. Fastenau, A. W. K. Liu, S. Elhamri, O. O. Cellek and Y.-H. Zhang, Appl. Phys. Lett. **99**, 251110 (2011).

[48] B. B. V. Olson, Appl. Phys. Lett. **101**, 092109 (2012).

[49] L. Ouyang, E. H. Steenbergen, Y.-H. Zhang, K. Nunna, D. L. Huffaker and D. J. Smith, J. Vac. Sci. Technol. B **30**, 02B106 (2012).

[50] X.-M. Shen, H. Li, S. Liu, D. J. Smith and Y.-H. Zhang, J. Cryst. Growth **381**, 1 (2013).

[51] A. Y. Lew, E. T. Yu and Y.-H. Zhang, J. Vac. Sci. Technol. B **14**, 2940 (1996).

[52] E. H. Steenbergen, Y.-H. Zhang, unpublished result.

[53] K. Mahalingam, E. H. Steenbergen, G. J. Brown and Y.-H. Zhang, Appl. Phys. Lett. **103**, 061908 (2013).

[54] J. Lu, P. T. Webster, S. Liu, Y.-H. Zhang, S.R. Johnson and D. J. Smith, J. Cryst. Growth **425**, 250 (2015).

[55] M. R. Wood, K. Kanedy, F. Lopez, M. Weimer, J. F. Klem, S. D. Hawkins, E. A. Shaner and J. K. Kim, J. Cryst. Growth **425**, 110 (2015).

[56] S. A. Barnett, J. Vac. Sci. Technol. A **5**, 2845 (1987).

[57] S. Francoeur, M.-J. Seong, A. Mascarenhas, S. Tixier, M. Adamcyk and T. Tiedje, Appl. Phys. Lett. **82**, 3874 (2003).

[58] K. Alberi, J. Wu, W. Walukiewicz, K. Yu, O. Dubon, S. Watkins, C. Wang, X. Liu, Y.-J. Cho and J. Furdyna, Phys. Rev. B **75**, 045203 (2007).

[59] J. J. Lee, M. Razeghi, Investigation of novel InTlSb and InSbBi alloys for uncooled photodetector applications (SPIE-INT Soc. Optical Engineering, Bellinghan, USA, 1998) p. 256.

[60] S. Wang, Y. Song and I. S. Roy, 13th International Conference on Transparent Optical Networks (ICTON), Stockholm, Sweden, June 23-30, 2011, edited by M. Jaworski and M. Marciniak (IEEE, Inc. New York, USA, 2011) p. 1.

[61] Y. Song, S. Wang, I. S. Roy, P. Shi and A. Hallen, J. Vac. Sci. Technol. B **30**, 02B114 (2012).

[62] S. P. Svensson, H. Hier, W. L. Sarney, D. Donetsky, D. Wang and G. Belenky, J. Vac. Sci. Technol. A **30**, 02B109 (2012).

[63] H. Li and Z. M. Wang, Bismuth-containing compound (Springer Science + Business Media, New York, USA, 2013) p. 5.

[64] A. G. Norman, R. France, and A. J. Ptak, J. Vac. Sci. Technol. B **29**, 03C121 (2011).

[65] K. Y. Ma, Z.M. Fang, R. M. Cohen and G. B. Stringfellow, J. Electron. Mater. **21**, 143 (1992).

[66] H. Okamoto and K. Oe, Jpn. J. Appl. Phys. **37**, 1608 (1998).

[67] P. T. Webster, N. A. Riordan, C. Gogineni, S. Liu, J. Lu, X.-H. Zhao, D. J. Smith, Y.-H. Zhang and S. R. Johnson, J. Vac. Sci. Technol. B **32**, 02C120-1 (2014).

[68] R. Triboulet, A. Tromson-Carli, D. Lorans and T. N. Duy, J. Electron. Mater. **22**, 827 (1993).

[69] A. Rogalski, Infrared Detectors (Overseas Publishers Association, Amsterdam, The Netherlands, 2000) p. 402.

[70] T. J. DeLyon, J. E. Jensen, M. D. Gorwitz, C. A. Cockrum, S. M. Johnson and G. M. Venzor, J. Electron. Mater. **28**, 705 (1999).

[71] R. F. C. Farrow, G. R. Jones, G. M. Williams and I. M. Young, Appl. Phys. Lett. **39**, 954 (1981).

[72] R. F. C. Farrow, J. Vac. Sci. Technol. A **3**, 60 (1985).

[73] G. M. Williams, C. R. Whitehouse, A. G. Cullis, N. G. Chew and G. W. Blackmore, Appl. Phys. Lett. **53**, 1847 (1988).

[74] N. G. Chew, G. M. Williams and A. G. Cullis, Inst. Phys. Conf. **68**, 437 (1983).

[75] R. F. C. Farrow, A. J. Noreika, F. A. Shirland, W. J. Takei, S. Wood, J. Jr. Greggi and M. H. Francombe, J. Vac. Sci. Technol. A **2**, 527 (1984).

[76] M. J. DiNezza, X.-H. Zhao, S. Liu, A. P. Kirk and Y.-H. Zhang, Appl. Phys. Lett. **103**, 193901 (2013).

[77] K. J. Mackey, P. M. G. Allen, W. G. Herrenden-Harker and R. H. Williams, Appl. Phys. Lett. **49**, 354 (1986).

[78] D. R. T. Zahn, K. J. Mackey and R. H. Williams, Appl. Phys. Lett. **50**, 742 (1987).

[79] Z. C. Feng, A. Mascarenhas, W. J. Choyke, R. F. C. Farrow, F. A. Shirland and W. J. Takei, Appl. Phys. Lett. **47**, 24 (1985).

[80] S. Adachi, Handbook on Physical Properties of Semiconductors (Springer Science + Business Media, New York, USA, 2004) vol. 2 & vol. 3.

[81] A. Janotti, S.-H. Wei and S. B. Zhang, Phys. Rev. B **65**, 115203 (2002).

[82] J. Lu, E. Luna, T. Aoki, E. H. Steenbergen, Y.-H. Zhang, and D. J. Smith, J. Appl. Phys. **119**, 095702 (2016).

[83] J. Lu, M. J. DiNezza, X.-H. Zhao, S. Liu, Y.-H. Zhang, A. Kovacs, R. E. Dunin-Borkowski and D. J. Smith, J. Cryst. Growth **439**, 99 (2016).

CHAPTER 2

EXPERIMENTAL METHODS

The development of semiconductor materials for infrared photo-detectors includes controlling the structural and compositional properties of the epitaxial layers, because both influence the energy band structure. The transmission electron microscope (TEM) provides a wide range of imaging, diffraction and spectroscopy techniques for characterizing these properties. In this chapter, the fundamental principles and experimental setups for the specific techniques used in this dissertation research are briefly described.

2.1. TEM Specimen Preparation

Transmission electron microscopy requires a specimen that is electron transparent, meaning that the specimen must be thin enough to allow sufficient transmitted electrons to form meaningful signals. The thickness needed to satisfy electron transparency depends on the accelerating voltage and the average atomic number of the material: different TEM techniques have different preferred thickness, but thicknesses in the range of a few nanometers to a few hundreds of nanometers are typical. This requirement means that bulk samples with epitaxial thin film structures grown by MBE must be thinned dramatically, preferably without compromising the microstructure and composition of the as-grown structure. The thinning can be achieved through well-designed progressive procedures (mechanical, chemical or ionic), in which initial coarse thinning is followed by successively finer thinning with reduced thinning speed, so that any damage induced in each step within certain specimen depth is removed by the subsequent steps [1].

Two types of TEM specimen preparation techniques have been utilized in this dissertation research as explained in more detail below. Dimple grinding followed by argon

ion milling is able to provide extensive thin regions, suitable for various TEM techniques that require different thicknesses. Focused-ion-beam (FIB) milling is site-specific and material efficient. Suitably thin TEM specimens can be prepared from targeted microscopic-scale areas of a few microns wide/long whereas dimple grinding needs a macroscopic-scale area of a few millimeters wide/long. However, the electron-transparent region in a FIB specimen is usually far smaller than obtainable in a dimpled specimen. In cases where the interfaces of epitaxial structures are of interest, cross-sectional thinning must be used so that the interfacial planes are parallel to the incident electron beam. All specimens examined in this dissertation research were prepared in the cross-sectional geometry.

2.1.1. Dimple Grinding and Low-Energy Ion Milling

The combination of dimple grinding and ion milling are based on mechanical abrasion and ionic displacement. First, the bulk sample is sliced with a wheeled saw (directional abrasion) into pieces with dimensions that are small enough to fit within the TEM holder (less than 3 mm in length). For extremely brittle materials (e.g., InSb substrate), cleaving instead of sawing is often used because of the limited stability when using the wheeled saw. For cross-sectional geometry, two sample pieces are glued together face-to-face to form a stack that helps protect the film surfaces during the following thinning steps. Second, mechanical polishing is carried out using diamond lapping film (with decreasing abrasive diamond grain sizes, e.g. 30, 9, 6, 3, 1 and finally 0.1 μm) and water as lubricant, to progressively thin the sample stack (usually to a thickness ~ 90 μm) with increasingly less surface/sub-surface damage. Third, the thin stack is further thinned under load with a dimple grinder using diamond paste (fine diamond grain size, e.g., 1 μm)

and polishing oil as lubricant, until the thinnest region of the dimple is ~ 10 μm. The fourth and final step, perforation around the dimple center, is achieved using argon-ion milling, with two ionized argon beams focused onto the rotating dimpled surface (one beam above the sample, the other below) at low inclination angles to gradually sputter material away from the surface. Argon is commonly used because it is inert, heavy and not usually present in semiconductors. The geometry of having one ion beam above the surface and another below is intended to remove material redeposited during the milling process [1]. The ion-milling is preferably carried out under liquid-nitrogen cooling and at the lowest available ion-beam energy (~ 2.1 keV using a Gatan precision ion polishing system) to reduce surface ion-beam damage [2].

2.1.2. Focused-Ion-Beam and Ultra-Low-Energy Ion Milling

In comparison to mechanical grinding plus ion milling, FIB milling provides precise site-specific sputtering/deposition capability using a finely focused ion beam. Nowadays, the commercial FIB is often integrated with a scanning electron microscope (SEM) to form an FIB/SEM dual-beam system, as shown in Figure 2.1 [3].

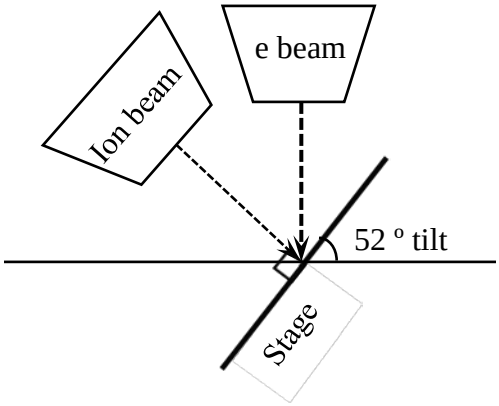

Figure 2.1 Column arrangement for FIB/SEM dual-beam system [3].

Such a system usually consists of a liquid-metal ion source, an electron source, a vacuum chamber, specimen stage, detectors and gas delivery system, all of which are computer controlled. Gallium is the customary ion source due to its low melting point, low volatility, and low surface free energy. Ionized Ga is extracted and subsequently accelerated by a variable potential (usually 5 ~ 30 kV), then focused and defined via suitable lenses and apertures to form an ion beam with controlled probe size and current. The sample is mounted on a stage that has five-axis motorized movement, namely, *x*, *y*, *z*, rotation and tilt, and eucentric-motion capability, to carry out the site-specific thinning and/or deposition. The electron beam is used for nondestructive imaging (no sputtering involved) and electron-beam-facilitated deposition, which has much less impact on the sample surface compared with ion-beam-assisted deposition [3].

One shortcoming of FIB milling is surface amorphization of the specimen, which is inherent to the ion-beam sputtering process. Even though the milling can be performed step-wise using decreasing ion-beam energies, which will induce increasingly less side-wall damage [4], for materials such as the group III-V and group II-VI semiconductors studied in this dissertation, the lowest reliable ion-beam energy (5 keV using the FEI FIB Nova NanoLab) still invariably causes significant damage. Sample cooling should help to reduce the ion-beam-induced damage but was unavailable. Alternatively, ultra-low-energy (e.g. 900 eV) ion-milling can gently clean the surfaces after FIB thinning [5]. This could be carried out, for example, with the Fischione NanoMill, which is designed for post-FIB cleaning.

2.1.3. Chemical Etching

The III-V semiconductor compounds, namely InAs and InSb, that have been studied in this dissertation are prone to ion-beam-induced damage during the final perforation step due to their moderate bonding strength. Thus, the thinned crystalline structures of interest are invariably sandwiched between two amorphized and partially damaged surface layers perpendicular to the thinning direction. This damage generates the so-called “salt-and-pepper” type of diffuse contrast which adds background noise to lattice-fringe images. This contrast often obscures the desired image details originating from the specimen and will bury any weak contrast generated by point defects [2]. The thickness of the damaged surface layers can be reduced by milling with lower ion-beam energy, although lower beam energy reduces the milling rate and prolongs the time to perforation. However, the argon-ion-milling equipment available at ASU only provided a minimum energy of about ~ 2.1 keV, which was insufficient to completely avoid the generation of damaged surface layers, even with liquid-nitrogen cooling.

Possible strategies to resolve these issues include: (1) Post-image-acquisition: processing images to filter out the diffuse background generated by the damaged layer. This approach may succeed if the objective is to enhance the contrast of crystalline structures, but may not work if the contrast is weak and diffuse in nature, such as the contrast originating from point defects, since most filtering techniques tend to impose false image periodicity and weaken the appearance of any aperiodic structures. (2) Pre-image-acquisition: perform chemical etching to physically remove the amorphized surface layers. There is considerable published literature and well-defined methodologies on this topic in the field of opto-electronical device fabrication using wet chemical etching, and well-tested

etchants. The major difference with the chemical etching approach discussed here is that the surface damage layers to be etched away are already very thin. Thus, the etchants must be significantly diluted to reduce the etching speed markedly. Hence, it becomes a matter of trial-and-error to identify the suitable concentration and ratio of the etchants, and the etching time needed to remove only the undesirable surface damage layers.

The etchants selected need to be a combination of hydrogen peroxide solution (H_2O_2, with deionized water) as oxidizer, and citric acid solution ($C_6H_8O_7$, with deionized water) as oxides/oxyhydroxides decomposition reagent, because: (1) organic acids such as citric acid can dissolve antimony oxides or oxyhydroxides (which are insoluble in water) and leave smooth etched surfaces [6]; (2) This combination has the capability to provide InAs/InSb etching selectivity of close to unity, meaning that the etching rates of InAs and InSb almost match [7].

The etchants were prepared using ACS-Reagent-grade reagents and separate volumetric flasks, and allowed to cool to room temperature before preparation. Two etchant solutions were mixed shortly before the etching experiments to prevent potential outgasing. Carbon-fiber-tipped tweezers were used instead of regular stainless-steel tweezers to avoid etchant contamination. Etching was consistently carried out at room temperature with the perforated TEM specimens being totally immersed in sufficient volume of etchant solution, which was mildly stirred by a Teflon-coated magnetic stirrer to ensure etchant freshness near the perforated regions of the TEM sample.

The superlattice samples used for this etching study consisted of 91.5 periods of 2.5-nm-thick $InAs_{1-x}Sb_x$ layers (antimony composition of 33 % from HRXRD) and 8.1-nm-thick InAs layers, sandwiched between two 10-nm-thick AlSb barrier layers and

capped with a 10-nm-thick InAs layer, and grown at 450 °C using the ASU's MBE (VG V80H) system. The TEM images in this section were recorded using a Philips-FEI CM200-FEG with an accelerating voltage of 200 kV and a structural resolution of 0.24 nm.

The first part of this etching experiment was to identify the approximate range of etchant concentration so that the etching rate was mild enough to avoid destroying the specimen. This step was carried out by applying etchants with ever-decreasing concentrations on mirror-like polished/dimpled specimen surfaces with short etching time (e.g. 1min), and observations under an optical microscope (magnification up to 1000X), until no visible surface etching occurred. The starting concentrations were $C_6H_8O_7$: H_2O =1g : 1mL, and H_2O_2 concentration = 31 % [7]. The next step involved trial runs with perforated TEM specimens to identify the close to ideal concentration range with proper etching speed. Finally, the recipe was optimized by fine-tuning the concentrations and the volume ratios of the two etchant solutions, keeping in mind that the etching power of the two etchants did not likely scale linearly with concentration. With the lack of any other technique to quantify the etching selectivity and rate, TEM image contrast of the etched specimens was used to guide the optimization process. During this final step of optimizing the etching recipe, variables such as concentrations and volume ratio of the reagent solutions, as well as etching time, were systematically adjusted.

Figure 2.2 shows a series of representative bright-field (BF) cross-sectional TEM (XTEM) images illustrating the structure of perforated TEM specimens etched with decreasing concentrations and etching time (from left to right). As the etchant concentrations and etching time were reduced, over-etching was alleviated, but problems such as etching non-uniformity and insufficient cleaning proved to be difficult to resolve.

It was found that the TEM specimens were significantly weakened in mechanical strength after etching, and most etched specimens failed to survive the loading procedure into the TEM holder, or afterwards into the high-vacuum TEM column. This serious drawback meant that the success rate of a complete etching experiment dropped drastically, on top of the limited success rate of preparing a perforated TEM specimen.

The best etching recipe identified to date was: citric acid (0.05 g/mL) : H_2O_2 (3 %) = 1 : 2 (volume ratio). The representative HREM image shown in Figure 2.3 demonstrates the relatively clean surface contrast. However, this recipe is not fully satisfactory since some sign of amorphous material still remains.

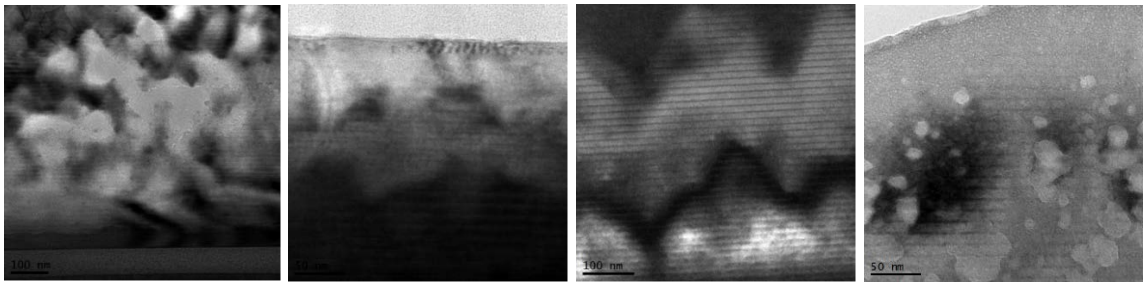

Figure 2.2 Representative BF XTEM images of etched TEM specimens with decreasing concentration and etching time from left to right.

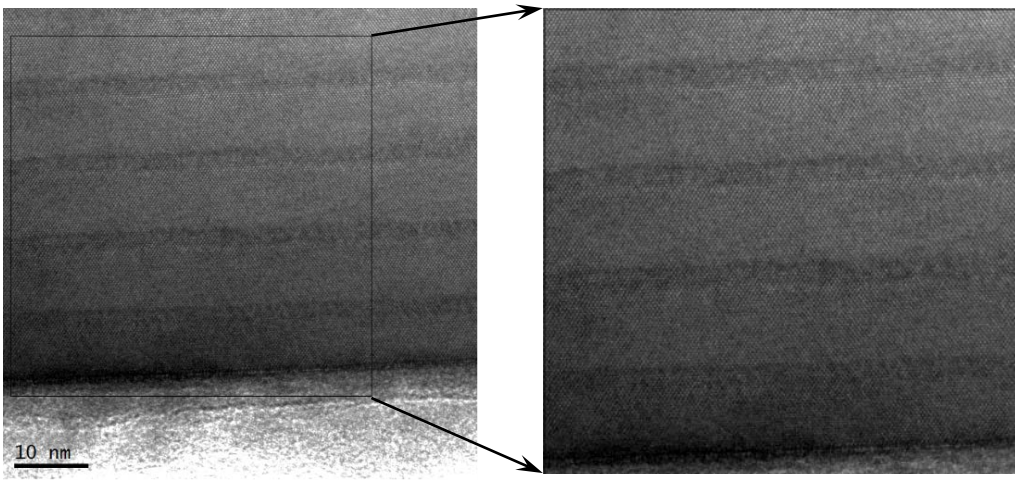

Figure 2.3 Representative HREM image of the superlattices etched by the best etching recipe evaluated to date.

The traditional method of TEM specimen preparation through mechanical polishing, dimple grinding and ion milling has limited success rate for the materials being studied. An alternative sample preparation method with higher speed and greater success would be beneficial for etching experiments that place heavy demands on the number and consistency of prepared TEM specimens.

Two major problems need to be addressed in any future continuation of this work: (1) alternative characterization schemes need to be developed to provide more detailed feedback on optimization of the etching process; and (2) safe transfer of the etched and mechanically weakened specimen into the TEM holder, and subsequently into the TEM column, and removal for proper storage (e.g. nitrogen-filled storage unit) must be identified.

The contrast in high-angle annular dark-field (HAADF) scanning transmission electron microscopy (STEM) images is less sensitive to the amorphized surface layers than HREM images, because such surface amorphous layers possess unordered structures, and compared to oriented crystalline structures they scatter relatively weakly in terms of high-angle incoherent scattering. Thus, HAADF STEM images may be preferred for analysis purposes until the issue of the damaged surface layers is resolved.

2.2. TEM Configurations and Techniques

The interaction of highly energetic electrons with crystalline semiconductors creates a range of different signals that can be utilized for characterization. The TEM can be configured in multiple ways to collect these signals, which offer complementary information about the specimen structure and composition.

Kinematical vs. dynamic scattering*:* Kinematical scattering assumes that the incident electron wave interacts weakly with matter [8] and only undergoes single

scattering. Theories based on kinematical scattering provide qualitative understanding of the interaction, but quantitative analysis requires consideration of dynamical scattering.

Coherent vs. incoherent scattering: Coherent scattering preserves the relative phase relationship between the unscattered and diffracted waves so that the diffracted intensity can be determined by adding the amplitudes of individual scattered waves. Conversely, incoherent scattering does not maintain any phase relationship, and the diffracted intensity can be obtained by summing intensities of the individual scattered waves [9].

Elastic vs. inelastic scattering: In inelastic scattering, some of the kinetic energy of the incident electron wave is lost or transferred during the electron-specimen interaction, whereas elastic scattering involves negligible change in kinetic energy of the electron wave after scattering [9].

These scattering events can be combined so that scattering by the sample can be coherent elastic, incoherent elastic, incoherent inelastic or coherent inelastic in nature. These different events create signals that provide complementary information about specimen structure and composition. For example, diffraction involves coherent elastic scattering, while spectroscopy studies involve incoherent inelastic scattering. Incoherent elastic scattering is used in high-angle annular-dark-field imaging, while coherent inelastic scattering is used in neutron scattering [9]. In the following sections, various TEM configurations used in this dissertation research are discussed.

2.2.1. Imaging Configurations

Image contrast can be considered in terms of the intensity difference between different areas of the specimen. To create useful and easily interpretable image contrast, signals need to be selectively collected or excluded in different TEM configurations.

2.2.1.1 TEM Imaging

Conventional TEM imaging can be categorized as either amplitude contrast or phase contrast, depending on the size of the objective aperture, and amplitude contrast can be further categorized as due to mass-thickness contrast or diffraction contrast. Amplitude contrast is prevalent in bright-field or dark-field (DF) imaging, where electrons in the transmitted beam or a Bragg diffracted beam are collected using a small objective aperture. Mass-thickness contrast originates from the incoherent elastic scattering (Rutherford scattering), and the scattering cross-section is related to the average atomic number Z and the thickness t of the specimen. Rutherford scattering has a wide angular range and is strongly forward peaked [10]. Diffraction contrast utilizes coherent elastic scattering, and reflects differences in Bragg diffraction conditions at different regions of the specimen. To obtain strong diffraction contrast, a special two-beam condition is preferred where only one diffracted beam is strongly excited besides the transmitted beam. Diffraction contrast is commonly used to study extended defects such as dislocations and stacking faults because these defects cause local bending of crystal planes, which induce local changes in the Bragg diffraction conditions. Mass-thickness contrast and diffraction contrast compete with each other at low scattering angles, and objective aperture of different size as well as specimen tilting may be needed to differentiate one from the other [10]. A chemically-sensitive type of DF imaging can be formed using Bragg diffraction when the structure

factor reflects differences in atomic scattering of the constituent elements, such as the {002} reflections of zincblende structured alloys [11].

Phase contrast primarily involves coherent elastic scattering. High-resolution TEM (HREM) is the most commonly used form of phase-contrast imaging, and the technique can provide specimen information with very high spatial resolution. In the axial-illumination BF configuration, an electron beam parallel with the optic axis interacts with the thin specimen which is usually tilted to a low-index, high-symmetry zone axis. Multiple diffracted beams are collected using a large objective aperture which allows them to interfere and form a lattice-fringe image. Such lattice-fringe images are capable of providing atomic-scale information depending on the imaging conditions, although the interpretation may require image simulations because the phase contrast is a complex interference pattern, with contrast determined by: (1) the interaction of the electron wave with the specimen, which is influenced by the specimen structure, orientation and thickness; and (2) the transfer of the information about the specimen structure that is transmitted through the microscope imaging system, which is influenced by the number of beams collected for imaging, the illumination coherence, and aberrations of the objective lens such as defocus, astigmatism and spherical aberration (C_s). These specimen-independent factors are incorporated in the so-called transfer function, which describes the modulation of the amplitude and phase of the electron wave by the objective lens. The transfer function is oscillatory in nature due to the spherical aberration of the objective lens, and results in bands of information transfer with opposite contrast and crossovers with no information transfer. Intuitive image interpretation is possible out to the interpretable resolution, defined as the first zero of the transfer function at Scherzer defocus, which maximizes the

spatial frequency range where the electron beam has nearly constant phase [12]. Correction of spherical aberration and other imaging aberrations can greatly enhance the useful resolution of the HREM. Although the dominant contrast of those TEM imaging modes relies mainly on elastically scattered electrons, inelastically scattered electrons around the direct beam and the Bragg diffracted beams will inevitably contribute diffuse background contrast to the image [13].

In this dissertation research, bright-field and high-resolution TEM imaging were carried out using a JEOL JEM-4000EX high-resolution electron microscope (housed at ASU) which was operated at an acceleration voltage of 400 kV, equipped with objective apertures with a range of sizes, and an interpretable resolution of 1.7 Å. 002 dark-field imaging was performed on a JEOL JEM 3010 transmission electron microscope operated at 300 kV (housed at Paul Drude Institute for Solid State Electronics, Berlin, Germany).

2.2.1.2 STEM Imaging

The configuration for scanning transmission electron microscopy consists of a demagnified electron source, scan coils to raster the finely focused electron beam across the specimen, and detectors of various geometries that collect scattered electrons. The relationship of TEM and STEM can be revealed by the principle of reciprocity, which states that the propagation of the electron wave in the microscope can be treated as reversible at least for elastic scattering. Thus, if the TEM detector plane is replaced with a source of electrons, and the TEM source is replaced by a detector, then similar image intensity/contrast will be obtained [14]. Commonly used STEM configurations can be selected using solid- or annular-disk detectors with collection semi-angles that can be controlled using the camera length setting: (1) Bright-field (BF) imaging, with a collection

semi-angle that is much smaller than the incident beam convergence semi-angle, collects the central part where the transmitted and diffracted disks overlap. Under such conditions, BF imaging uses coherently scattered electrons and demonstrates phase contrast, as in the equivalent case of HREM imaging [14]; (2) High-angle annular-dark-field (HAADF) mode, with collection inner and outer semi-angles several times the size of the beam convergence semi-angle. HAADF STEM imaging mainly involves incoherent elastic high-angle scattering [15], and can demonstrate mass-thickness contrast, which is often termed *Z*-contrast since the contrast mainly depends on the average atomic number of the specimen and its thickness. The spatial resolution for HAADF STEM imaging can be considered as being defined by the full-width-half-maximum of the intensity profile of the electron beam [15], and is usually limited by the spherical aberration of the objective lens, similar to the constraint on the interpretable resolution of HREM. Thus, correction of spherical aberration can result in smaller electron probes with higher current, providing higher spatial resolution and better image signal-to-noise ratio. (3) Medium-angle annular dark-field (MAADF), with the collection semi-angle low enough to include some Bragg diffraction scattering onto the detector, so that some diffraction contrast will contribute to image formation. (4) Large-angle bright-field (LABF) imaging, with a large collection semi-angle, comparable to the convergence semi-angle. The contrast mechanism is no longer phase contrast [16], but the technique has some advantages for imaging materials with similar atomic numbers since the image intensity is indirectly *Z*-dependent.

The STEM configuration also allows direct correlation of structural and compositional information through low-angle inelastically-scattered electron energy-loss

spectroscopy (EELS) and energy-dispersive X-ray spectroscopy simultaneous with STEM imaging [17].

In this dissertation research, HAADF STEM imaging and LABF STEM imaging were performed using an aberration-corrected JEOL ARM 200F operated at an acceleration voltage of 200 kV (located at Arizona State University), and an aberration-corrected FEI-Titan 80-200 (scanning) transmission electron microscope also operated at 200 kV (located at the Ernst Ruska-Centre for Microscopy and Spectroscopy with Electrons in Jülich, Germany). Both microscopes were equipped with Schottky field emission guns, and capable of providing of STEM spatial resolution of ~ 0.8 Å.

2.2.2. Diffraction Techniques

Diffraction is another important TEM capability since it allows access to crystallographic information such as the crystal structure, orientation, lattice spacing and misfit strain. There are several available diffraction techniques: selected-area electron diffraction (SAED), convergent-beam electron diffraction (CBED) and precession electron diffraction (PED); all three were utilized in this dissertation.

SAED: Selected-area electron diffraction is the classic TEM diffraction mode. An SAED pattern is obtained by illuminating the oriented specimen with a nearly parallel beam, and coherent elastic Bragg diffraction by the sample resulting in formation of a pattern of sharply focused spots; the diameter of the spots is determined by the incident beam divergence. An aperture of suitable size is then used to select a limited specimen area (effectively diameter of ~ 0.1 – 1 μm) at the first image plane of the objective lens [18]. The SAED pattern is routinely used to set up TEM BF and DF imaging conditions; it can also provide local crystallographic information, such as the crystal structure and orientation,

although the orientation determination may not be very accurate due to relaxation of the Bragg diffraction condition in thin specimen regions. Accurate crystal orientations can be achieved by referring to the Kikuchi lines which arise from elastic Bragg diffraction of inelastically scattered electrons in relatively thick specimen regions. There is unavoidable error in area selection by an SAED aperture due to spherical aberration of the objective lens, so that higher-order Bragg diffraction spots do not originate from the region selected by the SAED aperture [18].

***CBED**:* The convergent-beam electron diffraction pattern is formed when a small area of the specimen (usually ~ 1 – 10 nm in diameter) is illuminated by a focused beam with a finite convergence semi-angle. Instead of the sharp maxima observed at the back focal plane in the case of SAED, arrays of diffraction disks are formed, with the size of the disk determined by the effective angular size of the condenser aperture. CBED patterns can provide a wealth of information such as the point and space group of the specimen, accurate orientation and local specimen thickness [19]. The determination of lattice spacing parallel to the beam direction using the intersecting high-order Laue zone (HOLZ) lines within the direct disk is also of value. The *i*th-order Laue zone pattern arises from intersection of the Ewald sphere with the reciprocal lattice: assuming that *UVW* is the incident beam direction, and that *hkl* is the allowed diffraction spot, then $Uh + Vk + Wl = i$ defines the *i*th-order Laue zone. HOLZ lines are the loci of the Bragg diffraction conditions for high-order diffraction, and these lines occur in pairs, with the excess/bright lines present in the HOLZ rings, and deficient/dark lines present within the direct transmitted disk. The positions of the intersecting excess HOLZ lines in the 000 disk are very sensitive to the accelerating voltage and/or the lattice spacing: if the accelerating voltage is calibrated with a known

structure, and CBED patterns simulated with different lattice spacing using dynamical scattering theory are available, then lattice spacings can be determined with high accuracy, in practice up to 0.2 %, by matching the experimental pattern with simulation [20].

***PED**:* Precession electron diffraction is carried out by precessing a fine electron probe with parallel illumination around a circular hollow cone centered on an oriented specimen, and the diffraction pattern is collected by integrating the diffraction intensity throughout the beam precession. The electron beam is tilted away from the zone axis of the specimen at any point of the precession, so that only the direct beam and one diffracted beam are strongly excited, which is the case for the two-beam condition, meaning that the kinematical scattering condition is mostly satisfied. The recorded diffraction pattern can then be considered as quasi-kinematical, where dynamical scattering artifacts such as kinematically forbidden reflections are avoided. Such quasi-kinematical PED patterns can allow accurate characterization of the crystal structure, symmetry, orientation, lattice constant and misfit strain with high spatial resolution [21].

In this dissertation research, SAED patterns were recorded on a JEOL JEM-4000EX TEM operated at an acceleration voltage of 400 kV; study of excess HOLZ lines in CBED patterns for lattice spacing measurement were attempted using a JEOL 2010F at 200 kV and a JEOL ARM 200F STEM at 80 kV; and PED experiments for misfit strain mapping were carried out using a JEOL ARM 200F operated at 200 kV in TEM mode with the precessed beam scan/descan controlled by NanoMEGAS digital precession interface DigiSTAR [22].

2.2.3. Spectroscopy Techniques

When highly energetic electrons interact with the TEM specimen, a variety of signals are generated through scattering events that involve loss of energy of the incident beam: (1) secondary electrons, where the outer loosely-bound electrons in the conduction band are ejected by the incident electron beam; (2) inner-shell excitation, where electrons tightly bound in the core shells receive enough energy to be excited away from the atom; (3) plasmon resonance, with collective oscillation of the outer-shell conduction-/valence-band electrons; (4) phonons, where collective oscillations of the crystal lattice are generated; (5) Bremsstrahlung, or braking radiation, where the incident electrons are decelerated by the Coulomb field of individual atom, and photons with energies from zero up to the incident-beam energy are emitted [23]. Most of those inelastic scattering events can be exploited to gain characteristic information about the local chemical composition of the specimen.

2.2.3.1 Electron Energy-loss Spectroscopy

Electron energy-loss spectroscopy (EELS) utilizes the primary process of inelastic scattering of fast electrons by the specimen, and allows characterization of the electronic structure and determination of the element composition. EELS measures the energy distribution of the electron beam following its interaction and transmission through the thin specimen, and dispersion by a magnetic prism. The inelastically scattered electrons are strongly forward peaked, and have limited angular distribution in relation to the energy loss, so that reasonable collection efficiency is achievable. The EELS spectrum usually consists of: (1) the zero-loss peak (ZLP), the most intense peak of the spectrum, which includes unscattered electrons, elastically scattered electrons and electrons that experience

only phonon excitations. The ZLP acts as a reference energy for other energy-loss edges, and provides measurement of the energy resolution via its full-width half-maximum. (2) Low-loss range: typically ~ 5 – 50 eV in energy loss. The low-loss spectrum contains electronic information about the outer weakly-bound electrons. Plasmon peaks are prominent in the low-loss region, and provide a convenient approach for rough measurement of the local specimen thickness [24], as given by the expression:

$$t / \lambda = \ln(I_t / I_0) \tag{2.1}$$

Where λ is the total mean free path for all inelastic scattering events, I_0 is the intensity within the ZLP, and I_t is the intensity under the whole energy-loss spectrum. Single-electron excitation of outer-shell electrons may occur, and cause a valence electron to undergo interband transition over the bandgap into the conduction band. Thus, bandgap measurement is possible, provided that the influence of the ZLP tail is dealt with. (3) High-loss region: for energy losses of ~ 50 eV and more. This region contains elemental information (from excitation of the tightly bound inner-shell electrons) and also bonding details. A core-loss edge has an energy onset that is element-specific, and demonstrates well-defined edge shapes in relation to the electronic structure. Elemental composition can be extracted by analyzing the core-loss edge: typical procedures include background subtraction using power-law-fitting, edge integration, and quantification using partial ionization cross-section values (experimental or theoretical) [25]. A thin specimen is preferred for such quantification to avoid plural inelastic scattering. Otherwise, both the inner- and outer-shell electron excitations contribute to the intensity of the core-loss edge, and deconvolution will be needed to isolate the pure inner-shell excitation signal [26].

2.2.3.2 Energy-dispersive X-ray Spectroscopy

Energy-dispersive X-ray spectroscopy (EDS) utilizes the secondary emission process of inelastic electron scattering by the TEM specimen. Inner-shell electron ionization leaves the atom in an excited state. In the de-excitation process, an outer-shell electron, or an inner-shell electron with lower binding energy, relaxes and fills the unoccupied state. The excess energy is released in the form of electromagnetic radiation (X-ray, spherical wave) or by the kinetic energy of another electron (Auger electron) [23]. The energy of the emitted X-ray is determined by the energy difference of the two electron shells, and is thus element-specific. Such characteristic X-rays are usually collected by semiconductor-based detectors, and converted to voltage pulses proportional to their energy and thus dispersed by energy, and then analyzed for compositional information about the specimen. A typical EDS spectrum consists of: (1) the Bremsstrahlung X-ray background which is due to deceleration of the energetic electron by the nuclei, and is continuous up to the incident beam energy; (2) the characteristic X-ray peaks inherent to the illuminated specimen area; and some artifact peaks due either to the X-ray detector or else from other specimen regions, the specimen holder or even the microscope column [27]. Elemental composition can be obtained by analyzing the characteristic X-ray peaks of interest, which typically involves background subtraction via averaging pre- and post-peak background, peak integration with the same window width with background subtraction, and quantification using Cliff-Lorimer *k*-factors (experimental or theoretical). In contrast to the EELS technique, EDS requires thicker specimens in order to enhance the inherently sparse X-ray signal which is due to limited fluorescence yield, i.e., only a small fraction of the ionization events generate X-rays, as well as limited collection efficiency because the

emitted spherical X-ray wave is isotropic in space whereas the detector has limited solid angle [27].

When full EELS and/or EDS spectra are collected at each pixel, STEM images are combined with EELS and/or EDS to form spectrum imaging, which represents compositional information with high spatial resolution. Aberration correction in STEM results in significant reduction of probe size with simultaneous enhancement of the beam current, which greatly enhances the spatial resolution and analytical sensitivity [28]. The spectrum imaging in this dissertation research was carried out with an aberration-corrected JEOL ARM 200F STEM equipped with a reasonably-high-solid-angle, ultra-thin-window X-Ray detector and an Enfinium EELS spectrometer. This spectrometer is capable of dual-EELS acquisition when two separate spectra with different energy-loss ranges are recorded simultaneously. This feature allows simultaneous acquisition of zero-loss peak and core-loss edges which differ significantly in signal intensity.

References

[1] J. Ayache, L. Beaunier, J.Boumendil, G. Ehret and E. Laub, Sample Preparation Handbook for Transmission Electron Microscopy Methodology (Springer Science + Business Media, LLC, New York, 2010) p. 83.

[2] D. J. Barber, Ultramicroscopy **52**, 101 (1993).

[3] L. A. Giannuzzi and F. A. Stevie, Introduction to Focused Ion Beams (Springer Science + Business Media, Inc., Boston, 2005) p. 3.

[4] D. A. Cullen and D. J. Smith, J. Appl. Phys. **104**, 094304 (2008).

[5] A. Barna, B. Pecz and M. Menyhard, Ultramicroscopy **70**, 161 (1998).

[6] M. N. Kutty, E. Plis, A. Khoshakhlagh, S. Myers, N. Gautam, S. Smolev, Y. D. Sharma, R. Dawson, S. Krishna, S. J. Lee and S. K. Noh, Journal of Electronic Materials **39**, 2203 (2010).

[7] O. Dier, C. Lin, M. Grau and M.-C. Amann, Semicond. Sci. Tehcnol. **19**, 1250 (2004).

[8] B. Fultz and J. Howe, Transmission Electron Microscopy and Diffractometry of Materials, 3rd edition (Springer-Verlag Berlin Heidelberg, 2008) p. 224.

[9] B. Fultz and J. Howe, ibid., p. 122.

[10] D. B. Williams and C. B. Carter, Transmission Electron Microscopy: A Textbook for Materials Science, 2nd edition (Springer Science + Business Media, LLC, New York, 2009) p. 371.

[11] D. B. Williams and C. B. Carter, ibid., p. 263.

[12] D. J. Smith, Instrumentation and Operation and High Resolution Electron Microscopy, Vol. 11 of Advances in Optical and Electron Microscopy (Academic Press, London, New York, 1989) p. 12.

[13] L. Reimer and H. Kohl, Transmission Electron Microscopy: Physics of Image Formation, 5th edition (Springer Science + Business Media, LLC, New York, 2008) p. 369.

[14] J. M. Cowley, Appl. Phys. Lett. **15**, 58 (1969).

[15] B. Fultz and J. Howe, ibid. 8, p. 583.

[16] T. Aoki, J. Lu, M. R. McCartney and D. J. Smith, Semicond. Sci. Technol. **31**, 094002 (2016).

[17] S. J. Pennycook and P. D. Nellist, Scanning Transmission Electron Microscopy: Imaging and Analysis (Springer Science + Business Media, LLC, New York, 2011) p. 163.

[18] L. Reimer and H. Kohl, ibid. 13, p. 329.

[19] J. C. H. Spence and J. M. Zuo, Electron Microdiffraction (Springer Science + Business Media, New York, 1992) p. 146.

[20] J. C. H. Spence and J. M. Zuo, ibid., p. 20.

[21] D. B. Williams and C. B. Carter, ibid. 10, p. 295.

[22] www.nanomegas.com

[23] D. C. Joy, A. D. Romig, Jr. and J. I. Goldstein, Principles of Analytical Electron Microscopy (Plenum Press, New York, 1986) p. 12.

[24] R. F. Egerton, Electron Energy-Loss Spectroscopy in the Electron Microscope, 3rd edition (Springer Science + Business Media, LLC, New York, 2011) p. 302.

[25] D. C. Joy, A. D. Romig, Jr. and J. I. Goldstein, ibid. 22, p. 254.

[26] R. F. Egerton, ibid. 23, p. 249.

[27] R. Brydson, Aberration-Corrected Analytical Transmission Electron Microscopy (John Wiley & Sons, Ltd. West Sussex, UK, 2011) p. 189.

[28] S. J. Pennycook and P. D. Nellist, ibid. 17, p. 307.

CHAPTER 3

DILUTE InAsBi BISMIDE ALLOYS

The research described in this chapter was carried out in collaboration with Dr. Preston T. Webster, Dr. Shi Liu, Prof. Yong-Hang Zhang and Dr. Shane R. Johnson at Arizona State University. My role in this collaboration involved structural characterization of the dilute bismide alloys using transmission electron microscopy. Important results from this study have been published [1, 9].

3.1. Introduction

III-V-Bi alloys have potential applications in uncooled long-wavelength infrared photo-detectors and lasers due to their large band-gap reduction (valence-band engineering, as opposed to conduction-band engineering in nitrides), spin-orbit splitting and relatively temperature-insensitive band gap. Thus, the synthesis of dilute bismides using different growth techniques has been actively pursued to take advantage of such properties [2, 3]. Despite the great promise of the dilute bismides, the successful growth of such thin films is very challenging and suffers from a large miscibility gap because the alloys are formed through isoelectronic substitution of group-V atoms with very different sizes [3]. MBE growth and microstructural studies of epitaxial $GaAs_{1-x}Bi_x$ films have shown that the morphology departs from homogeneity in several ways, including phase separation, atomic ordering and surface-droplet formation [4-6], despite all the efforts directed towards optimizing growth. In comparison, the growth of $InAs_{1-x}Bi_x$ epitaxial layers were mostly done by organometallic vapor phase epitaxy [7], and growth by MBE has only recently been initiated [8, 9]. Thus, there is an urgent need for a detailed microstructural study of

such alloys to facilitate the development of this material system towards applications such as optoelectronics.

The samples examined here were grown on GaSb (001) substrates using a VG-V80H solid-source MBE system. The two $InAs_{1-x}Bi_x$ samples (maximum [Bi] ~ 4.5 % and ~ 5.8 %) were grown at a substrate temperature ~ 280 °C with different V/III flux ratios. The relatively low growth temperature was chosen because it was regarded as favorable for incorporating bismuth. As shown by the schematic in Figure 3.1, after growth of the 600-nm-thick GaSb buffer layer, a 15-nm-thick InAs spacer layer was grown, followed by a 1-μm-thick $InAs_{1-x}Bi_x$ film and a 10-nm-thick InAs capping layer.

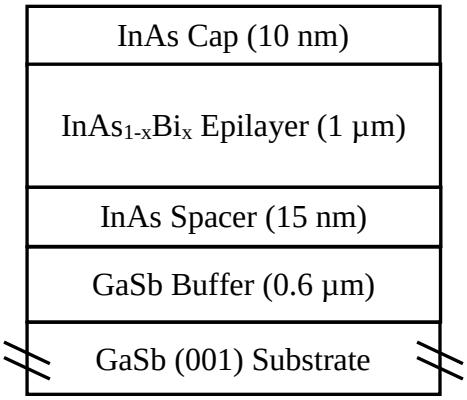

Figure 3.1 Schematic of structures grown on GaSb (001) substrates.

TEM specimens were prepared for cross-sectional observation along <110>-type projections using standard mechanical polishing and dimple grinding, followed by argon-ion-milling (maximum beam energy 2.3 keV) with liquid-nitrogen cooling in order to reduce ion-beam damage [10]. Electron microscopy was performed using a JEOL JEM-4000EX high-resolution electron microscope with an accelerating voltage of 400 kV and structural resolution of 0.17 nm. Geometric phase analysis (GPA) to extract information

about interfacial misfit strain was applied to the high-resolution electron micrographs using a Digital Micrograph script [11].

3.2. As-Grown Structures

All surfaces of the $InAs_{1-x}Bi_x$ films had smooth droplet-free regions and hazy droplet-forming regions [9]. Measurements using X-ray diffraction (XRD) indicated less Bi incorporation under the hazy regions of the $InAs_{1-x}Bi_x$ films. Moreover, broadened X-ray peaks were observed for the droplet-free regions, suggesting non-uniform composition [9]. Reciprocal space maps in the vicinity of the (115) reflection indicated that the InAsBi layers were pseudomorphically strained to the GaSb substrate.

The first sample studied by TEM had a maximum Bi incorporation of 5.8 % as measured by (004) ω-2θ high-resolution XRD scan, assuming a theoretical lattice-constant calculation for InBi. A TEM sample was prepared from the droplet-free region. As indicated by the bright-field image in Figure 3.2 (a), very few structural defects were visible over wide lateral distances. Selected-area electron diffraction patterns, as shown by the inset, gave no indication of atomic ordering along this viewing projection. Diffraction-contrast images such as Figure 3.2 (b) gave contrast primarily enhanced by differences in mass/thickness, because the imaging condition was set up with a relatively large objective aperture and tilting off the zone axis such that Bragg diffraction contrast was weakened. The vertical stripe features visible in this micrograph thus indicate the occurrence of lateral compositional modulations on the scale of several tens of nanometers.

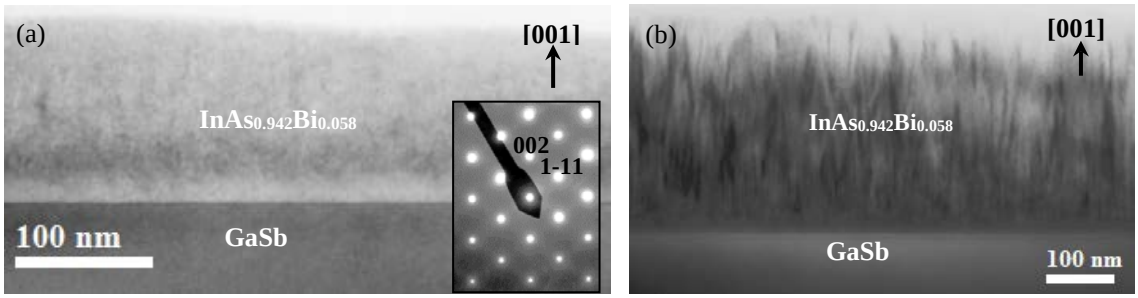

Figure 3.2 (a) Bright-field TEM image of $InAs_{0.942}Bi_{0.058}$ alloy sample and the corresponding selected-area electron diffraction pattern (inset); (b) diffraction contrast image showing vertical stripe features, indicating lateral compositional modulation.

This type of vertical stripe feature was generally present in all regions of the InAsBi samples studied, which had growth temperature of 280 °C, different Bi % in the range of 4.5% to 5.8%, with or without surface droplets. This reflects the difficulty of incorporating Bi into the small InAs matrix, with the growth conditions not fully optimized.

The subsequent interfaces of GaSb substrate, GaSb buffer layer and InAs spacer appeared to be largely free of extended defects, and all epi-layers were regarded as being effectively constrained to the GaSb substrates in a coherent manner.

High-resolution electron micrographs were taken close to the substrate, and near the top of the film, to investigate the interfacial coherence of the $InAs_{1-x}Bi_x$ films as shown in Figure 3.3 (a) and Figure 3.4 (a), respectively. These lattice-fringe images confirm the excellent crystallinity of the film. The technique of geometric phase analysis can then be used to extract both in-plane and out-of-plane misfit strain across the epitaxial layers, where the out-of-plane misfit strain (in the [001] growth direction) due to the tetragonal distortion of the alloy lattice is defined by the expression:

$$\xi_{zz} = \frac{c_{\text{alloy}} - c_{\text{reference}}}{c_{\text{reference}}} \tag{3.1}$$

In Eq. (3.1), c is the lattice parameter along the growth direction.

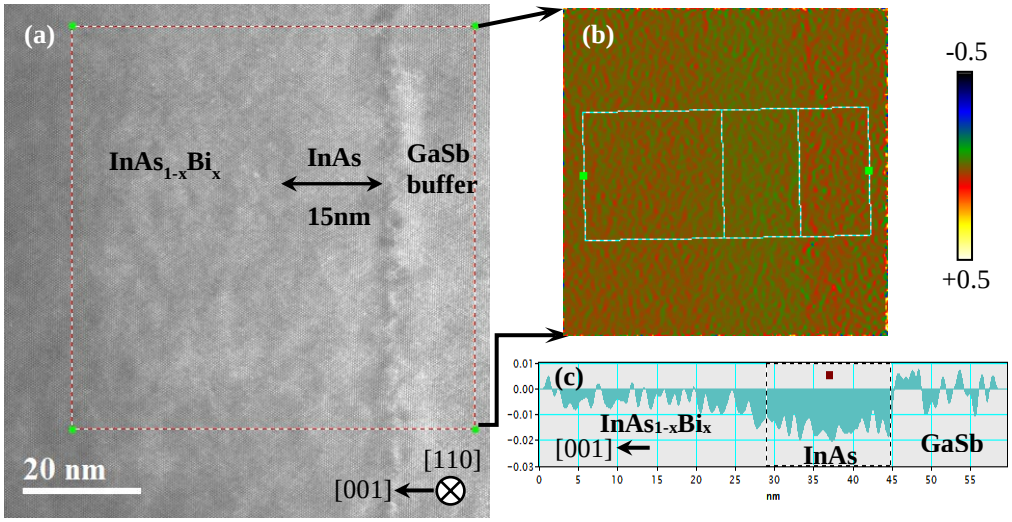

Figure 3.3 (a) High-resolution image of $InAs_{0.942}Bi_{0.058}$ sample showing region close to the GaSb buffer, (b) corresponding out-of-plane misfit strain map, and (c) average misfit strain line profile.

The in-plane misfit strain (not shown) extracted from both images was negligible, as expected. For out-of-plane misfit strain analysis of the lattice-fringe image recorded close to the substrate, the unstrained GaSb buffer layer was used as the reference in Eqn. (1). In Figure 3.3, the InAs spacer under tensile misfit strain was readily identifiable in the misfit strain map, and in the averaged line profile (averaged perpendicular to the growth direction). Bi started incorporating into the $InAs_{1-x}Bi_x$ layer shortly if not immediately after the end of growth of the InAs spacer layer, as evident from the reduced tensile misfit strain in the $InAs_{1-x}Bi_x$ layer compared with that in the InAs spacer. Bi incorporation increased the lattice spacing in the $InAs_{1-x}Bi_x$ film, which is similar to the lattice expansion observed in GaAsBi [12], but contrary to the cases of lattice contraction for GaSbBi or InSbBi [13]. Thus, the lattice mismatch is reduced with respect to the unstrained GaSb buffer. However, insufficient Bi was incorporated to achieve exact lattice match so that the $InAs_{1-x}Bi_x$ layer remained under slight tensile misfit strain.

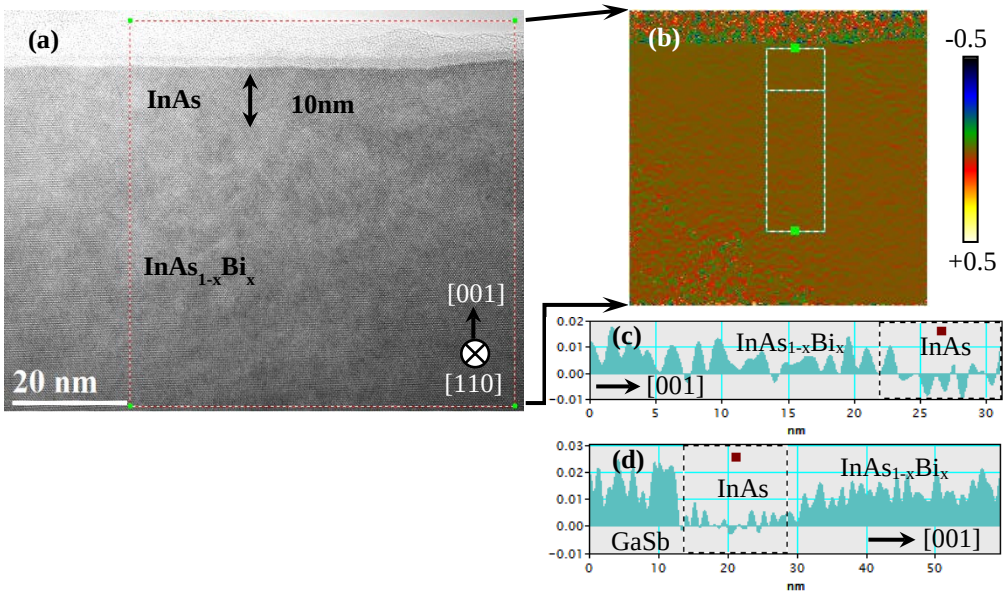

Figure 3.4 (a) High-resolution image of $InAs_{0.942}Bi_{0.058}$ sample showing region close to the top InAs capping layer, (b) corresponding out-of-plane misfit strain map, (c) average misfit strain line profile, and (d) average out-of-plane misfit strain line profile obtained from further GPA analysis of Figure 3.3 (a) using InAs as the reference.

Figure 3.4 (a) shows excellent crystallinity near the top surface, and the coherent interface between the $InAs_{1-x}Bi_x$ film and the InAs capping layer. GPA analysis again brings out the misfit strain information embedded in the high-resolution micrographs, and the out-of-plane misfit strain map obtained is shown in Figure 3.4 (b). In this case, the InAs capping layer was used as the reference. Thus, the $InAs_{1-x}Bi_x$ was under compressive misfit strain as shown by the positive misfit strain value in the averaged line profile (Figure 3.4 (c)). A qualitative comparison of the averaged out-of-plane misfit strain in the $InAs_{1-x}Bi_x$ film close to the cap in Figure 3.4 (c) and close to the substrate (Figure 3.4 (d), obtained from further GPA analysis of Figure 3.3 (a) but using InAs as the reference) shows that the misfit strain difference of the InAs cap and the top region of the $InAs_{1-x}Bi_x$ film is less than

that of the InAs spacer and the bottom region of the $InAs_{1-x}Bi_x$ film, indicating that less Bi was incorporated near the top of the film.

The second sample investigated by TEM had a maximum Bi incorporation of 4.5 %, as determined from analysis of the (004) ω-2θ high resolution XRD patterns. In this case, the TEM sample was prepared from the droplet-forming region. The bright-field image in Figure 3.5 (a) shows vertical stripe features similar to Figure 3.2 (b), as well as surface droplets at the surface (example arrowed in Figure 3.5 (b)). No apparent atomic ordering was visible, although horizontal growth defects were sometime observed for this particular sample - see the example in Figure 3.5 (b).

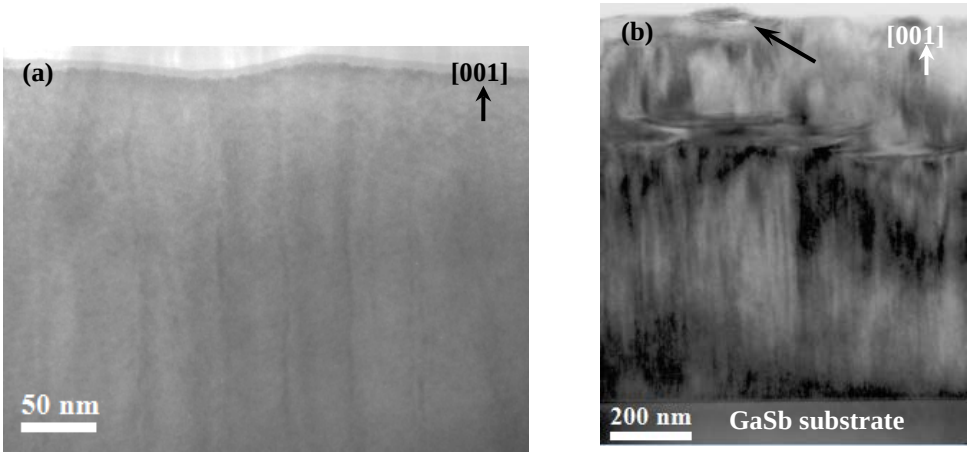

Figure 3.5 (a) Bright-field TEM image of $InAs_{0.955}Bi_{0.045}$ sample, and (b) diffraction contrast image showed vertical stripe features, indicating lateral compositional modulation. Horizontal growth defects also visible.

The lattice-fringe image of a representative surface droplet, which is about 100 nm in length and 40 nm in maximum height, is shown in Figure 3.6 (a). Twinning and V-shaped surface grooves ((111) surface faceting) were observed in the droplet. Fast-Fourier-transform analysis was performed from regions of the capping layer (Figure 3.6 (b)) and the droplet (Figure 3.6 (c)), respectively, and the measured spacings of different lattice

planes and angles are labelled. Judging from the length ratio and the angle between diffraction vectors in the diffractogram, the surface droplet has adopted a distorted zincblende structure, with a lattice constant in the range of 0.64 - 0.67nm and an ~ 80° rotation away from the matrix. EDX analysis performed on various positions of the droplet indicated that it consisted predominantly of Bi. In comparison, Bi-rich zincblende Ga(As, Bi) clusters and rhombohedral Bi clusters were reported for GaAsBi after annealing [14], and InBi clusters with distorted PbO structure were reported in InAsBi [8]. Such phase separation has been attributed to the difficulties associated with Bi incorporation.

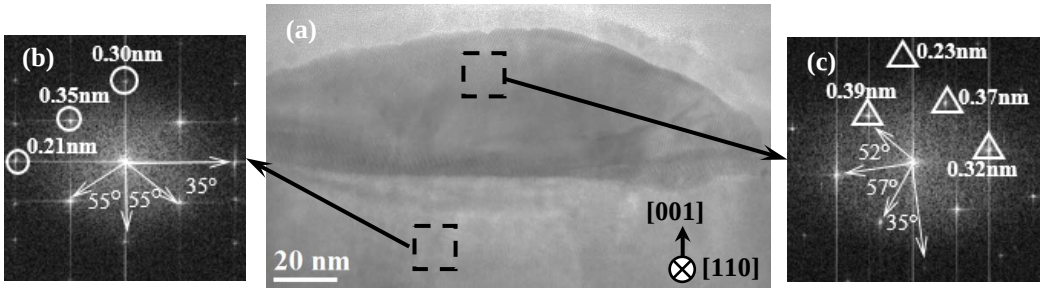

Figure 3.6 (a) High-resolution image showing surface droplet on the $InAs_{0.955}Bi_{0.045}$ film. Fast Fourier transform from square region of interest chosen in (b) capping layer, (c) droplet region, with measured spacings of different lattice planes and angles as shown labelled.

3.3. Future Work: Bismuth Compositional Modulation

The BF XTEM analysis presented in the previous section revealed the existence of lateral Bi compositional modulations. The vertical stripe features indicate that regions relatively rich and poor in Bi composition alternate laterally, similar to what has been reported in $GaAs_{1-x}Bi_x$ alloys grown by MBE [15]. Two methods are currently under consideration to facilitate investigation of the compositional modulation:

(1) Perform HAADF STEM imaging at high magnification, and use GPA to extract the misfit strain as related to Bi compositional distribution. GPA analysis of HREM images

has yet to reveal such misfit strain information, indicating that the misfit strain variation related to Bi compositional modulation is relative subtle. Thus, care will need to be taken to select the proper imaging conditions to decompose the strain tensor, and to avoid the influence of any scan distortion.

(2) Perform energy-dispersive X-ray spectroscopy in scanning mode, to map out the compositional distribution of Bi. Quantification of Bi composition from EDX spectrum maps may be difficult because: (a) the X-ray signal from low Bi % in InAsBi may well be small; (b) the theoretical calculation of k-factors for heavy elements such as Bi has large error.

Another possible interesting topic for further research is to study the similarities and differences between $InAs_{1-x}Bi_x$ and $GaAs_{1-x}Bi_x$, which could provide useful insights into the growth and engineering of bismides in general.

References

[1] J. Lu, P. T. Webster, S. Liu, Y.-H Zhang, S. R. Johnson and D. J. Smith, J. Cryst. Growth **425**, 250 (2015).

[2] K. Oe and H. Asai, IEICE Trans. Electron **E79C**, 1751 (1996).

[3] H. Li and Z. M. Wang, Bismuth-Containing Compounds (Springer Science + Business Media, New York, 2013) p. 2.

[4] S. Tixier, M. Adamcyk and T. Tiedje, Appl. Phys. Lett. **82**, 2245 (2003).

[5] G. Vardar, S. W. Paleg, M. V. Warren, M. Kang and R. S. Goldman, Appl. Phys. Lett. **102**, 042106 (2013).

[6] M. Wu, E. Luna, J. Puustinen, M. Guina and A. Trampert, Appl. Phys. Lett. **105**, 041602 (2014).

[7] K. Y. Ma, Z. M. Fang, R. M. Cohen and G. B. Stringfellow, J. Cryst. Growth **107**, 416 (1991).

[8] L. Dominguez, D. F. Reyes, F. Bastiman, D. L. Sales, R. D. Richards, D. Mendes, J. P. R. David and D. Gonzalez, Appl. Phys. Express **6**, 112601 (2013).

[9] P. T. Webster, N. A. Riordan, C. Gogineni, S. Liu, J. Lu, X.-H. Zhao, D. J. Smith, Y.-H. Zhang and S. R. Johnson, J. Vac. Sci. Technol. B **32**, 02C120 (2014).

[10] C. Wang, S. Tobin, T. Parodos, J. Zhao, Y. Chang, S. Sivananthan and D. J. Smith, J. Vac. Sci. Technol. A **24**, 995 (2006).

[11] M. J. Hÿtch, E. Snoeck and R. Kilaas, Ultramicroscopy **74**, 131 (1998).

[12] Y. Takehara, M. Yoshimoto, W. Huang, J. Saraie, K. Oe, A. Chayahara and Y. Horino, Jpn. J. Appl. Phys. **45**, 67 (2006).

[13] S. Wang, Y. Song and I.S. Roy, 13th International Conference on Transparent Optical Networks (ICTON), IEEE, New York, USA (2011).

[14] M. Wu, E. Luna, J. Puustinen, M. Guina and A. Trampert, Nanotechnology **25**, 205605 (2014).

[15] M. Wu, M. Hanke, E. Luna, J. Puustinen, M. Guina and A. Trampert, Nanotechnology **26**, 425701 (2015).

CHAPTER 4

InAs/InAsSb TYPE-II SUPERLATTICES

The work described in this chapter was carried out in collaboration with Dr. Esperanza Luna at Paul-Drude Institute in Berlin, Dr. Toshihiro Aoki and the group of Prof. Yong-Hang Zhang at Arizona State University. My role involved characterization of antimony compositional distribution within the MBE-grown superlattices using transmission electron microscopy. Major results from this study have been published [1].

4.1. Introduction

Mercury cadmium telluride (MCT) semiconductor alloys remain the most widely used materials for infrared (IR) photo-detection in mid-wavelength and long-wavelength ranges despite major disadvantages of weak mechanical strength, intrinsic Auger recombination and small effective mass [2]. Type-II superlattices (T2SL) have been proposed as promising alternatives because they may overcome the MCT problems by providing flexible and more controllable band-gap engineering through design of the superlattice layer thickness/composition and coherency strain, as well as giving additional benefits including larger effective masses, better Auger suppression, higher mechanical strength and lower relative cost [2, 3]. The most widely studied III-V T2SL system, InAs/$Ga_{1-x}In_xSb$, suffers from short minority carrier lifetimes, most likely due to Shockley-Reed-Hall recombination induced by Ga-related native defects [4]. Ga-free InAs/$InAs_{1-x}Sb_x$ T2SLs, on the other hand, have since demonstrated significantly improved minority carrier lifetimes relative to their Ga-containing counterparts [5, 6]. These Ga-free T2SLs can be routinely grown with high structural quality provided care is taken in the design of superlattice structures concerning the misfit strain and the control of growth parameters [7,

8]. Hence, Shockley-Reed-Hall recombination associated with extended defects is no longer likely to be limiting the minority carrier lifetime.

It is of considerable interest to investigate the global homogeneity of the superlattices, the local compositional distribution at interfaces, and ultimately possible point defects. The compositional distribution of antimony is especially important because the superlattice structures are realized through incorporation of Sb into InAs with controlled spatial position and concentration. Fluctuations in InAsSb layer thickness and/or Sb composition throughout the superlattice stack as well as interface chemical diffuseness have been suggested by high-resolution X-ray diffraction, scanning tunneling microscopy and transmission electron microscopy [7, 9-13]. It is of importance to provide a quantitative evaluation of such non-uniformity and diffuseness, because either of these factors could introduce perturbations to the superlattice band structure, causing deviations from the design and possible deterioration of the optoelectronic response.

Transmission electron microscopy can be highly effective in studying structural and compositional properties of semiconductor structures with different imaging, diffraction and analytical techniques having a wide range of spatial resolution. Efforts have been directed towards understanding compositional properties of the as-grown superlattices at fine scale. Specific topics of interest include, but are not limited to: chemical etching of TEM specimen for enhanced contrast, fluctuation in superlattice layer thickness (and antimony composition) throughout the stack, interface diffuseness due to antimony segregation and the possible effect of bismuth surfactant on the diffuseness.

The InAs/$InAs_{1-x}Sb_x$ superlattices studied here were designed for mid-wave infrared photo-detection, and consist of 58.5 periods of 1.8-nm-thick $InAs_{1-x}Sb_x$ layers

(nominally antimony composition of 40 %, HRXRD gave an average of 34 %) and 6.8-nm-thick InAs layers, sandwiched between two 10-nm-thick AlSb barrier layers and capped with a 10-nm-thick InAs layer (see Figure 4.1 for a schematic of the general structure). The T2SLs were grown using molecular beam epitaxy without any special interface treatment on unintentionally-doped 2"-diameter GaSb nominal-(001) wafers at a temperature of 405 °C in IQE Inc., with a beam-equivalent pressure of In/As fixed at 5.5, and with the Sb flux being adjusted instead of As flux for alternating the growth of InAs and $InAs_{1-x}Sb_x$ layers [5].

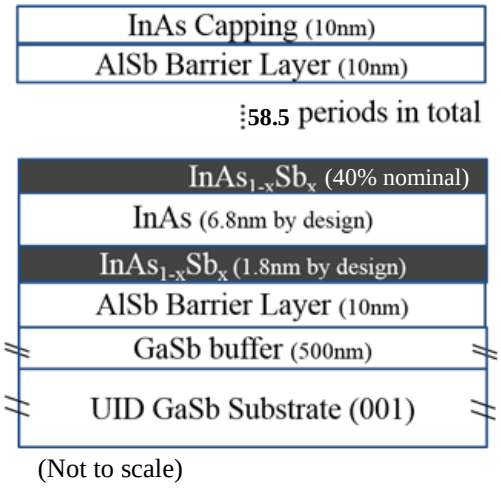

Figure 4.1 Schematic of the type-II superlattice structure under study.

Cross-sectional TEM samples suitable for imaging, diffraction and spectroscopy study along <110> and <210> projections were first progressively thinned using mechanical polishing and dimple grinding, and finally perforated using argon-ion-milling (maximum energy of 2.3 keV) with liquid-nitrogen cooling to help reduce ion-beam-induced damage.

HREM and HAADF STEM images of the superlattices at the bottom region close to the substrate, the middle region and the top region close to the capping layer, have been

recorded to investigate the variation of the superlattice layer thickness. HREM and HAADF STEM images were respectively recorded using a JEOL JEM-4000EX high resolution electron microscope with an accelerating voltage of 400 kV and structural resolution of 0.17 nm, and an aberration-corrected JEOL ARM200F TEM/STEM operated at 200 kV with a highly focused probe size of 0.08 nm. The collection half-angle of the dark-field detector covers the range of 90 – 170 mrad.

4.2. Variations in Superlattice Layer Thickness

The asymmetric superlattice peaks present in HRXRD rocking curves (Figure 4.2) and their comparison with simulations suggest fluctuations of superlattice layer thicknesses, and/or variation of the Sb composition in the InAsSb layers throughout the whole superlattice stack. Such variations will directly influence band-gap engineering, or may even induce carrier localization [14].

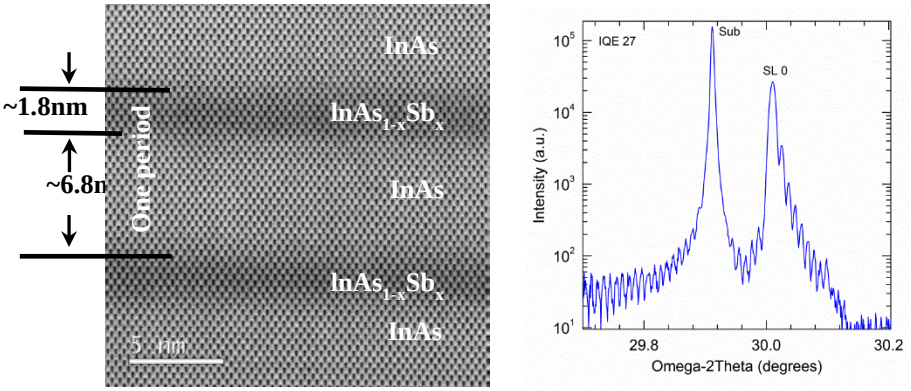

Figure 4.2 BF STEM image of superlattices, and portion of ω-2θ (004) high-resolution X-ray diffraction rocking curve.

The method used to analyze fluctuations in layer thickness is based on analysis of the contrast in HREM and HAADF STEM images. The assumption is that the alternating layers of InAs and InAsSb have been faithfully recorded in both HREM and STEM (with correct defocus and suitable specimen thickness). Thus, although different contrast

mechanisms are involved (phase contrast for HREM and incoherent imaging for STEM), analysis of contrast evolution should provide insight into the causes, effectively the Sb distribution.

HREM and HAADF STEM images taken from the top, middle and bottom superlattice regions, respectively, are shown in Figure 4.3.

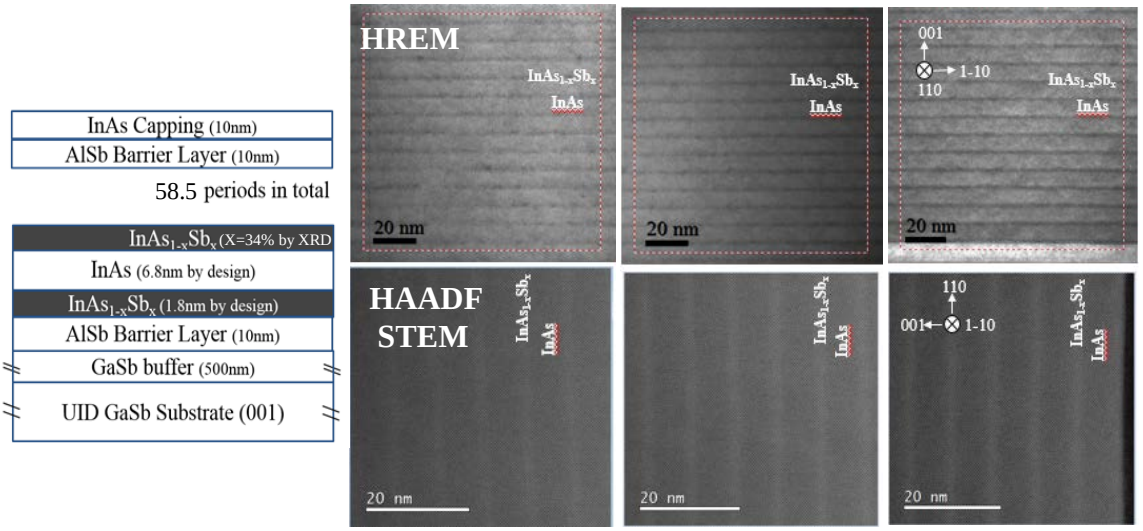

(a) (b) Top SL (c) Middle SL (d) Bottom SL

Figure 4.3 (a) Schematic of structure under study; HREM (top row) and HAADF STEM (bottom row) images of (b) top, (c) middle, and (d) bottom, SL regions.

Average background subtraction filtering (ABSF) was performed on the HREM images [15] to remove the diffuse background intensity generated mainly by the amorphized surface layers of the TEM specimen. Intensity line profiles were then extracted and the layer thickness was defined as the distance between two neighboring mid-intensity points on the line profile (see Figure 4.4).

Layer thickness measurements from the HREM and HAADF STEM images are summarized in Table 4.1, where the standard deviation is defined as: $= \sqrt{\sum_{i=1}^{N} (x_i - \bar{x})^2 / (N-1)}$.

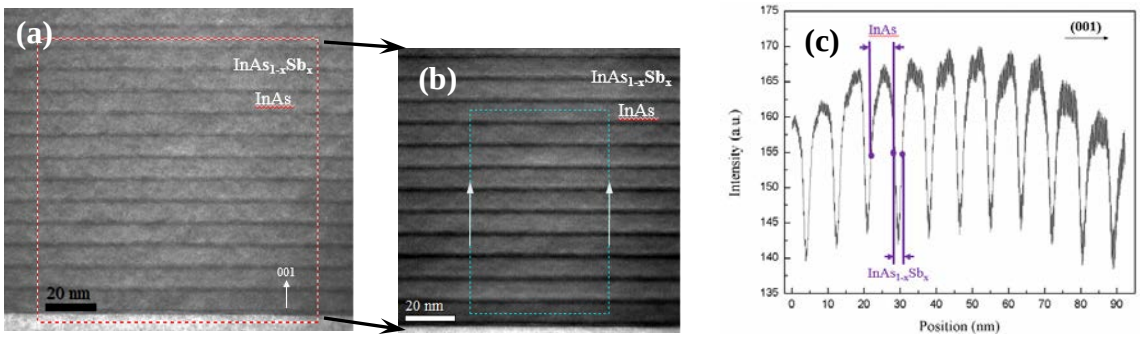

Figure 4.4 HREM images: (a) as recorded; (b) after ABSF filtering; and (c) extracted averaged intensity line profile.

Table 4.1 Summary of layer thickness measurement from HREM and HAADF STEM images.

		Bottom SL/nm			Middle SL			Top SL		
		InAs	InAsSb	Period	InAs	InAsSb	Period	InAs	InAsSb	Period
HREM	Average	6.60	2.11	8.71	6.49	1.99	8.48	6.12	2.47	8.60
	SDV	0.17	0.19	0.21	0.05	0.03	0.06	0.19	0.12	0.11
HAADF STEM	Average	6.05	2.60	8.65	6.32	2.31	8.62	6.23	2.42	8.65
	SDV	0.27	0.28	0.21	0.18	0.20	0.20	0.27	0.16	0.21

The overall thickness of the SL period roughly maintained the 8.6-nm design value during growth, but the InAsSb layer was thicker than the design value throughout the whole SL stack, while the InAs layer was thinner. This likely indicates that Sb has segregated into the following InAs layer during growth. Closer examination shows that the InAsSb layer thickness first slightly decreases then significantly increases along the growth direction, with the top InAsSb thicker than the bottom InAsSb layer. This change could be due to either variation of Sb composition and/or Sb diffusion during growth.

Graphical presentation of the measurement summary is shown in Figure 4.5. It is difficult to directly compare the measurement of superlattice layer thickness obtained from HREM and HAADF STEM images, since different regions of the same TEM specimen were investigated and different contrast mechanisms were involved. Future work should aim: (1) to develop a more objective and consistent definition of the layer thickness; (2) to remove the background intensity in HREM and HAADF STEM images due to thickness variation because this profile shifts the intensity maxima and minima and thus alters the layer thickness measured from the intensity profile. The background in HAADF STEM images tend to follow linear behavior [16] and can be subtracted more reliably than the generally non-linear background present in HREM images; (3) to perform statistical analysis of interface position and width, feed values into the carrier localization model, and then correlate with photoluminescence study.

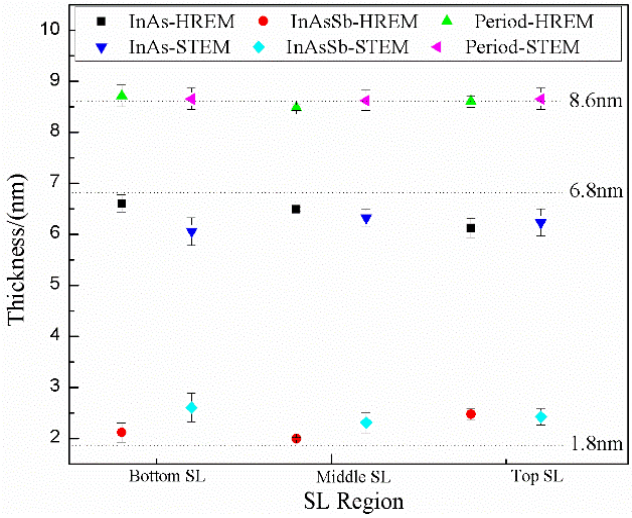

Figure 4.5 Summary of measurement of superlattice layer thickness from HREM and HAADF STEM images.

4.3. Interface Abruptness

Evidence exists for the presence of interface diffuseness at the interface of InAs-on-InAsSb from scanning tunneling microscopy and transmission electron microscopy [7, 9-12], possibly due to Sb segregation. This diffuseness also seems apparent from many of the experimental HREM and high-resolution STEM images (Figure 4.6).

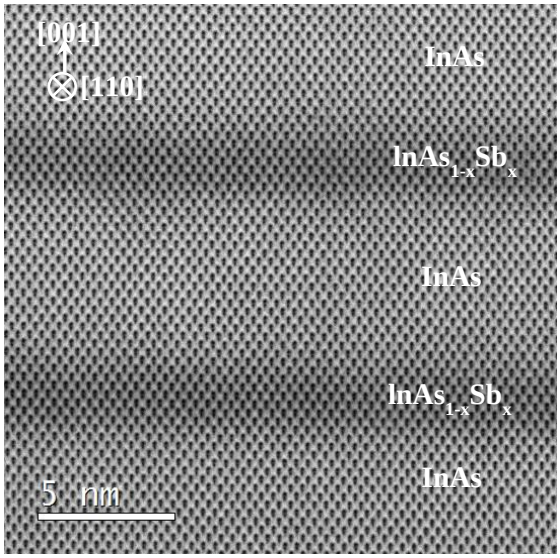

Figure 4.6 BF STEM image showing the relatively diffuse interface of InAs-on-InAsSb compared with InAsSb-on-InAs.

It is important to understand the nature of the interface because this directly impacts band-gap engineering parameters such as the thickness of the InAsSb layer, maximum Sb incorporated in InAsSb layers, and coherency strain. Possible causes of the interface diffuseness include: (1) the experimental interface has a graded compositional profile rather than abrupt, which is assumed during structure design; (2) lower maximum Sb incorporation in the InAsSb layers, which would induce blue shift of the optical response; (3) effectively thicker InAsSb layers due to segregated Sb, which would reduce the overlap of electron and hole wavefunctions and thus lead to weakened absorption; (4) smaller maximum compressive misfit strain in the InAsSb layers and reduced tensile misfit strain

in the first half of each InAs layer, which would mean reduced effect of coherency strain on band-gap engineering. All of these possible effects must be taken into account during structure design to avoid undesirable or even detrimental impact on device performance.

The same InAs/$InAs_{1-x}Sb_x$ T2SL sample selected for the study of superlattice layer thickness variation was evaluated for interface diffuseness, and a variety of microscopy techniques were adopted for this investigation. High-resolution imaging coupled with geometric phase misfit strain analysis is straightforward to implement and provides qualitative misfit strain information across the superlattice layers, thus indirectly revealing the Sb compositional profile and indicating Sb segregation. Two other techniques have been performed for quantification of Sb distribution across the superlattice layers, namely electron energy-loss spectroscopy (EELS) operated in scanning mode, and 002 dark-field (DF) imaging combined with kinematical contrast calculation. These techniques provide quantitative characterization of Sb compositional evolution along the growth direction, and thus allow further evaluation of antimony segregation.

4.3.1. Geometric Phase Misfit Strain Analysis

HAADF STEM images suitable for GPA analysis were recorded using an aberration-corrected JEOL ARM200F operated at 200 kV, with a DF detector collection semi-angle of 90 – 170 mrad: the collection inner angle was deliberately set high to minimize the inclusion of any strain-related scattering [17]. The spherical aberration coefficient was tuned to be less than 1 µm, which enabled a focused probe size of 0.08 nm with a convergence semi-angle of 21 mrad. Misfit strain analysis was carried out on as-recorded images using a dedicated GPA script based on the original GPA approach [18].

The GPA technique can be used to extract information on both in-plane and out-of-plane misfit strain across epitaxial layers. The out-of-plane misfit strain is usually defined relative to the growth direction (*z*-axis) as shown in Eq. (1) [19]:

$$\xi_{zz} = \frac{c_{\text{alloy}} - c_{\text{reference}}}{c_{\text{reference}}} \tag{4.1}$$

where *c* corresponds to the lattice parameter along the growth direction. Extended structural defects were completely absent over very large lateral distances in this particular sample (i.e., the defect density was below the detectability of plan-view TEM), and coherent interfaces were confirmed by high-resolution HAADF STEM images (see Figure 4.8 (a)). Thus, it was reasonable to assume tetragonal distortion of the lattice (see Figure 4.7) and to calculate the lattice parameter *c* using Vegard's law and Poisson's ratios [20] (or equivalently, elastic constants). The out-of-plane misfit strain in the growth direction calculated for the different layers is listed in Fig. 7 (b).

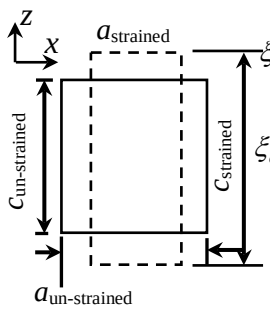

	GaSb	InAs	$InAs_{1-x}Sb_x$(x=0.34)	AlSb
a/Å	6.0959	6.0584	6.2012	6.1355
υ	0.313	0.352	0.351	0.331
ε_{zz}	0	–1.2%	+3.6%	+1.3%

Figure 4.7 Calculations of lattice parameter *c* and out-of-plane misfit strain (vs GaSb) for the case of tetragonal distortion.

HAADF STEM images (Figure 4.8 (a)), rather than HREM, were chosen for detailed misfit strain analysis here because the contrast in HAADF STEM images is relatively immune to small thickness/focus changes and more intuitively interpretable over

greater thickness ranges. Moreover, misfit strain in thicker specimen regions can be more reliably measured since strain relaxation at the specimen surface due to thinning is less severe. In this study, the sample thicknesses were typically ~ 5 – 10 times greater than the layer period. The influence of distortions in the scanning system on misfit strain analysis was accounted for by recording successive images in two orthogonal orientations. The images recorded with the scanning direction along or perpendicular to the growth direction were used to analyze either the out-of-plane or the in-plane misfit strain, respectively.

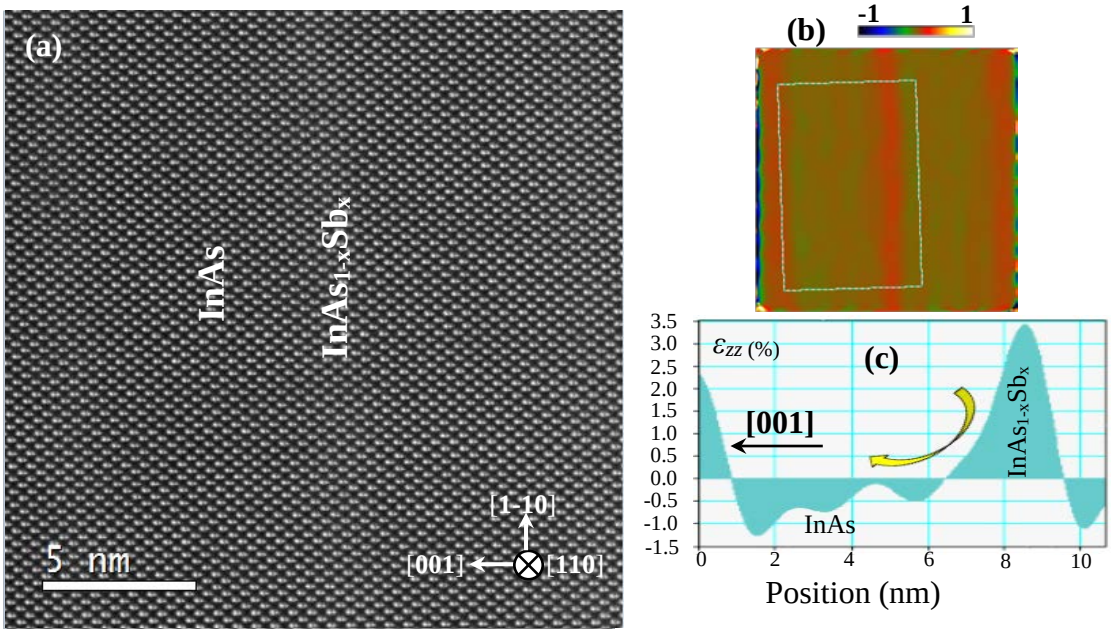

Figure 4.8 (a) Aberration-corrected HAADF image; (b) out-of-plane misfit strain map (with color legend) obtained through GPA analysis; and (c) misfit strain line profile averaged along the direction perpendicular to [001].

The GPA analysis was carried out by selecting two non-collinear 111 Bragg spots with smoothed reciprocal-space masks that provided a spatial resolution of 1 nm, and by using the InAs layers as reference since the unstrained GaSb buffer was far out of the field of view. In particular, the InAs reference region was close to the next InAsSb layer in the growth direction, thus away from any possible influence of Sb segregation across the InAs-

on-InAsSb interface, as later justified by EELS and 002 DF analysis of the segregation broadening length. The misfit strain map was then converted with respect to the unstrained GaSb. The standard deviation of the misfit strain measurements was 0.3 % judging from signal variation present in the unstrained GaSb buffer layer. The out-of-plane misfit strain in the AlSb barrier layer was also measured by precession electron diffraction (not shown here) to be 1.3 %, agreeing well with the calculation shown in Figure 4.8 (b).

The in-plane misfit strain was found to be negligible over all superlattices examined (not shown here), which agreed with the previous observations of coherent interfaces and no extended defects. A representative summary of the out-of-plane misfit strain analysis is listed in Figure 4.8. It is evident from the out-of-plane misfit strain maps in Figure 4.8 (b) that the InAs layers were under biaxial tension and the InAsSb layers were under biaxial compression, each with a misfit strain value in reasonable agreement with the calculation for the case of tetragonal distortion (Figure 4.8 (c)). The transition from tensile misfit strain in the InAs layer to compressive in the InAsSb layer occurred relatively quickly indicating sharp interfaces and effective Sb incorporation upon introduction of the Sb flux. In comparison, the transition from compressive misfit strain in the InAsSb layer to tensile in the InAs layer was gradual and extended over longer distances. The explanation for such a graded misfit strain profile compared with the InAsSb-on-InAs interface must be related to how the Sb composition evolved, which is the only factor varying across the SL structure. Thus, the graded Sb composition profile is likely to be due to segregation, which was reported previously to occur during MBE growth [9]. As a result, the intended step-like profile was altered to a significantly graded profile for the InAs-on-InAsSb interface, in addition to reduced maximum compressive misfit strain in the InAsSb layers and locally

weakened tensile misfit strain in the InAs layers. All of these factors would alter the intended band structure and cause the optical response to deviate from the target design.

It is difficult to reliably determine Sb composition or estimate Sb segregation from misfit strain measurements, mainly because: (1) at a crystal discontinuity such as an interface, the GPA algorithm averages over both sides of the interface such that the absolute value is not the true local misfit strain; (2) there is an inherent error associated with choosing the 111 Bragg diffraction spots. In addition to geometric phase associated with the true misfit strain, an non-zero phase term related to the sub-cell structure contributes as false strain, even though relatively small [21]; (3) the spatial resolution is limited, as defined by the masks applied in reciprocal space. Nevertheless, GPA misfit strain analysis is straightforward to implement, and provides useful preliminary insight into the existence of fine-scale grading of Sb compositional profile that is likely to be due to Sb segregation.

4.3.2. Convergent-Beam Electron Diffraction

The evolution of the lattice parameter along the growth direction *c* across the superlattice interfaces can be directly determined by fitting the positions of high-order Laue zone (HOLZ) lines in the experimentally recorded transmitted disks of convergent-beam electron diffraction (CBED) patterns to those in the simulated CBED transmitted disk. The Sb composition can subsequently be calculated using tetragonal distortion and Vegard's law.

To achieve misfit strain measurement with sensitivity of ($\Delta a/a$) ~ 0.1 %, accelerating voltage and thickness of region of interest need to be determined [22], by fitting experimental and simulated HOLZ lines positions in the transmitted disk, and the dynamical scattering feature within the zero-order Laue Zone disks, of the GaSb buffer

layer (assuming bulk GaSb lattice constants). Bloch wave dynamical scattering simulation were performed using JEMS [23] under the assumption of tetragonal distortion. Zone axis of <210> instead of <110> was used to enhance HOLZ visibility, avoid strong dynamical scattering [24]. Figure 4.9 shows the Bloch-wave simulation of HOLZ lines intersecting differently for $InAs_{0.66}Sb_{0.34}$, InAs and GaSb under the same accelerating voltage of 120 kV and local specimen thickness of 250 nm.

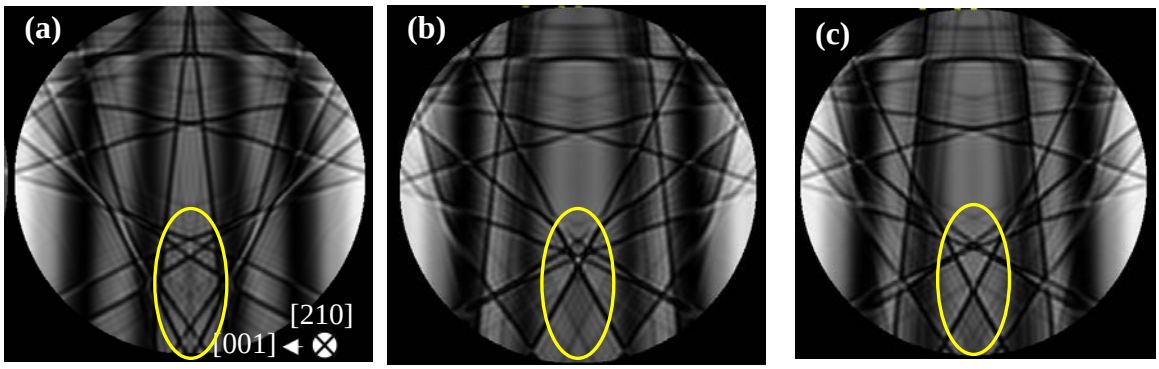

Figure 4.9 Bloch-wave simulation with 120-kV accelerating voltage and 250-nm thickness: (a) InAsSb; (b) InAs and (c) GaSb. Yellow ellipses show HOLZ lines intersect that are sensitive to voltage/lattice constant change.

Experimentally, great difficulties were encountered in the experiment. The poor visibility of HOLZ lines in the transmitted disk, at accelerating voltages of either 200 kV or 80 kV. Access to a specimen-cooling stage (low temperature enhances HOLZ scattering and minimizes phonon scattering or thermal-diffuse scattering) or energy-filtering (remove inelastically scattered electrons) would be helpful in this regard, but was not available. Besides, the application of CBED in this interface study is limited by finite probe size attainable, because the large specimen thicknesses correspond to spread of the finely-focused, highly-convergent electron probe, which is not ideal for investigation of the fine-scale interfacial compositional profile, as revealed previously by GPA.

4.3.3. Precession Electron Diffraction

TEM is not only capable of providing misfit strain, or lattice parameter information through dynamical scattering process (e.g. HOLZ lines in CBED), but also by using nearly kinematical scattering with suitable experimental conditions. Precession electron diffraction (PED) [25] involves a fine parallel electron probe with largely tilt which is precessed about a conical surface centered at the TEM optical axis. The diffraction patterns obtained largely lack forbidden reflections and multiple scattering, and are regarded as being much closer to kinematical scattering, allowing reliable analysis of misfit strain and lattice parameters perpendicular to the incident beam direction from direct geometric measurements of the diffraction patterns.

Precession electron diffraction patterns were recorded on the JEOL ARM200F operated in regular TEM mode, with the electron beam controlled by the NanoMEGAS DigiSTAR system. An example of the PED pattern and misfit strain measurement are shown in Figure 4.10.

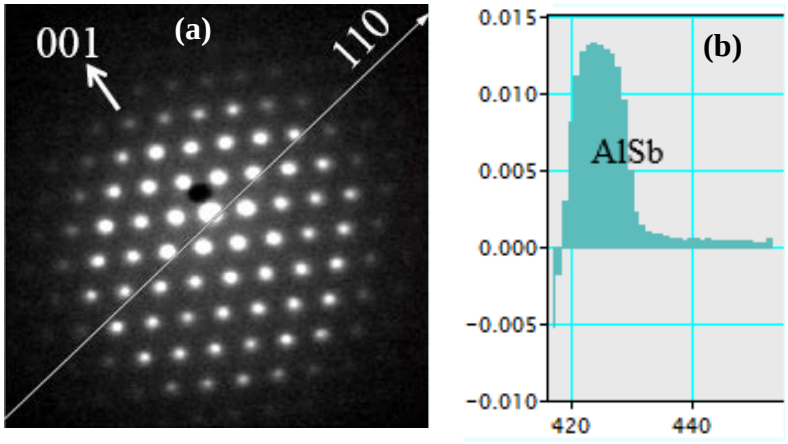

Figure 4.10 (a) Example of PED pattern recorded in AlSb region; (b) Calculated ε_{zz} for the bottom AlSb layer.

PED misfit strain analysis provides high precision (+/– 0.05% judging from GaSb buffer layer), but the technique is limited by spatial resolution (> 1.5nm for the JEOL ARM200F at ASU). Misfit strain calculation can be performed directly using diffraction spots since the patterns were recorded using precessed illumination with large tilt under close to kinematic scattering conditions. The ε_{zz} misfit strain of the bottom 10-nm-thick AlSb barrier layer was measured to be 1.3 %, agreeing with previous theoretical misfit strain calculations based on tetragonal distortion. This result indicates that strain relaxation is not significant if measurement is done in thick regions of the TEM sample.

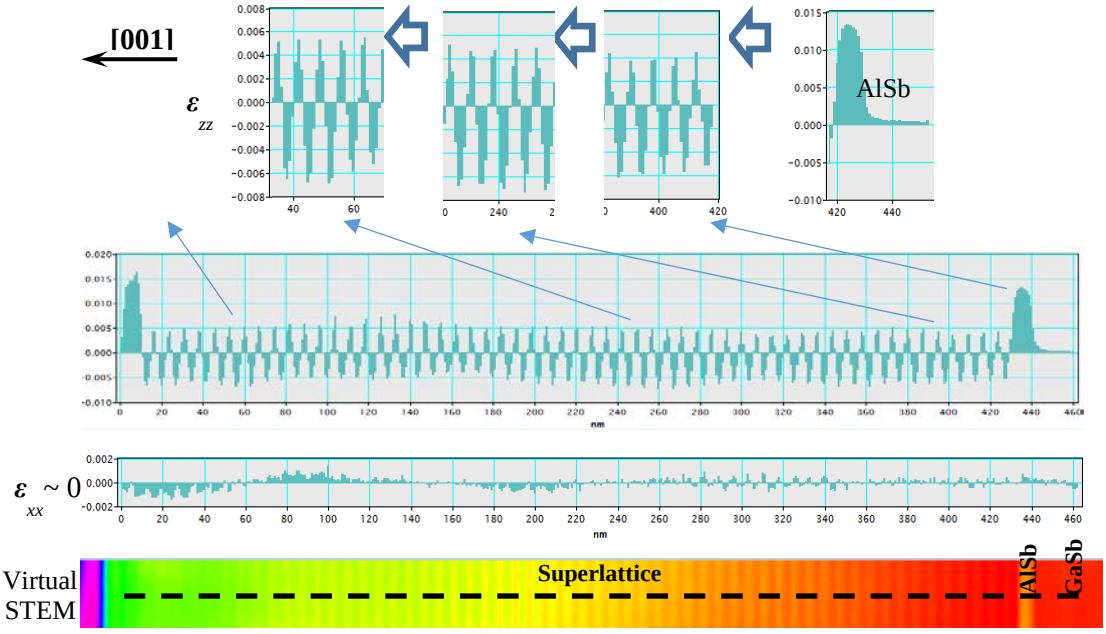

Figure 4.11 Representative misfit strain analysis of the whole superlattice stack using precession electron diffraction patterns.

However, the electron probe is too broad to resolve local misfit strain variations within and across the superlattice layers. Figure 4.11 shows the representative analysis of PED patterns recorded throughout the whole superlattice stack. The in-plane misfit strain is close to zero as expected for a coherently strained structure; the out-of-plane misfit strain

fluctuates from one superlattice layer to another, but the analysis fails to provide meaning out-of-plane misfit strain data. The misfit strain value stays far from the theoretical calculation, and there is a lack of fine-scale misfit strain variations as previously revealed by GPA analysis. These factors are mainly due to the finite electron beam size.

4.3.4. Electron Energy-Loss Spectroscopy in Scanning Mode

Unlike the methods discussed above, the EELS technique not only provides direct quantification of the Sb composition, and thus its evolution, but also allows very high spatial resolution since it utilizes the finely focused electron beam in STEM mode.

EELS spectrum images were acquired using the JEOL ARM 200F, which was equipped with a Gatan Enfinium EELS spectrometer capable of DualEELS acquisition. The instrument was operated at the accelerating voltage of 80 kV, for the purpose of reducing any electron-beam-induced specimen damage and also enhancing the energy-loss signal by increasing the inelastic scattering cross-sections [26]. The beam convergence semi-angle of 30 mrad was defined by a 40-μm condenser aperture, and the electron probe size was ~ 0.2 nm. The EELS collection semi-angle of 60 mrad was defined using a 5-mm entrance aperture. A rough calculation of the most-probable scattering semi-angles using $\theta_E = \Delta E / 2E_0$ (where ΔE is energy loss, and E_0 is the accelerating voltage) yielded 2.8 mrad for the In $M_{4,5}$ edge (edge onset at 443 eV) and 3.3 mrad for the Sb $M_{4,5}$ edge (edge onset at 528 eV) for this study. The difference between the EELS collection semi-angle and the incident-beam convergence semi-angle is 8 - 10 times larger than the most-probable scattering angle so that a substantial fraction of the energy-loss signals of interest should have been collected. Moreover, the microscope-specimen geometry was kept fixed during

acquisition of all EELS spectra so that estimates of (changes in) Sb concentration vs. position should be reliable.

An energy dispersion of 0.25 eV/channel and a total of 2048 channels provided the total collected energy range of 512 eV. This particular dispersion setting was chosen to capture only the majority signals of the In and Sb *M* edges, which are close to edge onset and relatively strong, so that these primary and less noisy portions of the spectra are employed for quantitative analysis. Zero-loss and core-loss spectra of interest were recorded simultaneously, where the zero-loss spectra were utilized to screen for thin areas of interest and to avoid excessive plural scattering. Spectrum images were acquired with a scanning step size of 0.15 nm and a pixel time of 0.02 s. Drift correction was essential (even though the TEM specimen was loaded beforehand to stabilize overnight) to counteract unavoidable slight drift introduced by significant changes of the goniometer setting when locating suitable regions of interest, as well as some ambient interference, because the Sb segregation, which was the feature of interest, occurred over a very fine scale (as revealed by prior GPA analysis). Acquisition of a single EELS spectrum image capturing three superlattice periods typically took more than 10 min.

The major challenge for EELS investigations of these InAs/$InAs_{1-x}Sb_x$ T2SL samples lies in the fact that the core-loss edges of interest, namely Sb and In $M_{4,5}$ edges (edge onsets at 528 eV and 443 eV, respectively), are two closely-positioned delayed edges with significant overlap. As a result, regular EELS quantification routines using background subtraction and peak integrals would likely fail due to unreliable extraction of individual signals. In this study, MLLS fitting [27] was implemented to achieve reliable separation of the Sb $M_{4,5}$ edge from the In $M_{4,5}$ edge. The Sb and In reference spectra were

taken from the AlSb barrier layer and from the InAs capping layer, respectively. Thus, the reference and target spectra were acquired from the same TEM specimen with identical acquisition parameters under similar chemical environment (same valence state). Zero-loss spectra were also recorded to calculate the relative sample thickness (in units of λ, the mean free path for inelastic scattering) in order to select suitably thin regions of the TEM specimens, so that both two-dimensional spectrum images and reference spectra could be acquired from relatively thin regions with similar thicknesses to make allowance for any plural scattering [27].

A representative STEM-EELS analysis is summarized in Figure 4.12. The EELS spectrum image was recorded from the region indicated by the solid blue rectangle in Figure 4.12 (a), and a closely adjacent region, indicated by the dashed yellow square, was used for drift correction. The core-loss spectrum image was acquired with both In and Sb $M_{4,5}$ edges included to enable MLLS fitting. The relative thickness map shown in Figure 4.12 (d) indicated that the thickness in this region was relatively uniform and considerably less than one inelastic mean free path (average thickness of 0.7 λ), similar to the thickness of the regions where the reference spectra were acquired (not shown here). Under this well-controlled acquisition condition, the ratio of MLLS fitting coefficients for the corresponding Sb/In 2D map in Figure 4.12 (b) and the extracted averaged line profile in Figure 4.12 (c) (averaged over two pixels) give the projected areal density of Sb compared with In in the scanned region. Thus, since the In content is presumed to be constant throughout growth of the InAs/$InAs_{1-x}Sb_x$ SL stack, the Sb composition can be extracted. Note that the Sb composition is the average for the examined region projected along the electron beam direction.

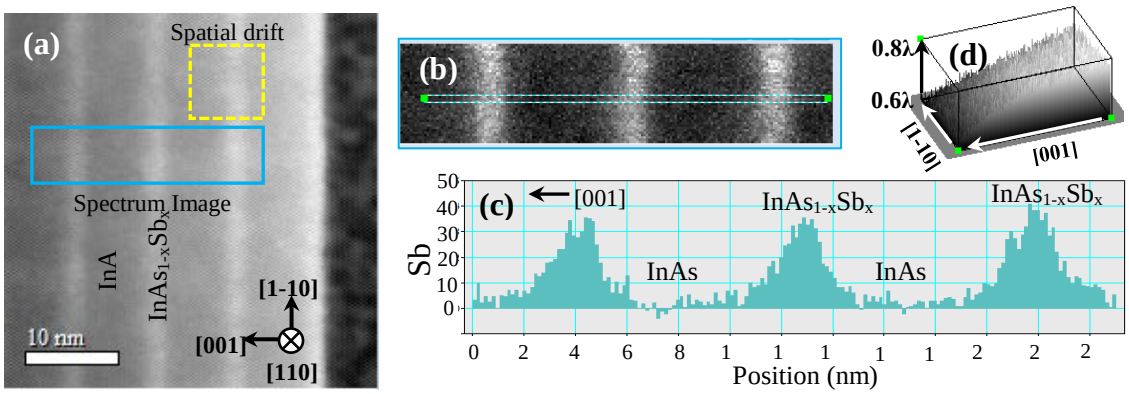

Figure 4.12 (a) Survey image for spectrum image acquisition, defining region of interest with solid blue rectangle, and area for spatial drift correction with dashed yellow square; (b) ratio map of MLLS fitting coefficients of Sb versus In; (c) Sb composition profile extracted from dashed blue rectangle in (b) averaged over two pixels; (d) relative thickness map of region of interest calculated from zero-loss spectrum image.

Closer examination of Figure 4.12 (c), which is the averaged projected line profile of Sb composition, confirmed the asymmetric interfaces in the superlattices, as previously indicated by GPA analysis. The InAsSb-on-InAs interface was relatively sharp, while the graded InAs-on-InAsSb interface demonstrated a typical segregational feature of an exponential-like tail with Sb atoms migrating from the InAsSb layer into the following InAs layer. The maximum Sb composition in the InAsSb layers here is about 35 %.

4.3.5. 002 Dark-Field Imaging

The 002 DF investigations were performed by Dr. E. Luna in Paul-Drude Institute, Berlin using a JEOL JEM 3010 transmission electron microscope operated at 300 kV using an objective aperture size of ~ 5 µm. To set up the correct g_{002} diffraction condition, the amount of tilt of both the incident electron beam and the TEM specimen were carefully chosen. In particular, the specimen was tilted by 8 – 10 º away from the <110> zone axis towards the [100] pole, while keeping the interface edge-on. The 002 Bragg beam used to

form the DF image was then selected using an objective aperture. The size of the aperture defined the spatial resolution, which was ~ 0.5 nm in this case.

002 DF imaging is a non-standard TEM imaging technique that uses a chemically-sensitive reflection, which is the 002 reflection in the case of zincblende III-V semiconductor compounds, to form DF images. The contrast in this "structure-factor imaging mode" mainly arises from the difference in the atomic-scattering factors between the group-III and group-V elements [28, 29]. In III–V alloys, the diffracted intensity for the 002 reflection is proportional to the square of the structure factor F_{002}, which in turn depends on the difference in the atomic-scattering factors of the alloy components (f_{III} and f_V for the group-III and group-V elements, respectively), thus $I_{002} \sim F^2{}_{002} \sim |f_{III} - f_V|^2$. Hence, when the 002 imaging condition is properly set up for a specimen region of interest with thickness well below the extinction distance for (002) reflections, compositional information can be directly extracted following the procedure of Bithell and Stobbs [28], which is based on analysis of the DF image contrast using kinematical calculations.

A typical 002 DF image of the superlattices is shown in Figure 4.13 (a), while Figure 4.13 (b) shows the averaged Sb composition profile extracted from the region marked by the white dashed rectangle (averaged over 30 pixels, which corresponds to about 4 nm). The averaged intensity line profile was initially calibrated using a characteristic dark-line feature (minimum-intensity line) at the AlSb/InAsSb interface [30]. Quantitative chemical determination was then carried out by analyzing the (002) diffracted intensity assuming the kinematical scattering approximation (with atomic-scattering factors adapted from Doyle and Turner [31]). The influence of electron redistribution due to the bonding of atoms, local structural distortions and thin-foil surface relaxation were not considered.

Note that the layer contrast in the 002 DF images is not the same as for the HAADF images used in GPA analysis, i.e., the InAsSb layers appear darker than the InAs layers because of different contrast mechanisms for the two techniques. The maximum Sb content of about 35 % estimated by 002 DF analysis is in remarkable agreement with the value obtained from EELS. Furthermore, the presence of asymmetric Sb profiles on either side of the InAsSb layers is confirmed, which is in agreement with the information obtained previously by GPA and EELS analysis. The 002 DF imaging results corroborate that the InAsSb-on-InAs interface is relatively sharp while the InAs-on-InAsSb interface is graded, and resembles a typical segregation profile with a decreasing exponential-like tail penetrating into the next InAs layer.

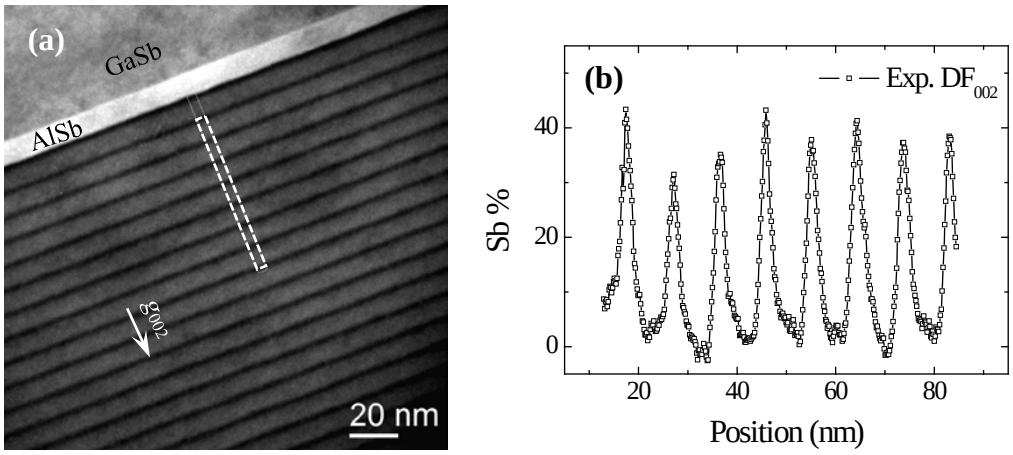

Figure 4.13 (a) Representative chemically-sensitive 002 DF image, with white dashed rectangle defining region of interest; (b) Experimental Sb composition profile obtained through analysis of diffracted intensity.

The main challenge associated with implementation of 002 DF imaging is to tilt the specimen with the 002 beam at or close to the Bragg condition while imaging the interface closely edge-on. A small tilting offset of the interface from the exact edge-on condition would broaden the projected interface by 0.5 – 1 monolayer (ML) for specimen thicknesses

of 50 – 100 nm. Such broadening is negligible provided that careful choices of specimen/beam tilting and specimen thickness are made, and is much smaller than the interface width measured here, as discussed in the next section. For other MBE-grown III-V heterostructures, the typical interface width (10% – 90% criterion) ranges between 4.4 and 7.5 ML [32]. In addition, although this imaging method is aperture-limited, it has been shown elsewhere that detailed analysis of the *shape* of the composition profiles, supported by structural modeling, allows quantification of the chemical interface, and variations in interface widths and layer thicknesses as small as 0.1 ML can be measured [33, 34].

4.3.6. Evaluation of Antimony Segregation

002 DF imaging and STEM EELS provided compositional evolution of Sb across the superlattices, and directly revealed, at the same time, the graded/broadened InAs-on-InAsSb interface with an exponential-like descending tail characteristic of surface segregation. Thus, the Sb composition profiles across this interface obtained from 002 DF and EELS measurements were evaluated using Muraki's phenomenological segregation model (Eq. (2)), which initially assumes a step-like interface, as summarized (for layer centered at the lower interface along the growth direction) by [35]:

$$x_n = x_0(1-R^z), \text{ for } 0 \le z \le N;\ x_n = x_0(1-R^N) \bullet R^{z-N}, \text{ for } z \ge N. \quad (4.2)$$

The segregation probability R defines the fraction of Sb atoms in the topmost layer that segregate into the next layer, N is the thickness of the InAsSb layer, and x_0 is the Sb composition. The analysis was performed by evaluating the profile fitting in the vicinity of the InAs-on-InAsSb interface by adjusting the parameters R, N and x_0. It was found that regardless of the technique used to obtain the Sb composition profiles or their particular location within the 58.5-period stack, the decay at the graded InAs-on-InAsSb interface

was well reproduced by the segregation model with the same parameters. Figure 4.14 (a) and (c) list representative experimental Sb composition profiles and corresponding segregation fitting curves for the 002 DF imaging and STEM EELS study.

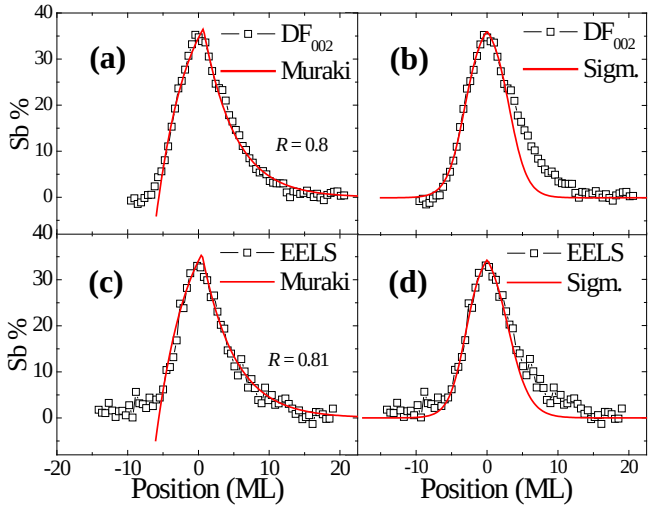

Figure 4.14 Experimental Sb composition profiles and corresponding segregation and sigmoidal fitting curves obtained from: (a) & (b) 002 DF imaging; and (c) & (d) STEM EELS.

The segregation probability *R* obtained from multiple fittings of data with both techniques agree well within experimental error and yield 0.81 +/– 0.01, which represents strong segregation when compared to values reported in the literature [36, 37]. In particular, R = 0.81 indicates that 81 % of the Sb atoms in the topmost layer on average have segregated into the next monolayer during growth. The interface width due to segregation broadening, defined as the length over which the Sb composition changes from 90 % to 10 % of the plateau value, can also be obtained. The interface width was found to be about 10 ML, which corresponds to a broadened width of about 3 nm (using a lattice constant of 0.62 nm for $InAs_{0.66}Sb_{0.34}$ following Vegard's law). This unexpectedly strong segregation significantly altered the composition profile from the ideal, step-like interface usually

assumed during T2SL structure design to one that is rather broadened, thus impacting the consequential evolution of the misfit strain across the InAs-on-InAsSb interfaces and beyond.

The InAsSb-on-InAs interface, although relatively abrupt, also deviated from the ideal, step-like shape assumed in the segregation model, as evident from the slight discrepancy between the Sb composition profiles and the segregation fitting at this interface. This is unlikely to be due to Sb segregation. This non-ideal interface is due to an intrinsic minimum interface width that is dictated by the molecule-surface interaction potential during growth, which can be approximated with a set of sigmoidal functions, as represented by Equation (3) [32-34]. For layers centered at $z = 0$, the sigmoidal expressions are:

$$x = \frac{x_0^{(l)}}{1 + e^{\frac{-(z+\frac{N}{2})}{L_{lower}}}}, \text{for } z < 0; \; x = x_0^{(u)} - \frac{x_0^{(u)}}{1 + e^{\frac{-(z-\frac{N}{2})}{L_{upper}}}}, \text{for } z > 0. \tag{4.3}$$

where $x_0^{(l)}$ and L_{lower}, $x_0^{(u)}$ and L_{upper} denote the composition and the intrinsic interface width at the lower (l) and upper (u) interfaces, respectively, and N is the layer thickness. This sigmoidal-type interface exists naturally at both interfaces in this T2SL system. However, the segregation effect across the InAs-on-InAsSb interface is so strong that it dominates over the intrinsic sigmoidal profile (Figure 4.14 (b) and (d)), and the Sb composition evolution can be reasonably reproduced using only the segregation model (Figure 4.14 (a) and (c)). Hence, the Sb composition profile across a three-layer structure of InAs/InAsSb/InAs was better described using a piecewise function, using the sigmoidal model for the InAsSb-on-InAs interface, and Muraki's segregation model for the InAs-on-

InAsSb interface. The connecting point of the two models is marked with an arrow, as indicated in Figure 4.15 for profiles obtained from 002 DF imaging and EELS analysis. Experimental Sb composition profiles obtained from these two independent microscopy techniques were very well reproduced using the combined models with the same fitting parameters. In addition to the segregation probability of 81 %, an intrinsic interface width of 1.2 ML was obtained for the InAsSb-on-InAs interfaces, which is relatively small compared to the broad InAs-on-InAsSb interface, confirming segregation as the dominant mechanism.

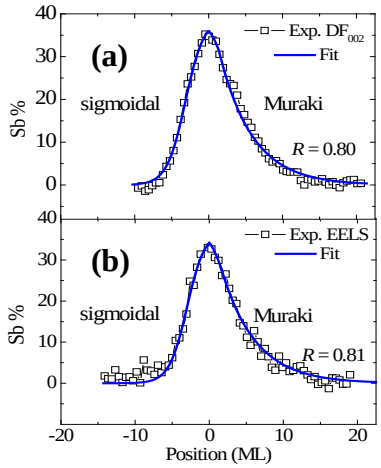

Figure 4.15 Experimental Sb composition profiles and corresponding fitting curves using combination of sigmoidal function for InAsSb-on-InAs interface and Muraki's segregation model for InAs-on-InAsSb interface, as obtained from: (a) 002 DF imaging; and (b) STEM EELS. Arrows indicate connection points of the fitting curves.

Thus, quantitative evaluation of the Sb composition profiles that has been obtained from these two independent microscopy techniques, with the aid of segregation and sigmoidal models, demonstrates remarkable agreement: both yield Sb segregation probability of 81 % and a segregation broadening length of about 3 nm. This significantly modified composition profile which in turn alters the effective superlattice layer thickness

and period, and related strain engineering, will induce significant deviations in the energy-band structure and the optoelectronic response.

4.4. Effect of Bismuth Surfactant

Recent progress has been made in the design, growth and characterization of Ga-free InAs/$InAs_{1-x}Sb_x$ T2SL with very high structural quality, and the SL interface abruptness seems to play a significant role in affecting the emission properties [9-12]. Growth front coverage with surfactants of at most a few monolayer thickness has been used in MBE to help improve the surface/interface morphology and material properties. For example, Sb was used as a non-reactive surfactant for the growth of AlGaAs, and the surface morphology was improved at all growth temperatures investigated [38]. It continues to be of interest to investigate the effectiveness of surfactants on interface roughness.

A T2SL sample was also grown using a Bi surfactant. These superlattices consisted of 56.5 periods of 8-nm $InAs_{1-x}Sb_x$ (x = 19 %) and 9-nm InAs layers, as indicated in Figure 4.16 (b), and was grown at a substrate temperature of 430 °C. The Bi flux (Bi/In flux ratio = 3 %) was switched on during growth of the last 40 nm of the GaSb buffer layer, and was kept on throughout the growth of the entire superlattice structure as well as the 100-nm GaSb capping layer. Additional growth details are provided elsewhere [39].

The particular sample studied was grown with a Bi/In flux ratio of 3 %, which was the highest of the series. A bright-field (BF) TEM image of a superlattice region close to the top of the superlattices is shown in Figure 4.16 (a). The averaged intensity line profile of the BF image is extracted (Figure 4.16 (b)) in order to study the interface abruptness and thus the possible effect of Bi surfactant [40]. The valleys visible in Figure 4.16 (b)

correspond to InAs layers while the peaks correspond to the InAsSb layers. The gradual intensity drop at the interface of InAs-on-InAsSb compared to the interface of InAsSb-on-InAs indicated interfacial broadening, as observed previously for samples grown without any surfactant [7]. Thus, it appears that use of the Bi surfactant during growth did not significantly improve the asymmetrical interfacial abruptness.

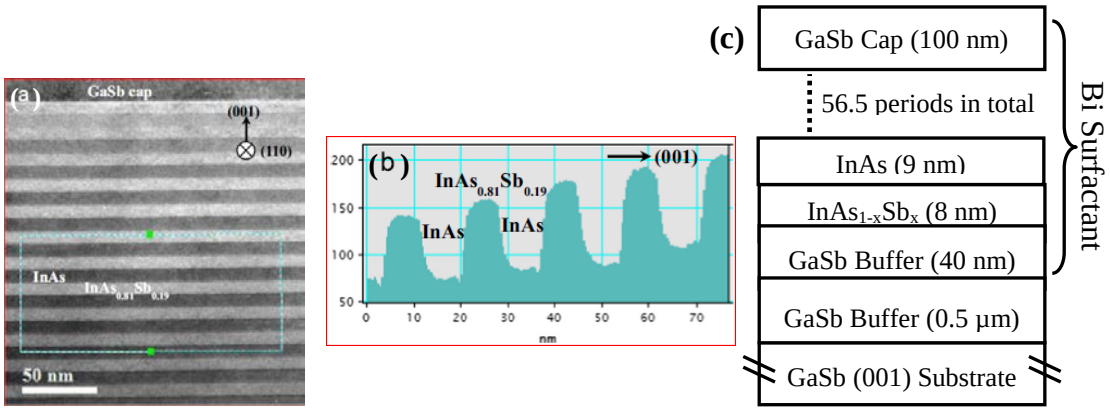

Figure 4.16 (a) Bright-field TEM image of the superlattices close to the top of the epilayer; (b) averaged intensity line profile extracted from the blue rectangular region in (a); (c) schematic of the Bi-mediated T2SL structure.

4.4.1. Future Work: Quantitative Evaluation of Bi Surfactant Effect

The results presented here indicate that antimony segregates at the interface of InAs-on-InAsSb for superlattices grown without special interfacial treatment. The application of a suitable surfactant during growth has the potential to improve the interface abruptness, and more research effort should be devoted to optimize the growth of Ga-free T2SL with Bi surfactant. Thus, it is of interest to characterize quantitatively the Sb compositional profile across the superlattice grown with and without Bi surfactant, in similar fashion to the work presented in Section 4.3, and then evaluate in detail the impact of the surfactant on the interface abruptness.

References

[1] J. Lu, E. Luna, T. Aoki, E. H. Steenbergen, Y.-H. Zhang, and D. J. Smith, J. Appl. Phys. **119**, 095702 (2016).

[2] P. Martyniuk, J. Antoszewski, M. Martyniuk, L. Faraone,, A. Rogalski, Appl. Phys. Rev. **1**, 041102 (2014).

[3] D. R. Rhiger, J. Electron. Mater. **40**, 1815 (2011).

[4] S. P. Svensson, D. Donetsky, D. Wang, H. Hier, F. J. Crowne and G. Belenky, J. Cryst. Growth **334**, 103 (2011).

[5] E. H. Steenbergen, B. C. Connelly, G. D. Metcalfe, H. Shen, M. Wraback, D. Lubyshev, Y. Qiu, J. M. Fastenau, A. W. K. Liu, S. Elhamri, O. O. Cellek and Y.-H. Zhang, Appl. Phys. Lett. **99**, 251110 (2011).

[6] B. B. V. Olson, Appl. Phys. Lett. **101**, 092109 (2012).

[7] L. Ouyang, E. H. Steenbergen, Y.-H. Zhang, K. Nunna, D. L. Huffaker and D. J. Smith, J. Vac. Sci. Technol. B **30**, 02B106 (2012).

[8] X.-M. Shen, H. Li, S. Liu, D. J. Smith and Y.-H. Zhang, J. Cryst. Growth **381**, 1 (2013).

[9] A. Y. Lew, E. T. Yu and Y.-H. Zhang, J. Vac. Sci. Technol. B **14**, 2940 (1996).

[10] K. Mahalingam, E. H. Steenbergen, G. J. Brown and Y.-H. Zhang, Appl. Phys. Lett. **103**, 061908 (2013).

[11] J. Lu, P. T. Webster, S. Liu, Y.-H Zhang, S. R. Johnson and D. J. Smith, J. Cryst. Growth **425**, 250 (2015).

[12] M. R. Wood, K. Kanedy, F. Lopez, M. Weimer, J. F. Klem, S. D. Hawkins, E. A. Shaner and J. K. Kim, J. Cryst. Growth **425**, 110 (2015).

[13] E. H. Steenbergen, Y.-H. Zhang, unpublished result.

[14] Z.-Y. Lin, S. Liu, E. H. Steenbergen, Y.-H. Zhang, Appl. Phys. Lett. **107**, 201107 (2015).

[15] R. Kilaas, J. Microscopy **190**, 45 (1998).

[16] D. O. Klenov, S. D. Findlay, L. J. Allen and S. Stemmer, Phys. Rev. B **76**, 014111 (2007).

[17] Z.-H. Yu, D. A. Muller and J. Silcox, J. Appl. Phys. **95**, 3362 (2004).

[18] M. J. Hÿtch, E. Snoeck and R. Kilaas, Ultramicroscopy **74**, 131 (1998).

[19] N. J. Ekins-Daukes, K. Kawaguchi, and J. Zhang, Cryst. Growth Des. **2**, 287 (2002).

[20] S. Adachi, in Handbook on Physical Properties of Semiconductors, (Springer, 2004), Vol. 2, p. 453.

[21] J. J. P. Peters, R. Beanland, M. Alexe, J. W. Cockburn, D. G. Revin, S. Y. Zhang and A. M. Sanchez, Ultramicroscopy **157**, 91 (2015).

[22] J. M. Zuo, Ultramicroscopy **41**, 211 (1992).

[23] P. Stadelmann, Ultramicroscopy **21**, 131 (1987).

[24] J. N. Stirman, M. Takeguchi, M. R. McCartney and D. J. Smith, Appl. Phys. Lett. **84**, 490 (2004).

[25] R. Vincent and P, Midgley, Ultramicroscopy **53**, 271 (1994).

[26] R. F. Egerton, in Electron Energy-Loss Spectroscopy in the Electron Microscope, (Springer, 2011), Chap. 3, p. 142.

[27] R. F. Egerton, ibid., Chap. 4, p. 287.

[28] E. G. Bithell and W. M. Stobbs, Philos. Mag. A **60**, 39 (1989).

[29] D. B. Williams and C. B. Carter, Transmission Electron Microscoy: A Textbook for Materials Science, 2nd edn. (Springer, US, 2009), p. 261.

[30] G. Patriarche, L. Largeau, J. C. Harmand and D. Gollub, Appl. Phys. Lett. **84**, 203 (2004).

[31] P. A. Doyle and P. S. Turner, Acta Cryst. A **24**, 390 (1968).

[32] E. Luna, A. Guzman, A. Trampert and G. Alvarez, Phys. Rev. Lett. **109**, 126101 (2012).

[33] E. Luna, B. Satpati, J. B. Rodriguez, A. N. Baranov, E. Tournié, and A. Trampert, Appl. Phys. Lett. **96**, 021904 (2010).

[34] E. Luna, A. M. Beltran, A. M. Sanchez, and S. I. Molina, Appl. Phys. Lett. **101**, 011601 (2012).

[35] K. Muraki, S. Fukatsu, Y. Shiraki and R. Ito, Appl. Phys. Lett. **61**, 557 (1992).

[36] J. Steinshnider, J. Harper, M. Weimer, C.-H. Lin, S.-S. Pei and D. H. Chow, Phys. Rev. Lett. **85**, 4562 (2000).

[37] A. Semenov, O. G. Lyublinskaya, V. A. Solovev, B. Y. Meltser and S. V. Ivanov, J. Cryst. Growth **301**, 58 (2007).

[38] S.R. Johnson, Yu.G. Sadofyev, D. Ding, Y. Cao, S. A. Chaparro, K. Franzreb, Y.-H. Zhang, J. Vac. Sci. Technol. B **22**, 1436 (2004).

[39] P. T. Webster, N. A. Riordan, C. Gogineni, S. Liu, J. Lu, X.-H. Zhao, D. J. Smith, Y.-H. Zhang and S. R. Johnson, J. Vac. Sci. Technol. B **32**, 02C120 (2014).

[40] S. Francoeur, M.-J. Seong, A. Mascarenhas, S. Tixier, M. Adamcyk and T. Tiedje, Appl. Phys. Lett. **82**, 3874 (2003).

CHAPTER 5

CdTe-BASED STRUCTURES GROWN ON InSb

The research described in this chapter was carried out in collaboration with the groups of Prof. Yong-Hang Zhang at Arizona State University, and Dr. Rafal E. Dunin-Borkowski at Ernst-Ruska Center in Julich, Germany. My role involved structural characterization of the CdTe-based structures grown on InSb substrates using transmission electron microscopy. Major results from this study have been published [1].

5.1. Introduction

The growth of epitaxial thin films of CdTe by molecular beam epitaxy was originally explored for potential applications in optoelectronics devices and as part of hybrid substrates for the growth of $Hg_{1-x}Cd_xTe$ alloys on economic substrates [2, 3]. InSb appeared to be a promising substrate for CdTe growth because of its small lattice mismatch and similar coefficient of thermal expansion with CdTe. However, the growth of CdTe on InSb historically suffered from a problematic interface that was attributed to compound(s) with different lattice spacings that could easily induce structural deterioration near the interface and well beyond [4]. Efforts have been devoted to eliminating the formation of interfacial compound(s) through proper surface preparation of substrates, choice of growth temperature [5], and introduction of an intermediate InSb buffer layer in a dual-chamber molecular beam epitaxy system [6, 7].

The atomistic nature of the CdTe/InSb interface has been an intriguing question for researchers from different fields. Since CdTe (II-VI compound) and InSb (III-V compound) are heterovalent compound semiconductors, the possible interfacial bonding could be: Cd-Sb, In-Te, or a mixture of both. An interfacial layer of In-Te compound has been suggested

from soft X-ray photoelectron spectroscopy [8] and Raman spectroscopy [9]. However, the structure of the CdTe/InSb interface has remained an open question for electron microscopists even though theoretically transmission electron microscopy has the capability to resolve atomistic structures with high enough spatial resolution. Besides investigation of the interface structure, TEM provides diffraction contrast imaging that can directly reveal the existence of extended defects such as dislocations, stacking faults, in cross-sectional or plan-view geometry. This feature is beneficial because the characterization of defective structures through evaluation of full-width at half-maximum of X-ray diffraction peaks is not always straightforward because some defects do not contribute to the width of the diffraction peak [10].

In this chapter, techniques based on diffraction contrast and Z-contrast imaging were utilized to evaluate the structural quality of CdTe epi-layers grown at different growth temperatures, and the CdTe/InSb interface grown at optimal temperature. Misfit strain at the CdTe/InSb interface was evaluated using geometric phase analysis [11].

5.2. Experimental Details

The specimens under investigation were grown in a dual-chamber VG V80H MBE system with separate III-V and II-VI chambers connected by an ultrahigh-vacuum (UHV) transfer chamber. A schematic of the as-grown structures is shown in Figure 5.1.

First, InSb buffer layers of 500-nm thickness were grown on InSb (001) substrates in the III-V chamber. Monitoring *in situ* using reflection-high-energy electron diffraction (RHEED) confirmed that the InSb surface oxide had been completely removed and that the InSb buffer layers had excellent crystallinity. The quality of the InSb buffer layers in all cases was later confirmed in the XTEM images. The wafers were then transferred to the II-

VI chamber under ultrahigh vacuum to receive Cd flux treatment prior to CdTe growth to suppress the formation of any kind of interfacial III-VI compound. The Cd/Te flux ratio during growth was kept fixed at 1.5 : 1 after an initial two-minute period with a Cd/Te ratio of 3.5 : 1 (Cd overpressure should serve to suppress the formation of In_2Te_3 compound during the nucleation of CdTe growth [4]). RHEED was used throughout to monitor the II-VI growth [7]. As the CdTe growth was initiated, the RHEED pattern invariably turned hazy during transition from the InSb to the CdTe pattern, At low substrate temperature (235 °C), the transition to clear 2×1 and c(2×2) patterns, which were used to confirm the Cd-rich condition, occurred quite rapidly compared with growths done at higher temperature. After growth of the 500-nm-thick CdTe buffer layer, the CdTe/$Mg_xCd_{1-x}Te$ double heterostructure was grown, with the 1-μm-thick CdTe film sandwiched between two 30-nm-thick $Mg_{1-x}Cd_xTe$ barrier layers with nominal Mg composition of 24 %. The growth temperature was systematically varied (235 °C, 265 °C and 295 °C) while all other growth conditions were kept fixed.

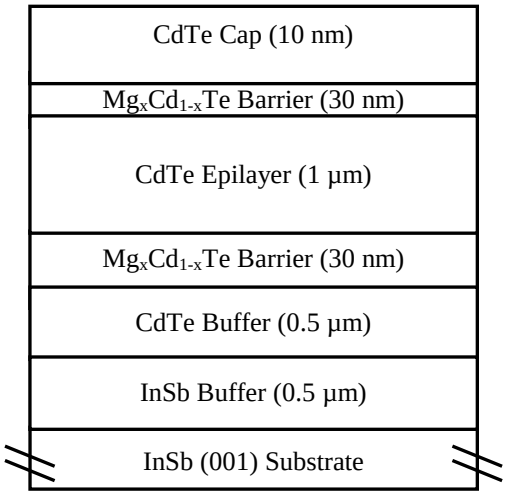

Figure 5.1 Schematic of the CdTe/MgCdTe double heterostructures grown on InSb.

Because of the known sensitivity of CdTe to argon-ion-milling [12, 13], precautions had to be taken to ensure that the microstructure of CdTe epilayers observed via TEM was representative of the as-grown structure. Hence, argon-ion-milling was performed using a liquid-nitrogen-cooled specimen holder [12, 14]. Moreover, adequate thickness of the thinned film should be maintained prior to final milling to eliminate plastic deformation induced during post-growth mechanical polishing [15]. Most samples observed here were prepared for TEM observation along <110>-type projections using traditional mechanical polishing and dimple grinding, followed by argon-ion-milling (maximum beam energy 2.2 keV) with liquid-nitrogen cooling to reduce ion-beam damage. One sample was prepared using low-voltage focused-ion-beam milling followed by ion-beam cleaning at 500 eV using a Fischione NanoMill. Electron microscopy was performed using a JEOL JEM-4000EX high resolution electron microscope with an accelerating voltage of 400 kV and structural resolution of 1.7 Å, and an aberration-corrected FEI-Titan 80-200 (scanning) transmission electron microscope (STEM) with sub-Å resolution remotely operated at 200 kV acceleration voltage.

Preliminary conventional and aberration-corrected TEM imaging were used to characterize the structural quality of epitaxial CdTe/$Mg_xCd_{1-x}Te$ (nominally x = 0.24) double heterostructures grown on (001) InSb substrates with intermediate InSb and CdTe buffer layers; this particular structure was designed for study of the photoluminescence of the CdTe bulk layer. The misfit strain distribution across the CdTe/InSb interface has also been investigated using the technique of geometric phase analysis [11], as an initial step to explore the interface structure. Detailed study of the CdTe/InSb interface (the interface of InSb/CdTe is not available in this growth campaign) would push forward the understanding

and control of such interfaces, and possibly open up new avenues for design of artificial structures such as quantum wells and superlattices, where interfaces dominate the electronic and optical behavior.

5.3. Impact of Growth Temperature

With proper substrate treatment and effective Cd overpressure, the growth temperature was found to have a major impact on the structural quality of the epi-layers. At non-optimum temperature, complicated networks of extended defects were formed, and interaction among the defects made it difficult to study individual dislocations and stacking faults. Presented here is an overview/survey of the structures imaged by BF XTEM, which reveals most of the extended defects even though the contrast is not as strong as that in the dark-field images.

As shown by the bright-field (BF) XTEM image in Figure 5.2 (a), many dislocations and threading defects were present in the lower region of the film grown at 235 °C, both in the CdTe buffer and also in the CdTe/$Mg_xCd_{1-x}Te$ double heterostructure regions. Most defects seemed to originate at or near the CdTe/InSb buffer interface, but there was no evidence for any Te precipitates, and the defect density dropped off considerably as the growth continued. Figure 5.2 (b) is a representative image showing the upper part of the heterostructure, and much less defects are visible in this region. Defect densities were estimated from the cross-sectional electron micrographs to range from > 10^9 cm^{-2} near the CdTe/InSb interface to ~ mid-10^7 cm^{-2} near the top surface. Ion-milling damage in CdTe had been identified previously as consisting primarily of planar-faulted dislocation loops with a density that is independent of sample thickness along the electron

beam direction [12]. This is clearly not the situation here since the defect density steadily decreases moving away from the substrate.

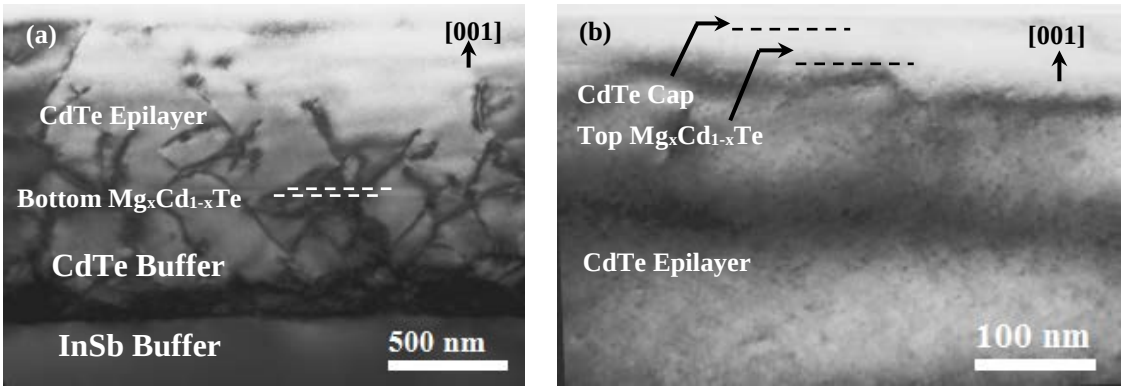

Figure 5.2 BF XTEM images of CdTe/$Mg_xCd_{1-x}Te$ DH grown at 235 °C: (a) lower region; (b) upper region.

Similar highly-defective film morphology was observed for the structure grown at 295 °C, as shown in Figure 5.3. The bottom part of the double heterostructure for this sample had a very complicated network of entangled defects. The defect density decreased from ~ 10^8 cm^{-2} moving away from the CdTe/InSb interface but quite a few stacking fault (SF) defects and dislocations, perhaps ~ 10^7 cm^{-2}, were still visible in the upper region of the structure. The defective nature of the films grown at 235 °C and 295 °C is considered as unlikely to be due to sample preparation artifacts, because the sample grown at 265 °C, which showed very few defects, has been prepared for TEM observation using the same procedure.

The sample showing the best structural quality of this series was obtained from the growth at 265 °C, and a representative BF XTEM image of the CdTe/$Mg_xCd_{1-x}Te$ double heterostructure grown at this temperature is shown in Figure 5.4 (a). Very few extended defects were visible, although SF defects were very occasionally seen, as shown by the example in Figure 5.4 (b). The lateral extent of this SF was not clear because only part of

the fault structure was captured in this cross-sectional micrograph. The bottom $Mg_xCd_{1-x}Te$ barrier layer is clearly visible and free of defects, while the CdTe/InSb interface can also be identified due to slight differences in diffraction conditions. No extended defects were visible at this interface across several tens of microns of viewing area.

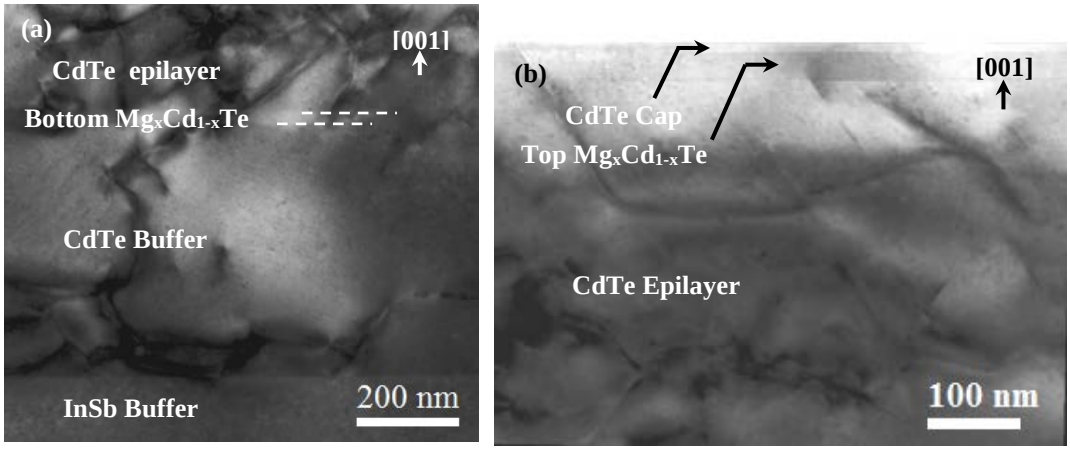

Figure 5.3 BF XTEM images of the $CdTe/Mg_xCd_{1-x}Te$ double heterostructure grown at 295 °C: (a) lower region (close to the substrate); (b) upper region.

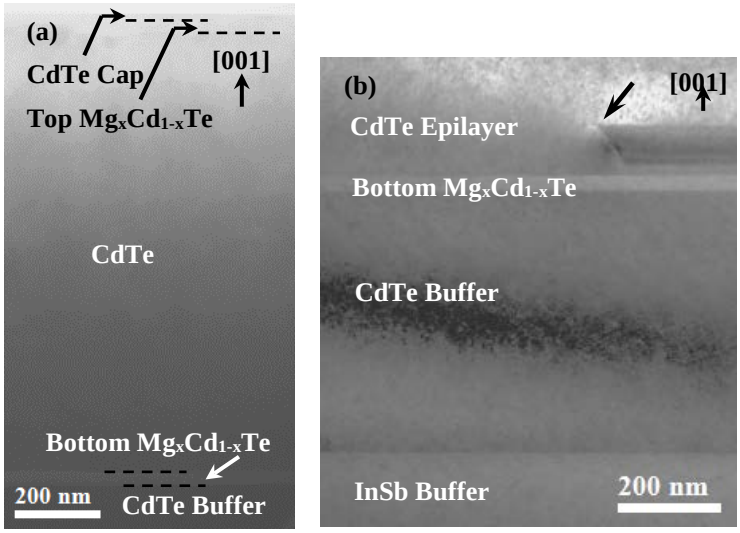

Figure 5.4 (a) BF XTEM image showing the entire $CdTe/Mg_xCd_{1-x}Te$ double heterostructure grown at 265 °C, (b) bottom region, showing an isolated stacking fault defect (arrowed) in the lower part of the CdTe film.

Aberration-corrected HAADF and BF STEM images (Figure 5.5) taken from this sample showed coherent defect-free interfaces between the CdTe and $Mg_xCd_{1-x}Te$ layer, and the top surface had excellent crystallinity. The minority carrier lifetime of this sample was measured using time-resolved photoluminescence (TRPL) to be 86 ns, which was the longest lifetime measured of this series of samples [15]. For comparison, the minority carrier lifetimes of the samples grown at 235 °C and 295 °C were 35 ns and 73 ns, respectively [16, 17].

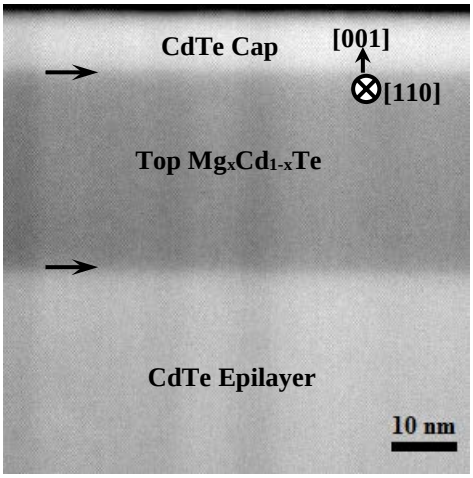

Figure 5.5 Aberration-corrected HAADF STEM image showing the upper region of the double heterostructure grown at 265 °C, with coherent, defect-free CdTe/$Mg_xCd_{1-x}Te$ interfaces (arrowed).

The non-monotonic dependence of defect density and carrier lifetime on growth temperature can be reasonably understood. There are many examples of epitaxial heterostructures reported in the literature where there is a well-defined temperature range for optimal growth, with low temperatures being limited mostly by surface mobility, and higher temperatures being constrained by inter-diffusion. In our experiments, the Cd/Te flux ratio of 1.5 : 1 (3.5 : 1 for the initial 2 minutes) was maintained continuously to ensure a Cd-rich surface, and this condition was confirmed by the 2×1 and c(2×2) RHEED patterns

observed at all growth temperatures. At the lower growth temperature, the mobility of atoms on the surface may well be low, and this effect is apparently manifested by the defective epilayer observed. Chew et al. have [5] reported the formation of polycrystalline CdTe and Te precipitates at very low growth temperature, < 150 °C, which is considerably lower than the temperature used here. We observed networks of extended defects, but no evidence for Te precipitates in the sample grown at 235 °C. At the higher growth temperature, inter-diffusion across the interface is likely to be enhanced, and could easily deteriorate the coherence of the CdTe epilayer in the vicinity of the interface. For regions away from the interface, the influence of such diffusion is reduced. This could help explain why the minority carrier lifetime measured in this sample was higher than measured in the sample grown at the lowest temperature: the upper region of this epilayer, which is effectively where PL is probing, is relatively less defective for the highest temperature sample.

5.4. CdTe/InSb Interface

The CdTe/InSb interface (also the InSb/CdTe interface) has been a subject of considerable interest for microscopists ever since the early trials of CdTe growth on InSb [18]. X-ray photoemission spectroscopy and Raman spectroscopy were used previously to extract information about the interface, and the possible formation of an interfacial compound with much smaller lattice constant (III-VI compound) was suggested [8, 9]. High structural quality interface can nowadays be routinely achieved, removing historical challenges of extensive faulted interfacial structures such as precipitates and In_2Te_3 compounds. However, the atomistic nature of the interface remains a mystery, and the possibility of inter-diffusion still remains. These would alter the compositional profile of

the structures, and directly influence the electronic and optoelectronic properties. The quest of understanding the atomistic nature of the CdTe/InSb interface is non-trivial since the four elements are closely positioned in the Periodic Table, which results in close similarity of the four in all aspects that can be utilized to generate signals collected via different microscopy techniques. Here geometric phase misfit strain analysis was applied to study this heterovalent interface indirectly.

HAADF STEM imaging was followed by GPA study, to reveal the misfit strain between CdTe and InSb. This serves as an ideal survey step, because HAADF STEM image contrast remains true to slight variation in thickness or value of defocus, and GPA is straightforward to implement to extract misfit strain information that is hidden within high-resolution images.

Aberration-corrected HAADF STEM images of the CdTe/InSb interface were taken for the sample grown at 265 °C, to explore the misfit strain distribution, i.e. in-plane, out-of-plane misfit strain, rotation and shear, across the interfacial layers. The out-of-plane misfit strain in the [001] growth direction is defined by the Eq. (5.1):

$$\xi_{zz} = \frac{c_{\text{alloy}} - c_{\text{reference}}}{c_{\text{reference}}} \tag{5.1}$$

where c is the lattice constant along the growth direction, and the InSb buffer region can be used as the zero-strain reference for all analysis. Images with the interface oriented vertically and horizontally were recorded for analysis of the out-of-plane and in-plane misfit strain, respectively, to eliminate the possible influence of scan distortion.

The in-plane misfit strain, i.e., misfit strain within the (001) growth plane, and the rotation and shear, were negligible (below the detectability of GPA analysis here) across

the interface, and over the field of view (not shown here). Figure 5.6 (a) is a representative HAADF STEM image of the CdTe/InSb buffer interface recorded with the interface vertically oriented (rotated post-recording to have growth direction pointing upwards), and is used to extract the out-of-plane misfit strain map and line profile, as shown in Figure 5.6 (b) and (c), respectively.

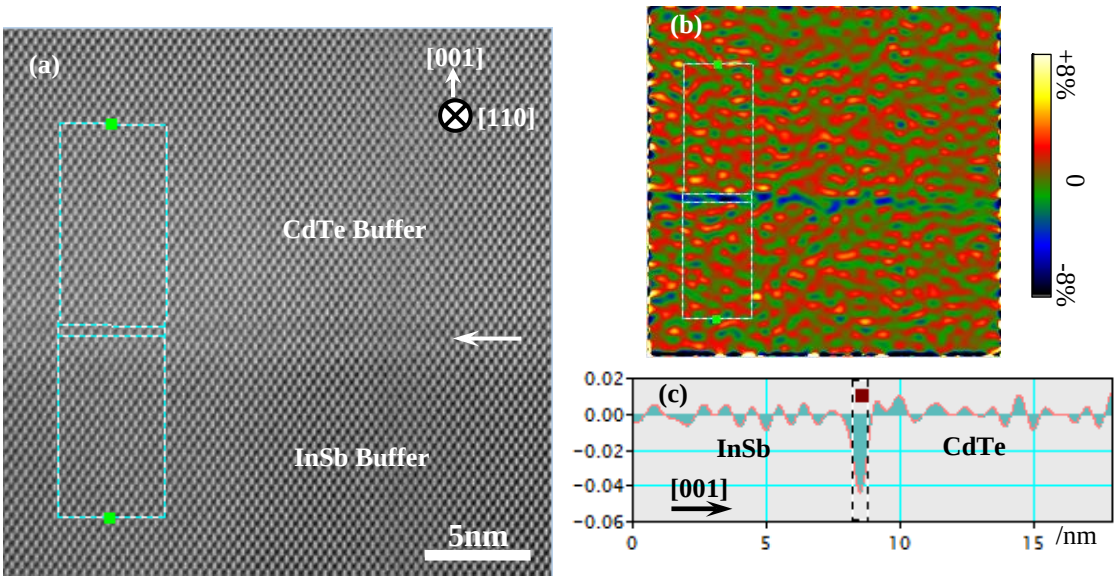

Figure 5.6 (a) Aberration-corrected HAADF STEM image of sample grown at 265 °C showing the CdTe/InSb interface; (b) out-of-plane misfit strain map obtained from GPA analysis; (c) line profile of out-of-plane misfit strain extracted from the misfit strain map averaged perpendicular to the growth direction (diffraction spots from two {111} planes were selected for GPA calculation).

The CdTe epi-layer is on-average under slight compressive misfit strain, which is attributed to its slightly larger lattice parameter compared to the InSb buffer. A sharp tensile spike is observed right at the CdTe/InSb interface (arrowed), while the misfit strain in the adjacent InSb and CdTe regions is relatively uniform. The width of the spike is ~ 0.7 nm, while the GPA spatial resolution defined by this analysis is 0.7 nm. Such a sharp spike is an indication of a rigid-body displacement across a few monolayers at the interface (rather than elastic strain), but the analysis shows no evidence for the formation of any interfacial

defects, although the possibility of an atomically thin layer of a II-V compound cannot be excluded. The slightly different thermal expansion/contraction behavior of CdTe and InSb did not cause noticeable lattice disruption.

5.5. Future Work: CdTe/InSb Interface

5.5.1. Analysis of Dumbbell Spacing and Intensity

Theoretically, with HAADF STEM images with good signal-to-noise ratio, it should be possible to resolve individual atomic columns with local maximum intensity that is related to atomic number (approaching Rutherford scattering approximation with a $\boldsymbol{Z}$-dependence of $\boldsymbol{Z}^2$ [19]), and the dumbbell spacings should reflect the atomic-column separation, at least in projection. An example of such study for a similar but simpler system, the interface of ZnTe/CdSe has been reported [20]. In practice, however, the slight difference in atomic numbers of the elements involved here: Cd-48, In-49, Sb-51 and Te-52, diminishes the possibility of detecting the interfacial elements through analysis of atomic-column intensity. Thus, measurement of dumbbell spacing is carried out to elucidate the nature of interfacial bonding because different III-VI and II-V compounds have different lattice constants.

The lattice constant for CdTe is of 0.649 nm [21]. The {110} dumbbell spacing can be calculated as a quarter of the lattice parameter along [001] direction (Figure 5.7). With the consideration of tetragonal distortion as a result of coherent constraint of the film with the substrate, the dumbbell spacing along [001] direction is approximately the same with the case without: $a_{001}/4 = 0.648 \text{ nm}/4 = 0.162 \text{ nm}$. Thus, through analysis of dumbbell spacing along the growth direction, information about the interfacial bonding might be obtained.

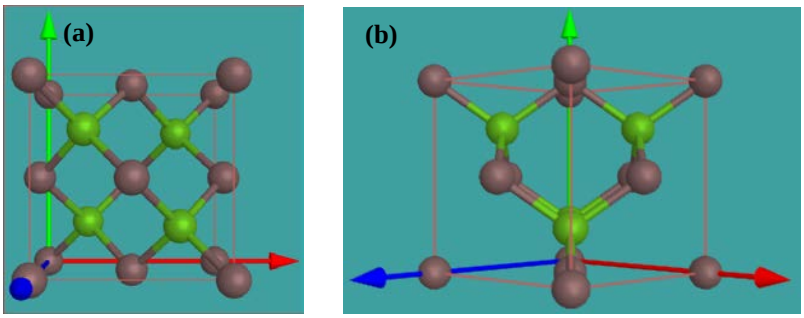

Figure 5.7 CdTe unit cell viewed along (a) [001], and (b) [110] projections.

HAADF STEM images will be recorded with the growth direction parallel to the scanning direction, and intensity line profiles will be extracted for measurements of the dumbbell spacings from the positions of intensity maxima.

5.5.2. Spectroscopy Analysis

Spectrum imaging techniques can provide compositional information with high spatial resolution, even atomic resolution in favorable cases. The aberration-corrected JEOL ARM 200F is equipped with both Dual-EELS collection system and EDX detector, and allow simultaneous acquisition of both EELS and EDX spectrum images at high spatial resolution. Thus, the possibility of identifying the extent of inter-diffusion, if any, and the atomistic structure of the CdTe/InSb interface has been pursued using such techniques.

The major challenge for analysis lies in the fact that the two closely lattice-matched compounds consist of elements with very close atomic numbers. Thus, the characteristic inelastic scattering events significantly overlap in the energy spectrum: X-ray peaks of the same/similar group overlap, and energy-loss edges of interest are all delayed and significantly overlap (see Table 5.1).

To reliably separate and afterward quantify the delayed energy-loss edges, individual reference spectrum for each element with similar valence state with CdTe and

InSb are required to perform a multiple linear least-square fitting procedure, e.g. Cd reference spectrum from CdX with X being similar with but other than Te, In reference spectrum from InAs, Sb reference spectrum from GaSb and Te reference spectrum from ZnTe. To ensure goodness of MLLS fitting, the relative thickness of the specimen needs to be controlled to be well below one mean free path for inelastic scattering. This stringent thickness requirement proves difficult to realize considering the brittle and prone-to-beam-damage nature of CdTe and InSb.

Table 5.1 Summary of EDX peaks and EELS edges of interest for the four elements.

	EDX/keV				**EELS**/eV
	$\mathbf{L}_{\alpha}$	$\mathbf{L}_{\beta 1}$	$\mathbf{L}_{\beta 2}$	**K**	$\mathbf{M}_{4,5}$(delayed)
Cd	3.13	3.32	3.53	23.17	404
In	3.29	3.49	3.71	24.21	443
Sb	3.60	3.84	4.10	26.36	528
Te	3.77	4.03	4.30	27.47	572

In comparison, EDX analysis may be implemented with similar capability of providing compositional information, with the possible drawback of relatively lower spatial resolution due to the less-well-defined nature of X-ray fluorescence. However, as shown in Table 5.1, EDX peaks of interest, $\mathbf{L}_{\alpha}$, $\mathbf{L}_{\beta 1}$ and $\mathbf{L}_{\beta 2}$ peaks, significantly overlap, and the difference between peaks of interest are less than the energy resolution available with the current equipment. This means that peak deconvolution is needed assuming that the peaks are Gaussian in shape. This issue can be better visualized in Figure 5.8, where X-ray spectra were acquired from InSb region and CdTe region, and prominent X-ray

peaks for Cd, In, Sb and Te are labelled in red vertical lines using Gatan DigitalMicrograph plug-in for EDX analysis.

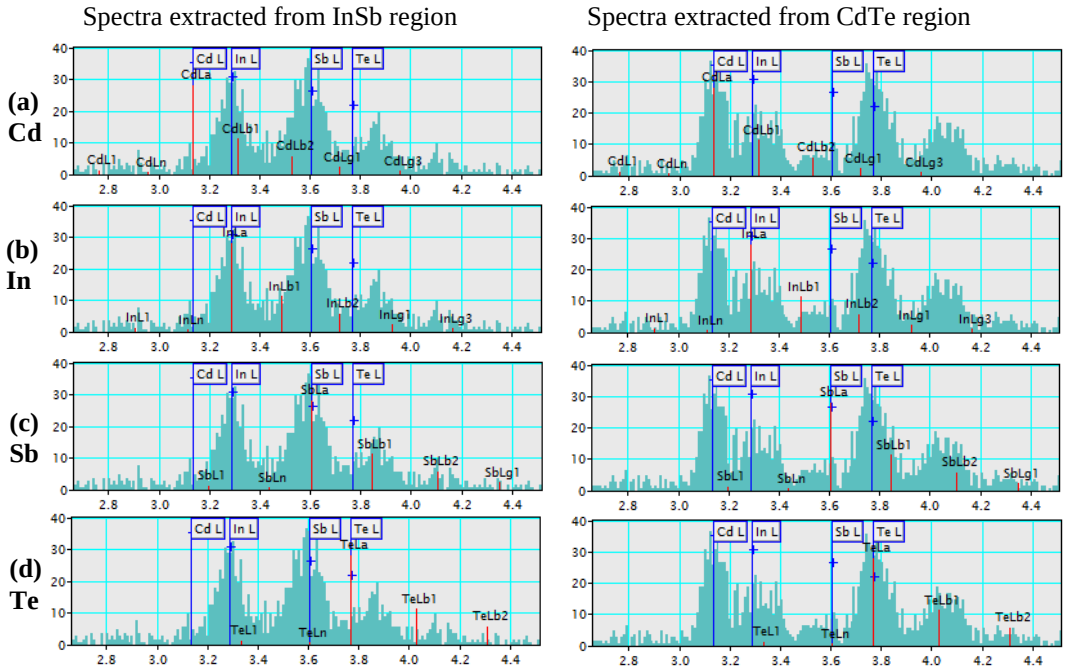

Figure 5.8 EDX spectra acquired in InSb region (left column) and CdTe region (right column). Prominent X-ray peaks are labelled in red vertical lines for Cd at row (a), In at row (b), Sb at row (c) and Te at row (d).

This issue of signal overlapping emphasizes that deconvolution of the EELS and EDX spectra to assess the composition profile across the CdTe/InSb interface will be a challenging task.

References

[1] J. Lu, M. J. DiNezza, X.-H. Zhao, S. Liu, Y.-H. Zhang, A. Kovacs, R. E. Dunin-Borkowski and D. J. Smith, J. Cryst. Growth **439**, 99 (2016).

[2] R. F. C. Farrow, G. R. Jones, G. M. Williams and I. M. Young, Appl. Phys. Lett. **39**, 954 (1981).

[3] R. F. C. Farrow, J. Vac. Sci. Technol. A **3**, 60 (1985).

[4] G. M. Williams, C. R. Whitehouse, A. G. Cullis, N. G. Chew and G. W. Blackmore, Appl. Phys. Lett. **53**, 1847 (1988).

[5] N. G. Chew, G. M. Williams and A. G. Cullis, Inst. Phys. Conf. **68**, 437 (1983).

[6] R. F. C. Farrow, A. J. Noreika, F. A. Shirland, W. J. Takei, S. Wood, J. Greggi Jr. and M. H. Francombe, J. Vac. Sci. Technol. A **2**, 527 (1984).

[7] M. J. DiNezza, X.-H. Zhao, S. Liu, A. P. Kirk and Y.-H. Zhang, Appl. Phys. Lett. **103**, 193901 (2013).

[8] K. J. Mackey, P. M. G. Allen, W. G. Herrenden-Harker and R. H. Williams, Appl. Phys. Lett. **49**, 354 (1986).

[9] D. R. T. Zahn, K. J. Mackey and R. H. Williams, Appl. Phys. Lett. **50**, 742 (1987).

[10] Z. C. Feng, A. Mascarenhas, W. J. Choyke, R. F. C. Farrow, F. A. Shirland and W. J. Takei, Appl. Phys. Lett. **47**, 24 (1985).

[11] M. J. Hÿtch, E. Snoeck and R. Kilaas, Ultramicroscopy **74**, 131 (1998).

[12] A. G. Cullis, N. G. Chew and J. L. Hutchison, Ultramicroscopy **17**, 203 (1985).

[13] T. Aoki, Y. Chang, G. Badano, J. Zhao, C. Grein, S. Sivananthan and D. J. Smith, J. Cryst. Growth **265**, 224 (2004).

[14] C. Wang, S. Tobin, T. Parodos, J. Zhao, Y. Chang, S. Sivananthan and D. J. Smith, J. Vac. Sci. Technol. A **24**, 995 (2006).

[15] S. Wood, J. Greggi Jr., R. F. C. Farrow, W. J. Takei, F. A. Shirland and A. J. Noreika, J. Appl. Phys. **55**, 4225 (1984).

[16] X.-H. Zhao, M. J. DiNezza, S. Liu, S. Lin, Y. Zhao and Y.-H. Zhang, J. Vac. Sci. Tech. B **32**, 040601-1 (2014).

[17] X.-H. Zhao, M. J. DeNezza, S. Liu, Y. Zhao and Y.-H. Zhang, unpublished results.

[18] J. L. Hutchison, W. G. Waddington, A. G. Cullis and N. G. Chew, J. Microsc. **142**, 153 (1986).

[19] S. J. Pennycook and P. D. Nellist, Scanning transmission Electron Microscopy: Imaging and Analysis (Springer Science + Business Media, LLC, New York, 2011) Chapt. 8, p. 370.

[20] B. Bonef, L. Gerard, J.-L. Rouviere, A. Grenier, P.-H. Jouneau, E. Bellet-Amalric, H. Mariette, R. Andre and C. Bougerol, Appl. Phys. Lett. **106**, 051904 (2015).

[21] S. Adachi, Handbook on Physical Properties of Semiconductors, Vol. 3: II–VI Compound Semiconductors, Chap. 14, p. 359, Springer, US (2004).

REFERENCES

A. Barna, B. Pecz and M. Menyhard, Ultramicroscopy **70**, 161 (1998).

A. G. Cullis, N. G. Chew and J. L. Hutchison, Ultramicroscopy **17,** 203 (1985).

A. G. Norman, R. France, and A. J. Ptak, J. Vac. Sci. Technol. B **29**, 03C121 (2011).

A. Hoffman, Introduction to Infrared Detection, 39th Annual Modern infrared Detectors and System Applications, UCSB Extension, June 19-23, 2006.

A. Janotti, S.-H. Wei and S.B. Zhang, Phys. Rev. B **65**, 115203 (2002).

A. Rogalski, Infrared Detectors (Overseas Publishers Association, Amsterdam, The Netherlands, 2000) p. 402.

A. Rogalski, Opto-Electron. Rev. **20**, 279 (2012).

A. Rogalski, Rep. Prog. Phys. **68**, 2267 (2005).

A. Semenov, O. G. Lyublinskaya, V. A. Solovev, B. Y. Meltser and S. V. Ivanov, J. Cryst. Growth **301**, 58 (2007).

A. Y. Cho, J. Appl. Phys. **41**, 2780 (1970).

A. Y. Lew, E. T. Yu and Y.-H. Zhang, J. Vac. Sci. Technol. B **14**, 2940 (1996).

B. B. V. Olson, Appl. Phys. Lett. **101**, 092109 (2012).

B. Bonef, L. Gerard, J.-L. Rouviere, A. Grenier, P.-H. Jouneau, E. Bellet-Amalric, H. Mariette, R. Andre and C. Bougerol, Appl. Phys. Lett. **106**, 051904 (2015).

B. F. Levine, J. Appl. Phys. **74**, R1 (1993).

B. F. Levine, K. K. Choi, C. G. Bethea, J. Walker and R. J. Malik, Appl. Phys. Lett. **50**, 1092 (1987).

B. Fultz and J. Howe, Transmission Electron Microscopy and Diffractometry of Materials, 3rd edition (Springer-Verlag Berlin Heidelberg, 2008) p. 122.

B. Fultz and J. Howe, ibid., p. 224.

B. Fultz and J. Howe, ibid., p. 583.

C. Kittel, Introduction to Solid State Physics, 8th edition (John Wiley & Sons, Inc. New York, USA, 2005) p. 188.

C. Kittel, ibid., p. 209.

C. Kittle, Thermal Physics (John Wiley & Sons, Inc. New York, 1969) p. 253.

C. Mailhiot, D. L. Smith, J. Vac. Sci. Technol. B **5**, 1268 (1987).

C. Wang, S. Tobin, T. Parodos, J. Zhao, Y. Chang, S. Sivananthan and D. J. Smith, J. Vac. Sci. Technol. A **24**, 995 (2006).

D. A. Cullen and D. J. Smith, J. Appl. Phys. **104**, 094304 (2008).

D. B. Holt and B. G. Yacobi, Extended Defects in Semiconductors (Cambridge University Press, Cambridge, UK, 2007) p. 24.

D. B. Williams and C. B. Carter, Transmission Electron Microscoy: A Textbook for Materials Science, 2nd edition (Springer Science + Business Media, LLC, New York, 2009) p. 261.

D. B. Williams and C. B. Carter, ibid., p. 263.

D. B. Williams and C. B. Carter, ibid., p. 295.

D. B. Williams and C. B. Carter, ibid., p. 371.

D. C. Joy, A. D. Romig, Jr. and J. I. Goldstein, Principles of Analytical Electron Microscopy (Plenum Press, New York, 1986) p. 12.

D. C. Joy, A. D. Romig, Jr. and J. I. Goldstein, ibid, p. 254.

D. J. Barber, Ultramicroscopy **52**, 101 (1993).

D. J. Lovell, Amer. J. Phys. **37**, 467 (1969).

D. J. Smith, Instrumentation and Operation and High Resolution Electron Microscopy, Vol. 11 of Advances in Optical and Electron Microscopy (Academic Press, London, New York, 1989) p. 12.

D. O. Klenov, S. D. Findlay, L. J. Allen and S. Stemmer, Phys. Rev. B **76**, 014111 (2007).

D. R. Rhiger, J. Electron. Mater. **40**, 1815 (2011).

D. R. T. Zahn, K. J. Mackey and R. H. Williams, Appl. Phys. Lett. **50**, 742 (1987).

D. Schroder, Semiconductor Material and Device Characterization, 3rd edition (John Wiley & Sons, Inc. New Jersey, USA, 2006) p. 389.

E. G. Bithell and W. M. Stobbs, Philos. Mag. A **60**, 39 (1989).

E. H. Steenbergen, B. C. Connelly, G. D. Metcalfe, H. Shen, M. Wraback, D. Lubyshev, Y. Qiu, J. M. Fastenau, A. W. K. Liu, S. Elhamri, O. O. Cellek and Y. -H. Zhang, Appl. Phys. Lett. **99**, 251110 (2011).

E. H. Steenbergen, Y. –H. Zhang, unpublished result.

E. Luna, A. Guzman, A. Trampert and G. Alvarez, Phys. Rev. Lett. **109**, 126101 (2012).

E. Luna, A. M. Beltran, A. M. Sanchez, and S. I. Molina, Appl. Phys. Lett. **101**, 011601 (2012).

E. Luna, B. Satpati, J. B. Rodriguez, A. N. Baranov, E. Tournié, and A. Trampert, Appl. Phys. Lett. **96**, 021904 (2010).

E. P. O'Reilly, Semicond. Sci. Technol. **4**, 121 (1989).

F. Capasso, Science **235**, 172 (1987).

F. D. Morten, R. E. King, Appl. Optics **4**, 659 (1965).

F. G. Smith, Atmospheric Propagation of Radiation (Infrared Information Analysis Center, Ann Arbor, Michigan and SPIE Optical Engineering Press, Bellingham, Washington, 1993) p. 46.

G. C. Osbourn, J. Vac. Sci. Technol. B **2**, 176 (1984).

G. J. Zissis, Sources of Radiation (Infrared Information Analysis Center, Ann Arbor, Michigan and SPIE Optical Engineering Press, Bellingham, Washington, 1993) p. 14.

G. M. Williams, C. R. Whitehouse, A. G. Cullis, N. G. Chew and G. W. Blackmore, Appl. Phys. Lett. **53**, 1847 (1988).

G. Patriarche, L. Largeau, J. C. Harmand and D. Gollub, Appl. Phys. Lett. **84**, 203 (2004).

G. Vardar, S. W. Paleg, M. V. Warren, M. Kang and R. S. Goldman, Appl. Phys. Lett. **102**, 042106 (2013).

H. Li and Z. M. Wang, Bismuth-containing compound (Springer Science + Business Media, New York, USA, 2013) p. 2.

H. Li and Z. M. Wang, ibid., p. 5.

H. Okamoto and K. Oe, Jpn. J. Appl. Phys. **37**, 1608 (1998).

I. Simon, Infrared Physics (D. Van Nostrand Company, Inc. Princeton, New Jersey, 1966) p. 10.

J. Ayache, L. Beaunier, J. Boumendil, G. Ehret and E. Laub, Sample Preparation Handbook for Transmission Electron Microscopy Methodology (Springer Science + Business Media, LLC, New York, 2010) p. 83.

J. C. H. Spence and J. M. Zuo, Electron Microdiffraction (Springer Science + Business Media, New York, 1992) p. 20.

J. C. H. Spence and J. M. Zuo, ibid., p. 146.

J. Chu and A. Sher, Physics and Properties of Narrow Gap Semiconductors (Springer Science + Business Media, LLC, New York, 2007) p. 5.

J. J. Lee, M. Razeghi, Investigation of novel InTlSb and InSbBi alloys for uncooled photodetector applications (SPIE-INT Soc. Optical Engineering, Bellinghan, USA, 1998) p. 256.

J. J. P. Peters, R. Beanland, M. Alexe, J. W. Cockburn, D. G. Revin, S. Y. Zhang and A. M. Sanchez, Ultramicroscopy **157**, 91 (2015).

J. L. Hutchison, W. G. Waddington, A. G. Cullis and N. G. Chew, J. Microsc. **142**, 153 (1986).

J. L. Miller, Principles of Infrared Technology (Van Nostrand Reinhold, New York, 1994) p. 6.

J. Lu, E. Luna, T. Aoki, E. H. Steenbergen, Y.-H. Zhang, and D. J. Smith, J. Appl. Phys. **119**, 095702 (2016).

J. Lu, M. J. DiNezza, X.-H. Zhao, S. Liu, Y.-H. Zhang, A. Kovacs, R. E. Dunin-Borkowski and D. J. Smith, J. Cryst. Growth **439**, 99 (2016).

J. Lu, P. T. Webster, S. Liu, Y.-H. Zhang, S. R. Johnson and D. J. Smith, J. Cryst. Growth **425**, 250 (2015).

J. M. Cowley, Appl. Phys. Lett. **15**, 58 (1969).

J. M. Zuo, Ultramicroscopy **41**, 211 (1992).

J. N. Stirman, M. Takeguchi, M. R. McCartney and D. J. Smith, Appl. Phys. Lett. **84**, 490 (2004).

J. R. Arthur, J. Appl. Phys. **39**, 4032 (1968).

J. Steinshnider, J. Harper, M. Weimer, C.-H. Lin, S.-S. Pei and D. H. Chow, Phys. Rev. Lett. **85**, 4562 (2000).

J. W. Matthews and A. E. Blakeslee, J. Cryst. Growth **27**, 118 (1974).

K. Alberi, J. Wu, W. Walukiewicz, K. Yu, O. Dubon, S. Watkins, C. Wang, X. Liu, Y.-J. Cho and J. Furdyna, Phys. Rev. B **75**, 045203 (2007).

K. J. Mackey, P. M. G. Allen, W. G. Herrenden-Harker and R. H. Williams, Appl. Phys. Lett. **49**, 354 (1986).

K. K. Ng, Complete Guide to Semiconductor Devices, 2nd edition (John Wiley & Sons, Inc. New York, USA, 2002) p. 1.

K. Mahalingam, E. H. Steenbergen, G. J. Brown and Y.-H. Zhang, Appl. Phys. Lett. **103**, 061908 (2013).

K. Muraki, S. Fukatsu, Y. Shiraki and R. Ito, Appl. Phys. Lett. **61**, 557 (1992).

K. Oe and H. Asai, IEICE Trans. Electron **E79C**, 1751 (1996).

K. Y. Ma, Z. M. Fang, R. M. Cohen and G. B. Stringfellow, J. Cryst. Growth **107**, 416 (1991).

K. Y. Ma, Z. M. Fang, R. M. Cohen and G. B. Stringfellow, J. Electron. Mater. **21**, 143 (1992).

L. A. Giannuzzi and F. A. Stevie, Introduction to Focused Ion Beams (Springer Science + Business Media, Inc., Boston, 2005) p. 3.

L. Dominguez, D. F. Reyes, F. Bastiman, D. L. Sales, R. D. Richards, D. Mendes, J. P. R. David and D. Gonzalez, Appl. Phys. Express **6**, 112601 (2013).

L. Esaki and R. Tsu, IBM J. Res. Dev. **14**, 61 (1970).

L. Ouyang, E. H. Steenbergen, Y.-H. Zhang, K. Nunna, D. L. Huffaker and D. J. Smith, J. Vac. Sci. Technol. B **30**, 02B106 (2012).

L. Reimer and H. Kohl, Transmission Electron Microscopy: Physics of Image Formation, 5th edition (Springer Science + Business Media, LLC, New York, 2008) p. 329.

L. Reimer and H. Kohl, ibid., p. 369.

M. A. Kinch, Fundamentals of Infrared Detector Materials (SPIE, Bellingham, Washington, 2007) p. 2.

M. A. Kinch, ibid., p. 5.

M. J. DiNezza, X.-H. Zhao, S. Liu, A. P. Kirk and Y.-H. Zhang, Appl. Phys. Lett. **103**, 193901 (2013).

M. J. Hÿtch, E. Snoeck and R. Kilaas, Ultramicroscopy **74**, 131 (1998).

M. N. Kutty, E. Plis, A. Khoshakhlagh, S. Myers, N. Gautam, S. Smolev, Y. D. Sharma, R. Dawson, S. Krishna, S. J. Lee and S. K. Noh, Journal of Electronic Materials **39**, 2203 (2010).

M. R. Wood, K. Kanedy, F. Lopez, M. Weimer, J. F. Klem, S. D. Hawkins, E. A. Shaner and J. K. Kim, J. Cryst. Growth **425**, 110 (2015).

M. Wu, E. Luna, J. Puustinen, M. Guina and A. Trampert, Nanotechnology **25**, 205605 (2014).

M. Wu, E. Luna, J. Puustinen, M. Guina and A. Trampert, Appl. Phys. Lett. **105**, 041602 (2014).

M. Wu, M. Hanke, E. Luna, J. Puustinen, M. Guina and A. Trampert, Nanotechnology **26**, 425701 (2015).

N. G. Chew, G. M. Williams and A. G. Cullis, Inst. Phys. Conf. **68**, 437 (1983).

N. J. Ekins-Daukes, K. Kawaguchi, and J. Zhang, Cryst. Growth Des. **2**, 287 (2002).

O. Dier, C. Lin, M. Grau and M.-C. Amann, Semicond. Sci. Tehcnol. **19**, 1250 (2004).

P. A. Doyle and P. S. Turner, Acta Cryst. A **24**, 390 (1968).

P. Martyniuk, J. Antoszewski, M. Martyniuk, L. Faraone and A. Rogalski, Appl. Phys. Rev. **1**, 041102 (2014).

P. Stadelmann, Ultramicroscopy **21**, 131 (1987).

P. T. Webster, N. A. Riordan, C. Gogineni, S. Liu, J. Lu, X.-H. Zhao, D. J. Smith, Y.-H. Zhang and S. R. Johnson, J. Vac. Sci. Technol. B **32**, 02C120-1 (2014).

P. W. Kruse, L. D. McGlauchlin and R. B. McQuistan, Elements of Infrared Technology (Wiley, New York, 1962) p. 399.

R. A. Soref, J. Appl. Phys. **38**, 5201 (1967).

R. Brydson, Aberration-Corrected Analytical Transmission Electron Microscopy (John Wiley & Sons, Ltd. West Sussex, UK, 2011) p. 189.

R. Dingle, W. Wiemann and C. H. Henry, Phys. Rev. Lett. **33**, 827 (1974).

R. F. C. Farrow, A. J. Noreika, F. A. Shirland, W. J. Takei, S. Wood, J. Jr. Greggi and M. H. Francombe, J. Vac. Sci. Technol. A **2**, 527 (1984).

R. F. C. Farrow, G. R. Jones, G. M. Williams and I. M. Young, Appl. Phys. Lett. **39**, 954 (1981).

R. F. C. Farrow, J. Vac. Sci. Technol. A **3**, 60 (1985).

R. F. C. Farrow, Molecular Beam Epitaxy, Applications to Key Materials (Noyes Publications, New Jersey, USA, 1995) p. 2.

R. F. C. Farrow, ibid., p. 9.

R. F. Egerton, Electron Energy-Loss Spectroscopy in the Electron Microscope, 3rd edition (Springer Science + Business Media, LLC, New York, 2011) p. 142.

R.F. Egerton, ibid., p. 249.

R. F. Egerton, ibid., p. 287.

R. F. Egerton, ibid., p. 302.

R. F. Pierret, Advanced Semiconductor Fundamentals (Addison-Wesley Publishing Company, Inc., Massachusetts, USA, 1987) p. 10.

R. F. Pierret, ibid., p. 53.

R. F. Pierret, Semiconductor Fundamentals (Addison-Wesley Publishing Company, Inc. Massachusetts, USA, 1988) p. 27.

R. G. Driggers, M. H. Friedman and J. Nichols, Introduction to Infrared and Electro-optical Systems, 2nd edition (Artech House, Norwood, MA, 2012) p. 127.

R. Kilaas, J. Microscopy **190**, 45 (1998).

R. N. Jacobs, C. Nozaki, L. A. Almeida, M. Jaime-Vasquez, C. Lennon, J. K. Markunas, D. Benson, P. Smith, W. F. Zhao, D. J. Smith, C. Billman, J. Arias and J. Pellegrino, J. Electron. Mater., **41**, 2707 (2012).

R. Triboulet, A. Tromson-Carli, D. Lorans and T. N. Duy, J. Electron. Mater. **22**, 827 (1993).

R. Vincent and P, Midgley, Ultramicroscopy **53**, 271 (1994).

S. A. Barnett, J. Vac. Sci. Technol. A **5**, 2845 (1987).

S. Adachi, Handbook on Physical Properties of Semiconductors (Springer Science + Business Media, New York, USA, 2004) vol. 2 & vol. 3.

S. Adachi, ibid., Chap. 14, p. 359.

S. Adachi, ibid., Vol. 2, p. 453.

S. Borrello and H. Levinstein, J. Appl. Phys. **33**, 2947 (1962).

S. Francoeur, M.-J. Seong, A. Mascarenhas, S. Tixier, M. Adamcyk and T. Tiedje, Appl. Phys. Lett. **82**, 3874 (2003).

S. J. Pennycook and P. D. Nellist, Scanning Transmission Electron Microscopy: Imaging and Analysis (Springer Science + Business Media, LLC, New York, 2011) p. 163.

S. J. Pennycook and P. D. Nellist, ibid., p. 307.

S. J. Pennycook and P.D. Nellist, ibid., Chapt. 8, p. 370.

S. Kasap and P. Capper, Handbook of Electronic and Photonic Materials (Springer Science + Business Media, Inc. New York, USA, 2006) p. 855.

S. P. Svensson, D. Donetsky, D. Wang, H. Hier, F. J. Crowne and G. Belenky, J. Cryst. Growth **334**, 103 (2011).

S. P. Svensson, H. Hier, W. L. Sarney, D. Donetsky, D. Wang and G. Belenky, J. Vac. Sci. Technol. A **30**, 02B109 (2012).

S. R. Johnson, Yu.G. Sadofyev, D. Ding, Y. Cao, S. A. Chaparro, K. Franzreb, Y.-H. Zhang, J. Vac. Sci. Technol. B **22**, 1436 (2004).

S. Tixier, M. Adamcyk and T. Tiedje, Appl. Phys. Lett. **82**, 2245 (2003).

S. Wang, Y. Song and I.S. Roy, 13th International Conference on Transparent Optical Networks (ICTON), IEEE, New York, USA (2011).

S. Wang, Y. Song and I.S. Roy, 13th International Conference on Transparent Optical Networks (ICTON), Stockholm, Sweden, June 23-30, 2011, edited by M. Jaworski and M. Marciniak (IEEE, Inc. New York, USA, 2011) p. 1.

S. Wood, J. Greggi Jr., R. F. C. Farrow, W. J. Takei, F. A. Shirland and A. J. Noreika, J. Appl. Phys. **55**, 4225 (1984).

T. Aoki, J. Lu, M. R. McCartney and D. J. Smith, Semicond. Sci. Technol. **31**, 094002 (2016).

T. Aoki, Y. Chang, G. Badano, J. Zhao, C. Grein, S. Sivananthan and D. J. Smith, J. Cryst. Growth **265**, 224 (2004).

T. J. DeLyon, J. E. Jensen, M. D. Gorwitz, C. A. Cockrum, S. M. Johnson and G. M. Venzor, J. Electron. Mater. **28**, 705 (1999).

V. Swaminathan and A. T. Macrander, Materials Aspects of GaAs and InP Based Structures (Prentice-Hall, Inc. New Jersey, USA, 1991) p. 138.

V. Swaminathan and A. T. Macrander, ibid., p. 142.

W. D. Lawson, S. Nielson, E. H. Putley and A. S. Young, J. Phys. Chem. Solids **9**, 325 (1959).

www.nanomegas.com

X.-H. Zhao, M. J. DeNezza, S. Liu, Y. Zhao and Y.-H. Zhang, unpublished results.

X.-H. Zhao, M. J. DiNezza, S. Liu, S. Lin, Y. Zhao and Y.-H. Zhang, J. Vac. Sci. Tech. B **32**, 040601-1 (2014).

X.-M. Shen, H. Li, S. Liu, D. J. Smith and Y.-H. Zhang, J. Cryst. Growth **381**, 1 (2013).

Y. Song, S. Wang, I.S. Roy, P. Shi and A. Hallen, J. Vac. Sci. Technol. B **30**, 02B114 (2012).

Y. Takehara, M. Yoshimoto, W. Huang, J. Saraie, K. Oe, A. Chayahara and Y. Horino, Jpn. J. Appl. Phys. **45**, 67 (2006).

Z. C. Feng, A. Mascarenhas, W. J. Choyke, R. F. C. Farrow, F. A. Shirland and W. J. Takei, Appl. Phys. Lett. **47**, 24 (1985).

Z.-H. Yu, D. A. Muller and J. Silcox, J. Appl. Phys. **95**, 3362 (2004).

Z.-Y. Lin, S. Liu, E. H. Steenbergen, Y.-H. Zhang, Appl. Phys. Lett. **107**, 201107 (2015).